EIEлектротехніка і лектромеханіка

Electrical Engineering & Electromechanics

Електротехніка. Визначні події. Славетні імена
Електричні машини та апарати
Техніка сильних електричних та магнітних полів.
 Кабельна техніка
Електричні станції, мережі і системи
Ювілеї

ISSUE 6 / 2019

TABLE OF CONTENTS

M.I. Baranov

AN ANTHOLOGY OF THE DISTINGUISHED ACHIEVEMENTS IN SCIENCE AND TECHNIQUE. PART 52: ROCKET-SPACE TECHNOLOGY DESIGNER MIKHAIL YANGEL AND HIS ACCOMPLISHMENTS IN MISSILE DESIGN

Purpose. Preparation of short scientifically-historical essay about the distinguished designer of domestic space-rocket technique and one of basic creators of missiles for a Soviet rocket-nuclear «shield» Mikhail Kuzmich Yangel. Methodology. Known scientific methods of collection, analysis and analytical treatment of scientific and technical information, regarding becoming and development in the USSR of space-rocket technique of the military and peaceful applications and resulted in scientific monographs, journals and internet-reports. Results. A short scientifically-historical essay is resulted about the distinguished Soviet designer of space-rocket technique of M.K. Yangel, becoming one of creators of domestic strategic rocket-nuclear «shield». Basic scientific and technical achievements of talented and purposeful scientist-mechanic M.K. Yangel are described, becoming in 1954 Head and Chief Designer of the Special Designer Bureau No. 586 (SDB-586, Dnepropetrovsk city), in area of development and creation of powerful battle ballistic rockets of the strategic applications and missiles for the peaceful mastering of space. It is shown that under scientific guidance of the Chief Designer of SDB-586 (in 1966 it began to be named DB «Southern») M.K. Yangel in the USSR were developed and accepted on the armament of rocket strategic armies the Soviet army: battle strategic rockets of the first generation (rockets with military indexes 8K63, 8K65 and 8K64); battle intercontinents ballistic rockets (ICBR) of the second (rockets with military indexes 8K67, 8K69 and 8K67П) and the third (rockets with military indexes 15A14 (on terminology of NATO SS-18 «Satan»), 15A15, 15A16 and 15A18) generations. At creation in the USSR of battle ICBR of the fourth generation (rockets with the military indexes of 15A18M, 15Ж60 and 15Ж61) the ideas of M.K. Yangel were applied. These battle ICBR provided in the period of the «Cold War» for the USSR a party in the world race of strategic rocket-nuclear armaments. Powerful domestic missiles are «Space-1», «Space-2»,»Cyclone-2» and «Cyclone-3», created at SDB-586 (DB «Southern») under the guidance of M.K. Yangel on the base of the indicated battle ICBR, executed the tasks laid on them in area of the peaceful mastering of space. Originality. Certain systematization is executed known from mass of scientific and technical materials media, regarding becoming and development in the USSR of rocket industry, having an important military-strategic and civil value. First for a wide reader the concrete contribution of SDB-586 (DB «Southern»), headed in the period of 1954-1971 by Academician of the Academy of Sciences of the Ukrainian SSR and the Academy of Sciences of the USSR M.K. Yangel is exposed in the concentrated kind, in creation of powerful Soviet battle ICBR, making in the period of 1959-1991 basis of rocket-nuclear «shield» of the USSR. Practical value. Scientific popularization and deepening for the students of higher school, engineering-technical and scientific workers of physical-technical knowledge in area of history of becoming and development in the former USSR of military and peaceful rocket production, extending their scientific and technical range of interests and further development of scientific and technical progress in society. References 24, tables 2, figures 13.
Key words: **space-rocket technology, distinguished Soviet designer of space-rocket technology Mikhail Yangel, achievements in a military and peaceful rocket production, scientifically-historical essay.**

Наведено науково-історичний нарис про видатного радянського конструктора ракетно-космічної техніки Михайла Кузьміча Янгеля, що став одним з творців вітчизняного ракетно-ядерного «щита». Описані основні науково-технічні досягнення М.К. Янгеля в галузі розробки і створення в СРСР бойового стратегічного ракетного озброєння і ракетно-космічної техніки для мирного освоєння космосу. Показано, що Головний конструктор ОКБ-586 (КБ «Південне», м. Дніпропетровськ) М.К. Янгель є «батьком» радянських бойових міжконтинентальних балістичних ракет (МБР) першого (з індексами 8К63, 8К65 і 8К64), другого (з індексами 8К67, 8К69 і 8К67П) та третього (з індексами 15А14, 15А15, 15А16 і 15А18) поколінь. При створенні МБР четвертого покоління (з індексами 15А18М, 15Ж60 і 15Ж61) були застосовані його ідеї. Дані бойові МБР забезпечили в період «холодної війни» для СРСР паритет в світовій гонці стратегічних ракетно-ядерних озброєнь. Бібл. 24, табл. 2, рис. 13.
Ключові слова: **ракетно-космічна техніка, видатний радянський конструктор ракетно-космічної техніки Михайло Янгель, досягнення у військовому і мирному ракетобудуванні, науково-історичний нарис.**

Приведен научно-исторический очерк о выдающемся советском конструкторе ракетно-космической техники Михаиле Кузьмиче Янгеле, ставшем одним из создателей отечественного ракетно-ядерного «щита». Описаны основные научно-технические достижения М.К. Янгеля в области разработки и создания в СССР боевого стратегического ракетного вооружения и ракетно-космической техники для мирного освоения космоса. Показано, что Главный конструктор ОКБ-586 (КБ «Южное», г. Днепропетровск) М.К. Янгель является «отцом» советских боевых межконтинентальных баллистических ракет (МБР) первого (с индексами 8К63, 8К65 и 8К64), второго (с индексами 8К67, 8К69 и 8К67П) и третьего (с индексами 15А14, 15А15, 15А16 и 15А18) поколений. При создании МБР четвертого поколения (с индексами 15А18М, 15Ж60 и 15Ж61) были применены его идеи. Данные боевые МБР обеспечили в период «холодной войны» для СССР паритет в мировой гонке стратегических ракетно-ядерных вооружений. Библ. 24, табл. 2, рис. 13.
Ключевые слова: **ракетно-космическая техника, выдающийся советский конструктор ракетно-космической техники Михаил Янгель, достижения в военном и мирном ракетостроении, научно-исторический очерк.**

Introduction. At present, taking into account the past years and declassifying many previously inaccessible to the general reader materials related to the formation and development of the missile industry in the former USSR, which had important military strategic importance, it is becoming known that the best Soviet intercontinental ballistic missile (ICBMs) were designed and created by

not the notorious designer of rocket and space technology (Chief Designer of SDB-1, Kaliningrad city, Moscow Region), twice Hero of Labor, academician of the Academy of Sciences of the USSR (since 1958) S.P. Korolev [1], but by the Chief Designer of SDB-586 (Design Bureau «Yuzhnoye» («Southern»), Dnipropetrovsk city) M.K. Yangel [2]. It is M.K. Yangel practically «shouldered» the incredible responsibility and the whole burden of the USSR's defense against a potential nuclear missile strike of the enemy's forces of the West. Merits of S.P. Korolev in the creation of the first Soviet ICBMs, set in 1956-1968 into service with the Strategic Missile Forces, no one pleads. In the competition M.K. Yangel actually «untied» the hands of S.P. Korolev for the Soviet breakthrough into peaceful space. It is required to pay tribute to the fully undervalued in the 20th century bright and successful outstanding Soviet designer of rocket and space technology twice Hero of Labor (1959. 1961), Academician of the Academy of Sciences of the Ukrainian SSR (since 1961) and of the Academy of Sciences of the USSR (since 1966) Mikhail Kuzmich Yangel [2] (Fig. 1). To do this, in the form of a scientific and historical essay about him, we make a modest contribution – we as the heirs of the works of M.K. Yangel.

The goal of the paper is preparation of a brief scientific and historical essay on the outstanding designer of domestic rocket and space technology and one of the main creators of launch vehicles for the Soviet nuclear missile «shield» M.K. Yangel.

1. The beginning of life and career of M.K. Yangel. Mikhail was born on November 7, 1911 in the East Siberian village of Zyryanova (Irkutsk province, Russian Empire) in a large peasant family of Kuzma Lavrentievich and Angelina Petrovna Yangel, who had 12 children [2]. As we see, the name and surname of this man glorified in the future by his titanic work is very associated in human consciousness with the divine word «angel», which was, as it were, sent to earthlings from heaven to comprehend the mysteries of our world.

Fig. 1. Outstanding Soviet designer of space and rocket technology, twice Hero of Labor, Lenin Prize Laureate, Doctor of Technical Sciences, Academician of the Academy of Sciences of the Ukrainian SSR and of the Academy of Sciences of the USSR Mikhail Kuzmich Yangel (07.11.1911 – 25.10.1971) [2]

In 1926, after finishing the sixth grade of a village school, he moved to Moscow to his older brother Konstantin [2]. After graduating from a factory school, in the period 1929-1931 Mikhail works as an assistant craftsman at a textile factory (Krasnoarmeysk, Moscow region). In 1931 he entered the Moscow Aviation Institute, which in 1937 he graduated with honors in the specialty «Aircraft Engineering» [2]. In the period 1935-1944 he worked in various positions (starting with the leading engineer and ending with the Director) at the plant-branch at the Design Bureau, led by the famous Soviet aircraft designer N.N. Polikarpov [3]. He participated in the development and refinement of his combat fighter aircrafts I-153, I-180 and I-185 [2]. In 1944 he was Deputy Chief Engineer of the aircraft plant No. 155 at the experimental design bureau (EDB), headed by prominent in the future aircraft designer A.I. Mikoyan, and in 1945 he began to work as a leading engineer at the design bureau of the famous Soviet aircraft designer V.M. Myasishchev [2]. In the period 1946-1948, while working at the special department of the Ministry of Aviation Industry of the USSR, he coordinated work both in the field of domestic aircraft construction and the work of numerous talented Germans-rocket men moved from Germany to the USSR [1]. These two years of communication with German rocket experts and the study of captured documents from Germany in the field of rocketry gave much to M.K. Yangel in understanding the ways of formation of the missile industry in the USSR. In 1950, he graduated with honors from the USSR Academy of Aviation Industry. Since April 12, 1950 (the future Cosmonautics Day of the USSR), its official «entry» into the rocket industry of our country begins [2, 4]: first, he holds the position of Head of Department at SDB-1 (Kaliningrad city, Moscow Region), created at the leading institution of the USSR in the field of rocket science SRI-88 [1] and led by S.P. Korolev, and then since 1951 he became one of the Deputy Chief Designers of S.P. Korolev. In May 1952, he was appointed as Director of the leading research institute SRI-88 in the USSR, which included 25 Departments, a pilot plant, two branches and more than ten Design Bureaus, including SDB-1 of extremely ambitious and striving for its own one-man management in the missile industry of the USSR S.P. Korolev. Apparently, by so high appointment of M.K. Yangel, to whom S.P. Korolev had to obey, the wise Soviet leadership (first of all, represented by the Minister of Arms of the USSR, then Colonel-General D.F. Ustinov, who later became the Marshal of the USSR, three times Hero of Labor and the USSR and who had the largest number of orders of Lenin in our country – 10 [5]) sought to limit the rocket «monopoly» of S.P. Korolev. We indicate that the Chief Designer of SDB-1 S.P. Korolev showed himself not in the best circumstances for him [6, 7]: he defiantly did not attend the meetings held by his boss M.K. Yangel, often ignored the orders of the new Director of SRI-88 and, with great delays, carried out his decisions. It was from this period that the «difficult» personal and generally difficult relationships began between these legendary Soviet rocket designers. Understanding the situation, M.K. Yangel in October 1953 made an extraordinary decision – he submitted to his Minister an application to dismiss him from the post of Director of SRI-88 of his own free will. In November

1953, by the order of the indicated Minister D.F. Ustinov, he was dismissed from the post of Director and appointed as Chief Engineer of SRI-88. In such a way M.K. Yangel after fulfilling administrative duties again found himself in his native creative «environment»: he had the opportunity to develop a new direction in rocket science and technology – the use of high-boiling fuel components and an autonomous control system in ICBMs. At this time the «outcome» took place of persons who many did during the period 1945-1954 under the leadership of Wernher von Braun's colleague Helmut Gröttrup's leadership to lift Soviet rocketry technology of Russified German missile-rocket experts from the USSR to the German Democratic Republic [1].

2. The main achievements of M.K. Yangel in military rocketry (1954-1971). In April 1954, a Special Decree of the Council of Ministers of the USSR established the Special Design Bureau No. 586 (SDB-586, which became known as the Design Bureau «Southern» in 1966) on the basis of a serial rocket plant No. 586 (Dnepropetrovsk city), and M.K. Yangel was appointed as its Head and Chief Designer [7]. The main activity of M.K. Yangel and the SDB-586 headed by him has been developing and creating Soviet combat ICBMs. Work in the field of creating spacecrafts and the peaceful exploration of outer space was in the background for him. The first for M.K. Yangel missiles were rockets of medium (P-12) and medium (P-14) range [7, 8]. On June 22, 1957, the first and successful test was conducted at the Kapustin Yar training ground for the P-12 rocket that he created (in NATO terminology SS-4, Fig. 2) [9].

Fig. 2. Museum exhibit of a single-stage strategic missile of type P-12 (military index 8K63) on the launch pad (1957, chief designer – M.K. Yangel) [9]

Table 1 shows the main tactical and technical characteristics of the rocket of type P-12 (8K63), created in SDB-586 under the leadership of M.K. Yangel. This single-stage rocket with liquid high-boiling fuel was the first strategic missile developed at SDB-586 (Dnepropetrovsk city) [9, 10].

Table 1
The performance characteristics of the Soviet combat missile P-12 (8K63) with a thermonuclear charge [9]

No.	Name of characteristic	Value
1	Body length, m	21.1
2	Case diameter, m	1.65
3	Starting weight, t	41.7
4	Number of stages	1
5	TNT warhead mono-charge power, Mt	2.3
6	Range of flight (firing), km	2080
7	High boiling rocket fuel components: – brand of fuel – brand of oxidizing agent	TM-185 AK-27И
8	Period of being in service with the Strategic Missile Forces of the Soviet Army	1959-1988

Note that on the basis of the P-12 strategic missile (see Fig. 2), related to the first generation combat missiles and intended for ground launch, the SDB-586 developed the P-12У missile (military index 8K63У) with increased nuclear resistance blows of the probable opponent, intended for a mine start. Note that compared to the first rocket of type P-1 of S.P. Korolev [1], which was an exact copy of the German single-stage V-2 with liquid rocket engine (LRE) [11], the first P-12 rocket of M.K. Yangel produced in the amount of 2300 pcs and had been on combat duty for about 30 years [9], with almost the same diameter and greater length of the hull 1.5 times had a range of flight (firing) of about 7 times greater. The main reason for this was that the LRE of the P-1 rocket and all subsequent missiles of S.P. Korolev worked on low-boiling fuel (kerosene) with a liquid-oxygen oxidizer, and the rocket engines of all M.K. Yangel's rockets – on high-boiling fuel with new types of oxidizing agents. This was followed by work on the creation of the P-14 (8K65) missile with a firing range twice as large as that of the P-12 missile. The features of the P-14 rocket (in NATO terminology SS-5) were [10]: firstly, the use of НДМГ fuel; secondly, the use of a gyro-stabilized platform for an autonomous inertial missile control system, which allows to reduce instrumental errors in the control system and to provide higher accuracy of its fire. In June 1960, the first successful launch of the intermediate-range missile (up to 4000 km) P-14, developed by the SDB-586, was carried out according to the program of its flight design tests [10].

The legislative bodies of the USSR set for M.K. Yangel (Fig. 3) and his SDB-586 a new important task: the development of the ICBM project on high-boiling and long-stored fuel components. Such a missile became the P-16, which was created in a fairly short time. Preparation for the first launch of which on October 24, 1960 ended with the largest disaster in the history of domestic rocket science [10]. Then, during pre-launch work (about 15 minutes before the scheduled test launch of the first M.K. Yangel's ICBM), an unauthorized start of the second-stage engines of this ICBM occurred and the P-16 rocket (in NATO terminology SS-7) exploded right on the launch pad site of the Baikonur training ground [12]. In a fiery tornado, diverging in concentric waves from the launch center to a distance of up to 120 m, 76 people were immediately burned alive. Among them were [2, 12]:

commander of the Strategic Missile Forces of the USSR, Artillery Marshal M.I. Nedelin, chief designers of rocket systems, testers, militants and employees of a number of design bureaus. Subsequently, 16 more people died in hospitals due to burns and poisoning [12].

Fig. 3. Chief designer of the Soviet SDB-586, which in 1966 became known as the Design Bureau «Southern» (Dnepropetrovsk city), M.K. Yangel at the «zenith» of the heyday of design talent and creative work in the development and creation of powerful domestic military ICBMs with LRE (photo of the 1950s) [7]

Chief Designer M.K. Yangel miraculously survived this disaster: he and several other people, a few minutes before the explosion of the P-16 rocket, moved away from the place where it started to smoke [2, 12]. Mikhail Kuzmich hard endured this tragedy, which hit us hard, as they say, directly «under the breath» of the SDB-586 and its team. The tasks of strengthening the country's defense required the completion of work on the P-16 (8K64) missile. On February 21, 1961, the first successful launch of the P-16 (SS-7) ICBM, related to first-generation combat missiles, was carried out in the USSR [10, 12]. ICBM R-16 in front of all ICBMs of S.P. Korolev had a number of advantages [12]: firstly, it was refueled with new fuel components, which enabled it to be in a refilled state for up to 30 days, and then more; secondly, the rocket had an autonomous control system leading the P-16 to the target without any connection with the Earth; thirdly, it was easier to operate. Later, this missile was adopted and it formed the basis of the Strategic Missile Forces of the USSR.

In the early 1960s, the SDB-586 was actively engaged in the modernization of first-generation strategic combat missiles [13]: their main focus was the ampouled execution of the fuel tanks of the missiles and the possibility of their being in the refueled state for up to seven years. At this time, in the USA, a Titan-2 mine-based ICBM was created based on high-boiling fuel, capable of carrying a thermonuclear charge of high power. There were no such ICBMs in the USSR at that time. In this regard, the main Soviet missile design bureaus received from the country's legislative bodies tasks for the development of powerful missiles of heavy and superheavy classes. To achieve these goals, the SDB-586 proposed a project of a middle-class missile implemented in the P-36 missile system (military index 8K67, in NATO terminology SS-9) in ballistic and orbital versions of missiles [13]. On September 28, 1963, the first and successful launch of the P-36 rocket, belonging to the second generation of combat missiles, was carried out. Further, under the leadership of M.K. Yangel the SDB-586 creates an orbital ICBM with a military index of 8K69 [13]. This class of ICBMs had a unique property: with an unlimited range of fire, it can deliver a warhead for the defended state from two directions – from the front and rear, which forced the probable enemy to create missile defense on their borders simultaneously from two directions. Technically, this property was provided by a specific flight pattern of an orbital rocket along flat trajectories, including the trajectory of an artificial Earth satellite (AES) [13]. In December 1965, the first launches of such an orbital Soviet missile were carried out according to the program of its flight design tests. In August 1968, a new powerful ICBM of the second generation of SDB-586 development missiles, a missile with a military index of 8K67П, which is a modification of P-36 type ICBM with a military index of 8K67 and having a three-part warhead that is divided in flight, was launched from a Soviet test site [13]. In the period 1964-1980, 288 units were deployed in the USSR of the heavy P-36 ICBMs (SS-9 missiles, which were in 1965 the most powerful military missiles in the world with thermonuclear charges) with a launch weight of 183 tons and a warhead weight of 5.8 tons [12, 14].

In the late 1960s, the USSR experienced a quantum leap in the creation of strategic missile systems. The efforts of many domestic research institutes and design bureaus have developed reliable small-sized on-board digital computers, high-precision command instruments of missile control and aiming systems, thermonuclear charges with high specific combat characteristics, more advanced rocket propulsion systems, new schemes and methods of hardening launchers [15]. This became the basis for the creation of third-generation combat ICBMs. One of the main features of the third generation of military missile equipment of the USSR was the use of a «mortar launch» of missiles from a transport and launch container (TLC) [15]. With this type of launch, the rocket, due to the triggering of the powder charge installed in the lower part of the TLC (Fig. 4), flew out of the container (figuratively for the reader we say like a cork from a bottle of champagne), and then its rocket engines were launched in flight of the rocket outside the container. Decision of M.K. Yangel about the transition to this type of launch of ICBMs was so new and unusual that for many of his colleagues from SDB-586 it seemed simply fantastic and risky.

On September 2, 1969, the USSR Council of Ministers issued a secret decree «On the development and manufacture of the P-36M (15A14) missile system» (now it has been declassified), aimed at creating at Design Bureau «Southern» (successor since 1966 to the legendary SDB-586) of the combat heavy missile complex P-36M (military index 15A14, according to NATO terminology SS-18 «Satan») instead of a heavy ICBM of type P-36 (military index 8K67, SS-9) [14].

Fig. 4. Moment of loading of heavy combat ICBM of type P-36M (military index 15A14, in NATO terminology SS-18 «Satan»), placed in a massive fiberglass TLC, in the mine launcher (1978) [14]

The preliminary design of the Soviet two-stage heavy missile P-36M (15A14), carried out under the leadership of M.K. Yangel, was completed in record time – in December 1969 [14]. At the first stage of the P-36M rocket, a block of four-chamber closed-circuit LREs was used, and at the second stage, a single-chamber march closed-circuit LRE and four-chamber open-circuit steering LRE [14]. The composition of the separable warhead (SWH) of the P-36M (15A14) rocket included eight individual guidance (IG) units with thermonuclear charges [14]. The use of a more advanced design (lightweight units and their tight layout) and more efficient closed-circuit rocket engines in heavy combat ICBM P-36M allowed, with almost the same dimensions as of the combat ICBM P-36, to increase the launch mass of the missile to 209.6 t with a weight of its head part (HP) up to 8.8 t [14]. This missile was located in a thick-walled fiberglass TLC (see Fig. 4), which was installed in a converted mine launcher (ML) from the P-36 missile. The ML of a combat P-36M ICBM was a structure with a vertical barrel depth of 39 m and a diameter of 5.9 m and was distinguished by increased security and resistance to a nuclear strike by a likely enemy (Fig. 5) [14]. Figure 6 shows a general view of the museum exhibit of the Soviet heavy combat missile of the P-36M type, developed and created at the Design Bureau «Southern» (Dnepropetrovsk city) under the leadership of the Chief Designer M.K. Yangel [14-16].

Figure 7 captures the mine launch of the Soviet combat two-stage heavy ICBM of the P-36M type (military index 15A14, in NATO terminology SS-18 «Satan»), created at the Design Bureau 'Southern» [14].

Table 2 shows the tactical and technical characteristics of the Soviet combat ICBM P-36M (15A14) [14].

We point out that in January 1971 «throw» tests of the P-36M (15A14) missile were launched, during which its «mortar launch» was being worked out [14]. On February 21, 1973 (at that time the student and associate of M.K. Yangel, Academician of the Academy of Sciences of the Ukrainian SSR (since 1976) and of the Academy of Sciences of the USSR (since 1984), an outstanding scientist and designer of rocket and space

technology, twice Hero of Labor (1969, 1976) V.F. Utkin [17] became the Director and General Designer of the Design Bureau «Southern»;) flight design tests of the new P-36M (15A14) rocket complex began [14].

Fig. 5. General view of the ML with the Soviet P-36M type ICBM installed in it (military index 15A14, SS-18 «Satan») during maintenance of the missile by military personnel from folding platforms [14]

Fig. 6. General view of the museum exhibit of the Soviet military two-stage heavy ICBM of type P-36M (military index 15A14, SS-18 «Satan»), which became the most powerful strategic missile in the world in the 1970s [14]

Fig. 7. Moment of «mortar launch» from the ML of the Soviet military two-stage heavy ICBM of type P-36M (military index 15A14, in NATO terminology SS-18) [14]

Note that the tests of this complex with three types of combat equipment were completed in October 1975, and on December 30, 1975 the Soviet heavy P-36M ICBM (military index 15A14, in NATO terminology SS-18 «Satan») was adopted by the Strategic Missile Forces of the USSR [14].

The performance characteristics of the Soviet combat heavy ICBM P-36M (15A14, SS-18 «Satan») [14]

No.	Name of characteristic	Value
1	Body length, m	36.6
2	Case diameter, m	3.0
3	Starting weight, t	209.6
4	Number of stages	2
5	Charge power of the warhead in TNT equivalent, performed in four versions (monoblock: Mod 1 or Mod 2; SWH with IG: module 3 or module 4), kg	Module 3: SWH IG 8×900 kg; Module 4: SWH IG 8×750 kg
6	Range of flight (firing), km	- 16000 (light HP); - 11200 (heavy HP); - 10200 (SWH with IG)
7	High boiling rocket fuel components: – brand of fuel: – brand of oxidizing agent:	-Asymmetric dimethylhyd razine (ADMH); -Diazot tetraoxide (N_2O_4).
8	Fuel weight, t	188.0
9	Missile control system	Autonomous inertial
10	Thrust force of the first stage LRE, kN	- 4163 (at sea level); - 4520 (in vacuum).
11	Mass of the warhead of the missile, t	8.8
12	Specific impulse of the first stage of the missile, m/s	- 2874 (at sea level); - 3120 (in vacuum).
13	Missile launcher type	ML with «mortar launch»

Unfortunately, this day did not wait for our great designer of military rocketry, twice Academician (of the Republican and the Soviet Union's Academies of Sciences) M.K. Yangel, who died on October 25, 1971 in Moscow from another heart attack [2]. The Soviet combat heavy ICBM of type P-36M (15A14, SS-18 «Satan») was a triumph of the design talent of our compatriot M.K. Yangel. He created it not for attacking and destroying people, but for the sake of the survival of mankind in the frenzied nuclear arms race that has swept our entire world. And how many were in the USSR at the beginning of its development of opponents of this grandiose missile project? Even long-time associate of M.K. Yangel, chief designer of the Soviet ML E.G. Rudyak proved that the design of the P-36M (15A14) missile at its «mortar launch» [12] was inconsistent: «... *To throw, like an apple, a liquid colossus weighing more than two hundred tons is pure absurdity*». But M.K. Yangel turned this absurdity into a reality. By 1988, almost half of all thermonuclear warheads of the Strategic Missile Forces of our country were located in the USSR on this legendary ICBM [12].

Later, at the Db «Southern», taking into account the ideas and developments of M.K. Yangel, improved ICBMs of the third generation of mine military missiles [15] were developed: P-36M УТТХ missile systems (military index 15A18) equipped with SWH with 10 IG combat units, and MP-УР100 missile systems (military index 15A15, Fig. 8) and its improved version MP-УР100 УТТХ (military index 15A16), equipped with SWH with four IG combat units. In these developments of the ICBMs, all the achievements of Soviet science and missile technology available at that time were embodied. For M.K. Yangel work on the Soviet strategic missile systems P-36M (15A14, SS-18) and MP-УР100 (15A15, SS-17) became the «swan song». By the way, it took the United States five years for the practical implementation of the «mortar launch» after the USSR from the buried mines of its strategic ballistic missiles [14, 15].

Fig. 8. General view of the museum exhibit of the Soviet ICBM MP-УР100 (military index 15A15, in NATO terminology SS-17) with TLC developed and created at the Design Bureau «Southern» [18]

To complete the «picture» of the achievements of the DB «Southern» in the field of creation in the period 1980-1991 (at that time, its Directors and General Designers were already mentioned V.F. Utkin and a talented student of M.K. Yangel and V.F. Utkin, a famous Ukrainian designer of rocket and space technology, Doctor of Technical Sciences, Academician of the NAS of Ukraine (since 1992), Hero of Ukraine (2004) S.N. Konyukhov [19]) of high-performance powerful ICBMs of the fourth generation of combat missiles, we note that during their development the main areas of work were [20]: firstly, the creation of missiles capable of starting directly under the conditions of a nuclear strike on a positional area; secondly, the creation of mobile-based solid-fuel rockets, the survivability of which is achieved due to their mobility and uncertainty of location. Both of these areas were implemented in the P-36M2 «Voyevoda» missile systems (military index 15A18M, in NATO terminology SS-18-3) developed by the Design Bureau «Southern» with LRE of fixed-mine base and solid-fuel ICBMs of the PT-23 and PT-23 УТТХ «Molodets» type (military indices 115Ж60 и 15Ж61, in NATO terminology SS-24-1 and SS-24-2) of a mine and mobile railway base [20]. The scientific basis for the creation of these Soviet mobile missile systems was laid by the perspicacious and talented M.K. Yangel. With the

collapse of the USSR, work on the development and creation of new strategic missile systems at the Design Bureau «Southern» was discontinued [20].

3. The main achievements of M.K. Yangel in rocket and space technology for peaceful purposes (1961-1971). Note that in the field of creating spacecrafts (SCs) M.K. Yangel also achieved considerable success. Of particular interest here is the fact that M.K. Yangel, despite the «difficult» relationships with the Chief Designer of SDB-1 S.P. Korolev, took an active share in the 1960s in the creation in the USSR of a super-heavy launch vehicle of the H-1 type, designed for the flight of a Soviet manned spacecraft to the Moon [1]. M.K. Yangel had his own achievements in creating a similar P-56 launch vehicle (launch weight up to 1200 tons) at the SDB-586, which had only four LREs with a thrust of 640 tons each in its first stage [2]. In the design of the H-1 launch vehicle (Chief Designer – S.P. Korolev), 30 low-power LREs, operating simultaneously with kerosene and liquid oxygen, were to be installed at the first stage [2]. Further events in the implementation of the Lunar Program of the USSR showed that the wrong approach of S.P. Korolev to the choice of the type of the LRE for the first stage of the H-1 launch vehicle led to its explosion on the launch pad and the destruction of the launch complex. Accept S.P. Korolev position of M.K. Yangel, perhaps the Soviet cosmonaut would have entered the first in the history of mankind on the surface of the Moon. However, designed, manufactured and tested under the guidance of M.K. Yangel in low Earth orbit, the lunar module by the SDB-586 of the project H-1 − Л3 (block «E») was the only one in the USSR that was completely ready for space flight in the framework of the Soviet Lunar SC program [2]. As we can see, these data additionally emphasize the originality of the personality and the versatility of scientific and engineering talent of M.K. Yangel, who always sought to adapt and modify combat launch vehicles for their use in the peaceful exploration of outer space. The constantly growing needs of the regular launch in the USSR into orbits of satellites for various purposes made it necessary to refine the P-14 (8K65) combat missile at the SDB-586 with a view to using it as a space launch vehicle. Thus, the Space-1 launch vehicle was created [7]. On the basis of the two-stage combat rocket P-36 (8K67), the Space-2 space launch vehicle was developed [7]. The first launch of the Space-2 launch vehicle was carried out on August 18, 1964. A total of 700 launches of the Space-2 launch vehicle were made, which launched more than 1000 different spacecrafts into orbit. On the basis of the 8K69 military missile at the Design Bureau «Southern», the Cyclone-2 launch vehicle was created (Fig. 9), designed to launch military and civil spacecrafts into low circular and elliptical near-earth orbits [7, 16].

We point out that the first launch of the Cyclone-2 launch vehicle (Chief Designer – M.K. Yangel) took place on August 6, 1969 from the Baikonur Cosmodrome (Kazakhstan), and the last one in June 2006 [4]. Having finalized the powerful 8K69 military missile, the Design Bureau «Southern» created a three-stage Cyclone-3 launch vehicle. Its first launch with the SC took place from the Plesetsk Cosmodrome (RF) on June 24, 1977, and the last one in January 2009.

Fig. 9. Launch moment of the Cyclone-2 launch vehicle [4]

In May 1939, Irina Viktorovna Strazheva (Fig. 10) became the wife of the outstanding designer of space and rocket technology M.K. Yangel [7, 8]. In their family, a daughter Lyudmila and a son Alexander were born. I.V. Strazheva became a Doctor of Technical Sciences and worked as a Professor at the Moscow Aviation Institute (MAI) [2]. Note that since the end of the 1960s, the Chief Designer of Design Bureau «Southern» began to live in a service house. Before that, he lived for 12 years in a hotel in Dnepropetrovsk, and later in a small two-room apartment with the family of his son Alexander.

Fig. 10. Brilliant Soviet designer of rocket and space technology M.K. Yangel with his wife I.V. Strazheva, the grandchildren Dima and Seryozha (the children of their daughter Lyudmila) during their common summer vacation at Mikhail Kuzmich's cozy summer house near Moscow (1967, settlement of Barvikha, RF) [8]

4. Awards, distinctions and recognition of the merits of M.K. Yangel. This great designer in the field of rocket science and an aeromechanic scientist was awarded the following Soviet state awards and was awarded such honorary titles [2]:

- two gold medals of the Hero of Labor «Hammer and Sickle» (1959, 1961);
- four Orders of Lenin (1956, 1959, 1961, 1969);
- Laureate of the Lenin Prize (1960);
- Laureate of the USSR State Prize (1967);

- Academician of the Academy of Sciences of the Ukrainian SSR (1961);
- Academician of the Academy of Sciences of the USSR (1966);
- S.P. Korolev gold medal of the Academy of Sciences of the (1970);
- Order of the October Revolution (1971);
- Medal «For the Defense of Moscow» (1944);
- Honorary resident (citizen) of Baikonur.

President of Ukraine (in the period 1994-2005) L.D. Kuchma, who once worked as the Director of the «Yuzhmash» plant and had close contact with the Design Bureau «Southern» under the leadership of M.K. Yangel, as his grateful follower said [2]: «... *Yangel is a fantastically talented scientist and designer. Yangel lived without sparing himself. He lived without looking back, burning his life «fuel». For months and years at spaceports – in the uninhabited steppe and taiga*». The great designer of rocket and space technology died in Moscow from the fifth heart attack on the anniversary of his 60th Birthday – on October 25, 1971. He was buried with the required honors in Moscow at the Novodevichy cemetery (Fig. 11) [21]. Later, along with Mikhail Kuzmich, his son Alexander (in 1989) and his wife I.V. Strazheva (in 1995) were buried. As a result, the tombstone of M.K. Yangel and his relatives, in my opinion, began to emphasize the post-mortem family unity and objectivity took place in the intense life of this outstanding design scientist, the separation and simultaneity of his faithful service to both his family and two fraternal peoples – Russian and Ukrainian. I hope that with this argument the author did not violate not only the sculptor's intention, but also the peace of the deceased.

Fig. 11. Tombstone to the great Soviet designer of rocket and space technology, twice Hero of Labor M.K. Yangel (Novodevichy cemetery, Moscow) [21]

In 1991, to commemorate the great merits of the former Director and Chief Designer of the legendary SDB-586, Mikhail Kuzmich Yangel, to the national rocket science, his name was given to the State Enterprise DB «Southern» [2]. On the territory of the huge plant «Yuzhmash» and Design Bureau «Yuzhnoye» («Southern») named after M.K. Yangel a monument to the great domestic scientist-mechanic and designer of rocket and space technology M.K. Yangel (Fig. 12) who forever is in the «battle formation» of the illustrious team of the world leader in the development and creation of modern rocket technology was erected [22].

Fig. 12. Monument to the outstanding Soviet scientist-aeromechanics and Chief Designer of rocket and space technology M.K. Yangel installed in the territory of the «Yuzhmash» plant and the State enterprise Design Bureau «Yuzhnoye» («Southern») (1991, Dnepropetrovsk, Ukraine) [22]

Commemorative busts were installed in the city of Dnepropetrovsk and the city of Baikonur to the creator of the formidable Soviet survival rocket weapon [23]. Streets in Moscow, Kiev, Dnepropetrovsk, Baikonur, Vinnitsa and Bratsk were named after him [2]. Name of M.K. Yangelya was worn by the Kharkiv Institute of Radio Electronics (in the period 1982-1993). In the name of M.K. Yangel an asteroid, a crater on the Moon, a village in the Irkutsk region, a mountain peak in the Pamirs and an ocean cargo ship of the Russian Federation were named [2]. The Cosmonautics Federations of the USSR (RF) and Ukraine instituted medals named after him. Plaques in his honor now adorn the brick walls of the buildings of the State Enterprise Design Bureau «Southern» (Dnipro city, the former city of Dnepropetrovsk), CNIIMach (former SRI-88, the city of Korolev, Moscow Region) and the Moscow Aviation Institute (MAI, Moscow) (Fig. 13) [24].

Fig. 13. A memorial plaque on the building of the MAI, where his famous student of aircraft engineering, future Academician and outstanding Soviet designer of rocket and space technology M.K. Yangel studied (Moscow, RF) [24]

Conclusions. An outstanding Soviet scientist-aeromechanic and designer of dual-use rocket technology,

twice Hero of Labor, Academician of the Academy of Sciences of the Ukrainian SSR and of the Academy of Sciences of the USSR Mikhail Kuzmich Yangel made an invaluable contribution to strengthening the defense of the USSR during the Cold War. Under his scientific supervision, at the legendary SDB-586 (Design Bureau «Southern», Dnepropetrovsk city), highly effective combat intercontinental ballistic missiles were developed and created that formed the basis of our country's nuclear missile «shield». He went down in the history of world rocket science as the Chief Designer of the world's most powerful combat ICBM of the P-36M type (military index 15A14, according to NATO terminology SS-18 «Satan»), which carries huge thermonuclear charges in its divided warhead with individual guidance. The adoption in the USSR strategic missile forces of these powerful military intercontinental ballistic missiles with a firing range of (10.2-16) thousand km immediately «cooled» the hot heads of the militant forces representatives of the West and forced them to significantly reduce offensive nuclear weapons. Thanks to the titanic work of the Special Design Bureaus, which worked well in the USSR, including SDB-586, headed by M.K. Yangel, and the military industries, in the period 1960-1990 for the Soviet country parity in powerful nuclear missile weapons of enormous destructive power was provided. The present generations of grateful people of the planet are in eternal spiritual and moral debt to such bright and talented representatives of the human race as M.K. Yangel, who voluntarily gave themselves to the Altar of the Fatherland and laid down their lives for the sake of maintaining peace on Earth.

REFERENCES

1. Baranov M.I. An anthology of the distinguished achievements in science and technique. Part 51: Rocket-space technology designer Sergey Korolev and his accomplishments in missile design. *Electrical engineering & electromechanics*, 2019, no.5, pp. 3-11. **doi: 10.20998/2074-272X.2019.5.01.**
2. Available at: https://en.wikipedia.org/wiki/Mikhail_Yangel (accessed 12 June 2017).
3. Available at: https://www.google.com/search?q=Авиаконструктор+оликарпов&ie=utf-8&oe=utf-8&client=firefox-b (accessed 11 May 2018).
4. Available at: https://www.yuzhnoye.com/company/history/yangel.html (accessed 12 June 2017). (Rus).
5. Available at: https://www.mmsk.ru/people/unit/?id=46786 (accessed 12 September 2018). (Rus).
6. Gubarev V.S. *Neskol'ko stranits iz zhizni Mikhaila Kuz'micha Iangelia* [Designer. A few pages are from life of Mikhail Kuz'mich Yangel]. Moscow, Politizdat Publ., 1977. 110 p. (Rus).
7. Available at: http://rvsn.ruzhany.info/raznoe/jangel2.html (accessed 24 June 2018). (Rus).
8. Strazheva I.V. *Tiul'pany s kosmodroma* [Tulips from a space center]. Moscow, Molodaia gvardiia Publ., 1978. 399 p. (Rus).
9. Available at: https://www.yuzhnoye.com/company/history/rk_r_12.html (accessed 14 June 2017). (Rus).
10. Available at: https://www.yuzhnoye.com/company/history/first-generation-military-rockets.html (accessed 04 February 2018). (Rus).
11. Baranov M.I. An anthology of the distinguished achievements in science and technique. Part 50: Rocket-space technology designer Wernher von Braun and his accomplishments in missile design. *Electrical engineering & electromechanics*, 2019, no.4, pp. 3-11. **doi: 10.20998/2074-272X.2019.4.01.**
12. Available at: https://gorod.dp.ua/tema/persons/?pageid=211 (accessed 11 March 2018). (Rus).
13. Available at: https://www.yuzhnoye.com/company/history/second-generation-military-rockets.html (accessed 11 May 2017). (Rus).
14. Available at: http://oruzhie.info/raketi/405-r-36m (accessed 21 April 2018). (Rus).
15. Available at: https://www.yuzhnoye.com/company/history/third-generation-military-rockets.html (accessed 16 May 2018). (Rus).
16. Andreev L.V., Konyukhov S.N. Yangel. *Uroki i nasledie* [Lessons and legacy]. Dnepropetrovsk, Art-Press Publ., 2001. 521 p. (Rus).
17. Available at: https://www.yuzhnoye.com/company/history/utkin.html (accessed 26 July 2018). (Rus).
18. Available at: http://oruzhie.info/raketi/404-mr-ur-100 (accessed 06 December 2017). (Rus).
19. Available at: https://www.yuzhnoye.com/company/history/konyuhov.html (accessed 15 January 2018). (Rus).
20. Available at: https://www.yuzhnoye.com/company/history/fourth-generation-military-rockets.html (accessed 05 September 2018). (Rus).
21. Available at: http://www.warheroes.ru/hero/hero.asp?id=12779 (accessed 18 April 2018). (Rus).
22. Available at: http://www.warheroes.ru/hero/hero.asp?id=12781 (accessed 30 May 2018). (Rus).
23. Platonov V.P. *Iangel' sozdatel' oruzhiia vyzhivaniia* [Yangel creator of weapon of survival]. Dnepropetrovsk, IMA-Press Publ., 2011. 528 p. (Rus).
24. Available at: http://www.warheroes.ru/hero/hero.asp?Hero_id=12072 (accessed 13 May 2018). (Rus).

M.I. Baranov, *Doctor of Technical Science, Professor,*
Scientific-&-Research Planning-&-Design Institute «Molniya»,
National Technical University «Kharkiv Polytechnic Institute»,
47, Shevchenko Str., Kharkiv, 61013, Ukraine,
phone +380 57 7076841,
e-mail: baranovmi@kpi.kharkov.ua

K.M. Vasyliv, L.I. Mazurenko

A MATHEMATICAL MODEL OF THE ELECTRICAL ENGINEERING COMPLEX FOR DRIVE OF MAIN CIRCULATION PUMPS OF NUCLEAR REACTOR VVER-1000 OF NUCLEAR POWER PLANTS

Tools for computer investigation of the modes of operation of induction motors of the main circulating pumps of the VVER-1000 NPP reactor have been created. The mathematical model of the electrical engineering complex "synchronous turbogenerator of NPP unit – electric grid of power system – two transformers of own needs – four induction motors" in phase coordinates, oriented on explicit methods of numerical integration of the system of differential equations is developed. On the basis of the mathematical model the software designed for the study of electromagnetic and electromechanical processes of the system of induction motors of the main circulating pumps of the VVER-1000 nuclear reactor in the modes of: operative switching including start and run, switching to standby power, self-start of the motors with turbogenerator's run-out and without it is developed. The investigations of the processes in the system of induction motors in the mode of operative switching during their power supply from the turbogenerator are carried out and the basic regularities of their course in qualitative and quantitative relations are established.
References 10, figures 11.
Key words: **nuclear reactor, main circulation pumps, synchronous turbogenerator, transformer, induction motor, starting modes, self-starting, mathematical model, differential equations.**

Створено засоби комп'ютерного дослідження режимів роботи асинхронних двигунів головних циркуляційних помп ядерного реактора ВВЕР-1000 АЕС. Розроблено математичну модель електротехнічного комплексу: «Синхронний турбогенератор енергоблоку АЕС – електрична мережа енергосистеми – два трансформатори власних потреб – чотири асинхронні двигуни» у фазних координатах, орієнтовану на явні методи чисельного інтегрування системи диференціальних рівнянь. На базі математичної моделі розроблено програмне забезпечення, призначене для дослідження електромагнітних і електромеханічних процесів системи асинхронних двигунів головних циркуляційних помп ядерного реактора ВВЕР-1000 в режимах: оперативного перемикання включно з пуском і вибігом, переходу на резервне живлення, самозапуску двигунів з вибігом турбогенератора і без його вибігу. Виконано дослідження процесів системи асинхронних двигунів в режимі оперативного перемикання під час їх живлення від турбогенератора та встановлено основні закономірності їх перебігу в якісному та кількісному співвідношенні. Бібл. 10, рис. 11.
Ключові слова: **ядерний реактор, головні циркуляційні помпи, синхронний турбогенератор, трансформатор, асинхронний двигун, пускові режими, самозапуск, математична модель, диференціальні рівняння.**

Созданы средства компьютерного исследования режимов работы асинхронных двигателей главных циркуляционных насосов ядерного реактора ВВЭР-1000 АЭС. Разработана математическая модель электротехнического комплекса: «Синхронный турбогенератор энергоблока АЭС – электрическая сеть энергосистемы – два трансформатора собственных нужд – четыре асинхронных двигателя» в фазных координатах, ориентированная на явные методы численного интегрирования системы дифференциальных уравнений. На базе математической модели разработано программное обеспечение, предназначенное для исследования электромагнитных и электромеханических процессов системы асинхронных двигателей главных циркуляционных насосов ядерного реактора ВВЭР-1000 в режимах: оперативного переключения включительно с пуском и выбегом, перехода на резервное питание, самозапуска двигателей с выбегом турбогенератора и без его выбега. Выполнено исследование процессов системы асинхронных двигателей в режиме оперативного переключения при их питании от турбогенератора и установлены основные закономерности их протекания в качественном и количественном соотношении. Библ. 10, рис. 11.
Ключевые слова: **ядерный реактор, главные циркуляционные насосы, синхронный турбогенератор, трансформатор, асинхронный двигатель, пусковые режимы, самозапуск, математическая модель, дифференциальные уравнения.**

Definition of the problem and its relevance. Analysis of scientific publications. To date, 4 NPPs operate in the Ukrainian grid, with 13 VVER-1000 reactors and 2 VVER-440 reactors installed. Water-water nuclear power reactors of the VVER class are double-circuit [1-3]. The first circuit is intended for the removal of thermal energy from heat-emitting elements, which are installed in the core of the reactor and which contain nuclear fuel and the reaction of fission of nuclei under the influence of thermal neutrons takes place [1, 2]. Normal water serves as the coolant, which at the same time has the function of a neutron moderator, since the VVER reactors operate on thermal neutrons, that is, low-energy neutrons. The coolant circulates in the first circuit, the successive links of which are the following structural elements of the nuclear power plant: reactor core, main circulation pumps (MCPs), steam generators and water mains.

For extraction of heat from the reactor core, it is necessary to ensure the circulation of the coolant in the first circuit. This function is performed by the MCPs [2, 3]. At each of the VVER-1000 nuclear reactors, four main circulation pumps of the GCN-195M brand with power up to 6000 kW and coolant supply of 20,000 m³/h were installed. Each of these MCPs pumps the coolant through the reactor and the steam generator, which together with the pump and piping system form a single loop [2].

Each of the four MCPs is driven by a separate short-circuited induction vertical motor VAZ 215/109-6AM05 with 8000 kW power and 6.3 kV supply voltage [2, 4]. The main circulation pumps belong to the responsible own need (ON) mechanisms. It is natural that the mechanisms of the NPP's own needs are subjected to high requirements for the reliability of the electric power

supply of the motors, which propel these mechanisms and for the reliability of their operation. Failure of electric motors (EMs) of NPP's MCPs due to break of its power supply or their break may lead to a reactor emergency shutdown and a system failure – first circuit depressurization and, as a consequence, emission of radioactive elements into the atmosphere, which is dangerous for the life of the plant's personnel, damage to its basic equipment and the environmental impact. Therefore, for reliable electric supply of electric motors of the main circulating pumps of the VVER-1000 nuclear reactor, it is provided to use two power sources: working and standby [2, 4].

In order to comply with the rules specified in the instructions concerning the modes of operation of the EM of the MCP, it is necessary to have a clear and unambiguous understanding and reliable information about the course of electromagnetic and electromechanical processes that take place in these motors, in order to make timely correct decisions about their operative switching, conducting startup, switch to standby and emergency power, etc. The analysis of the literature indicates that the rules of operation of the EM of the MCP are stated only in job descriptions for NPP personnel [3], in which the algorithms of actions for the execution of these operations, including carrying out of profiles repairs and based solely on operating experience without a thorough analysis of the processes and problems of the motors operation modes.

The necessary information about the course of the processes can be obtained in two ways: 1) by conducting physical experiments directly on the electric motors of the MCP; 2) by conducting computer simulations using software developed on the basis of mathematical models of high-level adequacy. The first method is quite problematic due to the limitations of access to the systems of the EM of the MCP and the practical inability to carry out all the necessary experiments. The second one has no such restrictions, and therefore is considered promising.

The problem of the analysis of the modes of operation of electric motors of ON mechanisms of electric power plants is discussed in a rather large number of scientific works, and the material presented in these works is based on the classical theory of electric machines and presented in a general conceptual form, which makes it problematic to use it in a specific situation with motors of different types of different purposes and powers, as well as of the peculiarities of power supply curcuits. This means that in order to apply the provisions of these works in the practice of operating electric motors of specific ON units of power plants, significant refinements of these materials are required. In the light of the above, it is obvious that, to date, insufficient attention is being given to the development of information and technical means of analyzing the modes of operation of electric motors of the ON of power plants, which would be suitable for their immediate application in practice of operation of the power plants in general and NPPs in particular.

It is clear that more reliable information regarding the modes of operation of ON electric motors can be obtained on the basis of the solution of the system of differential equations, which describe the processes not only in steady but also in dynamic modes of operation of motors with the use of modern computer systems.

The above-mentioned suggests that the development of means of analysis of the modes of operation of electric motors of the own needs of NPPs, which are served by mathematical models and their corresponding software, is a relevant scientific and practical problem.

The goal of the paper is the development of a mathematical model and related software as a means of investigating the modes of operation of the induction motor (IM) system of the main circulating pumps of the VVER-1000 reactor of the NPP using modern computer technology.

Presentation of the main material. According to [2, 4], NPP's own-distribution switchgears are implemented with one assembled busbar system and one switch for connection. The number of sections of assembled busbars of the NPPs with voltage of 6.3 kV or 10.5 kV of normal operation is selected depending on: the number of MCPs, the allowed number of simultaneously connected MCPs without triggering the reactor emergency protection and the number and powers of installed ON operational transformers. On VVER-1000 reactors 4 MCPs are installed, drive induction motors of them motors are powered by the assembled busbars of 4 separate sections of normal operation (SNOs), the first two of which are powered by two secondary windings of the first working transformer of own needs (TON) of the first stage of transformation, and the primary winding of this transformer is connected to the first branch of the generating current lead. The other two SNOs are connected to the second branch of the generator current lead in the same way. Both working TONs are made with one primary and two secondary windings, which ensures the presence of four sections of normal operation per unit. Each of the two operational TONs of the unit on the base of the VVER-1000 nuclear reactor has power of 63 MVA.

Based on [2-4] and the above described, the system of electric motors of the MCP is referred to as an electrical engineering complex, the electrical circuit of which is shown in Fig. 1. The following system of designations is adopted in this Figure: the letter M denotes a three-phase electrical network that includes the power system together with the block transformer; TB, T1, T2, B1, B2, B3, B4 labels denote steam turbine, two operating TONs and four switches through which the stator windings of the induction motors are connected to the secondary windings of the TONs, and D1, D2, D3, D4 denote four asynchronous MCP's motors; letter G denotes synchronous turbogenerator (TG); letter F is the power source of the TG excitation winding; B5 is the generator switch for power unit; P1 – P4 are the main circulation pumps.

The other designations are: the letter φ denotes the potentials of the independent nodes of the circuit, the letter i denotes the currents of the phase branches of the structural elements, and the letter E denotes the electromotive force of the constant voltage source of the electrical circuit of the excitation of the turbogenerator. The lower indices indicate the numbers of independent nodes, the number of phase branches of the structural elements of the circuit and the numbers of the external

branches of the structural elements. The letters M, T, G, D, F in the lower indices indicate the belonging of currents to the external branches: network, transformers, turbogenerator, induction motors, the power source of the excitation winding; M_e and T_P inscriptions indicate belonging to the internal currents of the network and transformers. The letter S in the lower indices indicates the identity of the phase currents to the stators of the induction motors and the turbohenegator, and the letter R – to the currents of the rotors of the induction motors. The numbers in parentheses in the upper index of the currents indicate the element number of the group of one type (transformers, switches and motors) to which this current belongs.
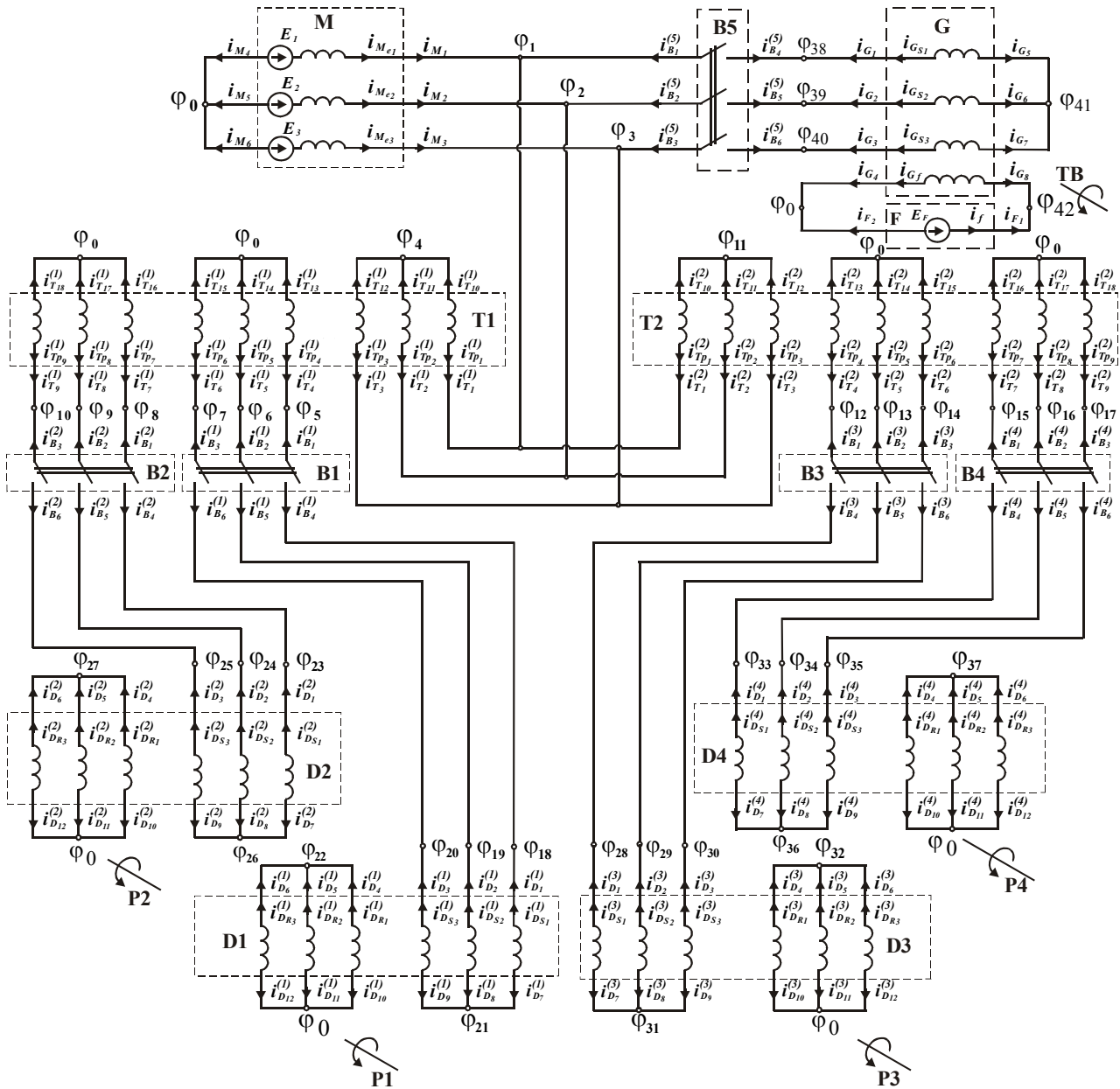
Fig. 1. Circuit diagram of the power circuit of the induction motor system of the MCP of the VVER-1000 nuclear reactor

For the practice of operation of the NPP unit on the basis of the VVER-1000 nuclear reactor, it is relevant to analyze the operation of the structural elements of the system of induction motors shown in the circuit of Fig. 1 in the following basic modes:

1) operation of the turbogenerator G in the normal mode on the power system M with the simultaneous electric power supply of the transformers of own needs T1, T2 and, accordingly, induction motors D1 – D4;

2) power supply of the TON from the power system through the block transformer when the turbogenerator is switched off;

3) operation of the MCP's induction motors in the situation of emergency shutdown with loss of connection with the power grid and shutdown of the turbogenerator due to the discontinuation of steam supply to the turbine, which translates TG into the run mode. Such a mode is indispensable for facilitating the transition to a natural coolant circulation in a nuclear reactor;

4) loss of power supply to the MCP's motors and the switch to the natural circulation of the coolant in the mode of the run of the units of the MCP (motors together with the pumps). To maximize run-time, which is critically important, induction motors are equipped with flywheels;

5) switching to the standby power supply of induction motors, followed by a short break in the supply of voltage to the TON for the duration of the automatic switching on of the reserve. Due to the re-supply of the voltage, the motors are restarted, that is, their further unwinding to the rated speed from the state in which there is less than the rated starting speed of the motors («self-start» in the literature);

6) mode of operative switching of MCP's induction motors.

The mathematical model of the electrical engineering complex (EEC) «TG-EM-T-IM» is developed on the basis of the theory of mathematical modeling of electromachine-valve systems (EMVS) [5] and a number of other developments presented in [6-10]. Thus, the mathematical model of the (EEC) «TG-EM-T-IM» is a system of differential equations of the electric state for the circuit of Fig. 1 and differential equations of mechanical state for induction motors together with MCP, turbogenerator with steam turbine, which serves as a source of primary mechanical torque of turbogenerator. The first system of equations describes the electromagnetic processes of the whole circuit of Fig. 1, and the second one – electromechanical processes occurring in induction motors and turbogenerators. The system of equations of electric state is written in phase coordinates and, together with equations of mechanical state, is oriented to explicit methods of numerical integration.

Each of the structural elements of the circuit (mains, transformers, switches, induction motors, turbogenerators, DC power source of the TG excitation winding) are represented by multipoles in the form of equations written by the second Kirchhoff law [5, 6].

Consider the mathematical models of structural elements of the electrical engineering complex on the example of a mathematical model of a turbogenerator.

System of equations of electrical and mechanical equilibrium of synchronous turbogenerator. According to [5, 8], a synchronous generator is represented by an eight-pole spanning three phases of the stator and the excitation winding, which is obtained by excluding the circuits of the damping winding represented by two circuits along the longitudinal d and the transverse q axis. The damping winding simulates the rotor array of the turbogenerator.

The electrical state of the synchronous generator is described by a vector equation of external branches that looks like this

$$p \, i_G + \Gamma_G \cdot \varphi_G + T_G = 0, \qquad (1)$$

where $p=d/dt$ is the differentiation operator in time t; $i_G = (i_{G_1}, i_{G_2}, i_{G_3}, i_{G_4}, i_{G_5}, i_{G_6}, i_{G_7}, i_{G_8})$ is the vector of currents of external branches; $\varphi_G = (\varphi_{38}, \varphi_{39}, \varphi_{40}, \varphi_0, \varphi_{41}, \varphi_{41}, \varphi_{41}, \varphi_{42})$ is the vector of external potentials of the generator;

$$\Gamma_G = \begin{bmatrix} L_G^{-1} & -L_G^{-1} \\ -L_G^{-1} & L_G^{-1} \end{bmatrix}; \quad T_G = \begin{bmatrix} L_G^{-1} \\ -L_G^{-1} \end{bmatrix} \times E \qquad (2)$$

are the matrix of coefficients and the vector of free terms.

The components of the matrix of coefficient and the vector of free terms in (2) are determined by the following formulas:

$$L_G^{-1} = (L_{e,e} - L_{e,i} \cdot L_{i,i}^{-1} \cdot L_{i,e})^{-1};$$

$$E = p_0 \, \psi^\gamma \, \omega_G + R \cdot i - L_{e,i} \cdot L_{i,i}^{-1} \cdot (p_0 \, \psi_D^\gamma \, \omega_G + R_D \, i_D); \quad (3)$$

$$L_{e,e} = \frac{L_d - L_q}{3} \begin{bmatrix} \cos(2\gamma) & \cos(2\gamma - \rho) & \cos(2\gamma + \rho) & 0 \\ \cos(2\gamma - \rho) & \cos(2\gamma + \rho) & \cos(2\gamma) & 0 \\ \cos(2\gamma + \rho) & \cos(2\gamma) & \cos(2\gamma - \rho) & 0 \\ 0 & 0 & 0 & 0 \end{bmatrix} +$$

$$+ \begin{bmatrix} \frac{L_d + L_q}{3} + \frac{L_0}{3} & \frac{L_0}{3} - \frac{L_d + L_q}{6} & \frac{L_0}{3} - \frac{L_d + L_q}{6} & \frac{L_{ad}}{K_i}\cos(\gamma) \\ \frac{L_0}{3} - \frac{L_d + L_q}{6} & \frac{L_d + L_q}{3} + \frac{L_0}{3} & \frac{L_0}{3} - \frac{L_d + L_q}{6} & \frac{L_{ad}}{K_i}\cos(\gamma - \rho) \\ \frac{L_0}{3} - \frac{L_d + L_q}{6} & \frac{L_0}{3} - \frac{L_d + L_q}{6} & \frac{L_d + L_q}{3} + \frac{L_0}{3} & \frac{L_{ad}}{K_i}\cos(\gamma + \rho) \\ \frac{L_{ad}}{K_i}\cos(\gamma) & \frac{L_{ad}}{K_i}\cos(\gamma - \rho) & \frac{L_{ad}}{K_i}\cos(\gamma + \rho) & \frac{3}{2} \cdot \frac{(L_{ad} + LGf)}{K_i^2} \end{bmatrix},$$

where $\rho = 2\pi/3$; K_i is the excitation current reduction coefficient of the stator current.

The matrix of mutual inductances between the stator and the excitation windings, on the one hand, and the circuits of the damping winding along the axes d, q, on the other hand, is as follows

$$L_{e,i} = \begin{bmatrix} L_{ad}\cos(\gamma) & L_{aq}\sin(\gamma) \\ L_{ad}\cos(\gamma - \rho) & L_{aq}\sin(\gamma - \rho) \\ L_{ad}\cos(\gamma + \rho) & L_{aq}\sin(\gamma + \rho) \\ \dfrac{3 \cdot L_{ad}}{2 \cdot K_i} & 0 \end{bmatrix}. \qquad (4)$$

The matrix of intrinsic inductances of the damper winding circuits is as follows

$$L_{i,i} = diag(L_{ad} + L_{\sigma dD}, \; L_{aq} + L_{\sigma qD}). \qquad (5)$$

The matrix of mutual inductances between the damping winding circuits and the external circuits (stator and excitation winding) is as follows

$$L_{i,e} = \frac{2}{3} \begin{bmatrix} L_{ad}\cos(\gamma) & L_{ad}\cos(\gamma - \rho) & L_{ad}\cos(\gamma + \rho) & \dfrac{3 \cdot L_{ad}}{2 \cdot K_i} \\ L_{aq}\sin(\gamma) & L_{aq}\sin(\gamma - \rho) & L_{aq}\sin(\gamma + \rho) & 0 \end{bmatrix} \quad (6)$$

Vectors ψ^γ, ψ_D^γ are determined by formulas

$$\psi^\gamma = L_{e,e}^\gamma i + L_{e,i}^\gamma i_D, \quad \psi_D^\gamma = L_{i,e}^\gamma i, \qquad (7)$$

where $L_{e,e}^\gamma$, $L_{e,i}^\gamma$, $L_{i,e}^\gamma$ are the derivatives of matrices $L_{e,e}, L_{e,i}, L_{i,e}$ by the angle of rotation γ; $i_D = (i_{Dd}, i_{Dq})$ is the vector of currents of the circuits of the damper winding; $i = (i_{G_{S1}}, i_{G_{S2}}, i_{G_{S3}}, i_{Gf})$.

In (4)-(7) L_d, L_q, L_0 are the inductances along the longitudinal, transverse axes and inductance of the zero sequence; L_{ad}, L_{aq} are the inductances that correspond to the yoke response along the longitudinal and transverse axes of the yoke; $L_{\sigma dD}$, $L_{\sigma qD}$ are the inductances of the scattering of the damping coil along the axes d, q.

We describe mechanical processes occurring in a turbogenerator by differential equations of mechanical

equilibrium, which has the following form:

$$(J_{TB} + J_G) \cdot p\omega_G - (M_{TB} - M_G) = 0, \quad (8)$$

where J_{TB}, J_G are the moments of inertia of the turbine and generator rotor; $p\omega_G$ is the derivative of the mechanical angular rotational speed of the generator rotor in time t; M_{TB} is the mechanical torque of steam turbine; M_G is the electromagnetic torque of the generator.

Taking into account that the differential equations of the electric and mechanical states of the mathematical model are oriented towards explicit methods of numerical integration, an important point in the algorithm of integration of these equations is the definition of the integration vector, which all the coordinates are systemized that are included in the differential equations under the sign of the derivative and which are solved directly by integration.

The integration vector for a synchronous turbogenerator has the following structure:

$$pv_G = (pi_{G_{S1}}, pi_{G_{S2}}, pi_{G_{S3}}, pi_{G_f}, pi_{G_d}, pi_{G_q}, p\gamma_G, p\omega_G), \quad (9)$$

where i_{G_d}, i_{G_q} are the currents of the damper winding along the axes d, q; γ_G, ω_G are the electric angle of rotation and the mechanical angular speed of the generator rotor.

The mathematical models of the switches were developed and described in [6] with the same approach (using the modular principle) as the mathematical model of the turbogenerator, and the mathematical models of the rest of the structural elements, including induction motors, were developed in a similar way based on [5, 8].

Direct integration of the system of differential equations of electrical and mechanical states is preceded by the formation and solution of a linear system of algebraic equations in the basis of the potentials of independent nodes in the electrical circuit of Fig. 1. For this purpose, derivatives of the currents of all electrical branches of the circuit are excluded from the system of differential equations of the electric state. Obtained in such a way system of linear algebraic equations of electric state has the following form [5, 6]:

$$A \cdot \varphi + B = 0, \quad (10)$$

where A is the matrix of coefficients; B is the vector of free terms; $\varphi = (\varphi_1, \varphi_2, ..., \varphi_{42})$, is the vector of the potentials of the independent nodes of the circuit of Fig. 1.

The matrix of coefficients A and the vector of free terms B of the system of equations (10) are formed from the matrices of coefficients, vectors of free terms, and incident matrices of the structural elements of the circuit of Fig. 1.

To the mathematical model of the electrical engineering complex of the circuit of Fig. 1 (apart from the system of differential equations of electrical and mechanical states) an automatic control system (ACS) is also included designed to stabilize the voltage of the turbogenerator while increasing and reducing the load on it, as well as to stabilize the rotation speed of the generator rotor which is driven by a steam turbine. To stabilize the generator voltage, a proportional-integral controller is used, the operation of which is described by the following equation:

$$u_F = K_{uP}(u_z - u_{GS}^V) + K_{ui}\int(u_Z - u_G)dt + u_{F0}, \quad (11)$$

where u_F, u_{F0} are the current and initial value of the excitation voltage; u_z, u_{GS}^V are the set value of voltage and module of imaging vector of phase voltages of the generator stator (their amplitude); K_{uP}, K_{ui} are the proportional and integral coefficients of the voltage regulator.

To stabilize the rotation speed of the generator rotor, a proportional-integral-differential controller is used, the operation of which is described by the following equation:

$$M_T = K_{\omega p}(\omega_z - \omega_G) + K_{\omega i}\int(\omega_z - \omega_G)dt + \\ + K_{\omega d} p(\omega_z - \omega_G) + M_{T0}, \quad (12)$$

where M_T, M_{T0} are the current and initial value of the mechanical torque of the turbine; ω_z, ω_G are the set value and current value of generator rotor rotation speed; $K_{\omega p}$, $K_{\omega i}$, $K_{\omega d}$ are the proportional, integral and differential coefficients of the generator rotor rotation speed controller.

The algorithm for the calculation of electromagnetic and electromechanical processes. The main input data are the catalog parameters of: electric network M; own need transformers T1, T2; induction motors D1, D2, D3, D4; turbogenerator G and DC voltage source F, as well as the initial conditions, which are systemized into a vector of integrated variables, having the following structure:

$$V = (V_M, V_T^{(1)}, V_T^{(2)}, V_B^{(1)}, V_B^{(2)}, V_B^{(3)}, V_B^{(4)},$$

$$V_D^{(1)}, V_D^{(2)}, V_D^{(3)}, V_D^{(4)}, V_B^{(5)}, V_G, V_F,$$

$$\int(u_z - u_{GS}^V)dt, \int(\omega_Z - \omega_G)dt, t) =$$

$$= (i_{Me1}, i_{Me2}, i_{Me3},$$

$$i_{Tp_1}^{(1)}, ..., i_{Tp_9}^{(1)}, i_{Tp_1}^{(2)}, ..., i_{Tp_9}^{(2)},$$

$$i_{B_1}^{(1)}, i_{B_2}^{(1)}, i_{B_3}^{(1)}, i_{B_1}^{(2)}, i_{B_2}^{(2)}, i_{B_3}^{(2)},$$

$$i_{B_1}^{(3)}, i_{B_2}^{(3)}, i_{B_3}^{(3)}, i_{B_1}^{(4)}, i_{B_2}^{(4)}, i_{B_3}^{(4)},$$

$$i_{DS_1}^{(1)}, i_{DS_2}^{(1)}, i_{DS_3}^{(1)}, i_{DR_1}^{(1)}, i_{DR_2}^{(1)}, i_{DR_3}^{(1)}, \gamma_D^{(1)}, \omega_D^{(1)}, \quad (13)$$

$$i_{DS_1}^{(2)}, i_{DS_2}^{(2)}, i_{DS_3}^{(2)}, i_{DR_1}^{(2)}, i_{DR_2}^{(2)}, i_{DR_3}^{(2)}, \gamma_D^{(2)}, \omega_D^{(2)},$$

$$i_{DS_1}^{(3)}, i_{DS_2}^{(3)}, i_{DS_3}^{(3)}, i_{DR_1}^{(3)}, i_{DR_2}^{(3)}, i_{DR_3}^{(3)}, \gamma_D^{(3)}, \omega_D^{(3)},$$

$$i_{DS_1}^{(4)}, i_{DS_2}^{(4)}, i_{DS_3}^{(4)}, i_{DR_1}^{(4)}, i_{DR_2}^{(4)}, i_{DR_3}^{(4)}, \gamma_D^{(4)}, \omega_D^{(4)},$$

$$i_{B_1}^{(5)}, i_{B_2}^{(5)}, i_{B_3}^{(5)},$$

$$i_{G_{S1}}, i_{G_{S2}}, i_{G_{S3}}, i_{Gf}, i_{Gd}, i_{Gq}, \gamma_{Gd}, \omega_{Gq},$$

$$\int(u_z - u_{GS}^V)dt, \int(\omega_Z - \omega_G)dt, t).$$

The main points of the process calculation algorithm are the following actions:

• on the basis of the initial conditions of the vector V (13) and the catalog data, the matrixes of coefficient and vectors of free terms of structural elements (for the turbogenerator (2)) are formed and through them the

matrix of coefficients A and the vector of free terms B of the system of equations of electric state (10), which is solved with respect to the vector φ;

• on the reverse course on the basis of the vector φ of the potentials of the independent nodes of the circuit of Fig. 1 the integration vector pV is defined equal to the derivative vector of integrated variables V (13) over time t ($pV = dV/dt$);

• one of the explicit methods of numerical integration, on the basis of the vector of integration pV and a given step of integration Δt, a new value of vector V is defined;

• the described procedure continues until the current time of integration t is exceeded beyond the specified final value.

According to the algorithm of the mathematical model, a software complex was developed. Below is a generalized analysis of electromagnetic and electromechanical processes occurring in the system of MCP's induction motors of a VVER-1000 nuclear reactor during the feed of transformers of own need (and thus of the induction motors) from a turbogenerator. In the actual operating conditions of the power unit, the rotational speed of the turbogenerator rotor is practically stable and corresponding to the frequency of the power grid voltage. In order to ensure such conditions, we use the possibility of a mathematical model and a software complex, which allows to provide a completely stable rotational speed of the generator rotor ω_G=const (although, as mentioned above, the mathematical model and the software package provide the possibility of calculation also the dynamic electromechanical process of the turbogenerator).

In this mathematical experiment, the corresponding ACS, described above (11), is used to stabilize the generator voltage during the operational switching of the MCP's induction motors.

The mathematical modeling results are the calculation dependencies of the basic coordinates, which include: the voltages and currents of all the electrical branches of the circuit of Fig. 1, the electromagnetic torques of IM and the moments of resistance of the MCP, as well as the rotational speed of the induction motors.

The input data are the catalog data of the turbogenerator, including the data of the power source of its excitation winding, induction motors, transformers of its own need and the electrical network. Here it is necessary to emphasize that the start-up AD of the MCP's IM of the VVER-1000 nuclear reactor is executed at total voltage of 6 kV (direct start), and the mechanical moment of inertia of the rotating mass of the rotor together with the flywheel is equal to 7250 kg·m². In addition, the input data includes information of an auxiliary character that determines the modes of operation of the software complex (integration step, end time of integration, etc.).

Simulation of electromagnetic and electromechanical processes is performed for the following mode of operation of MCP's induction motors: in the state of the moving with synchronous frequency rotor of the generator at the time taken by the initial ($t = 0$) the power source of the generator excitation winding is switched on. In the next stage, the first three IMs start in 5 s and at 5 s intervals (at times $t_1 = 5$ s,

$t_2 = 10$ s, and $t_3 = 15$ s). At time $t_4 = 30$ s, the third motor is switched on, and at time $t_5 = 40$ s, the fourth motor is also switched on. At time $t_6 = 70$ s, all three induction motors that are currently running (the first, the second and the fourth ones) are switched off.

Below are graphs of the calculated dependencies of the basic coordinates on time and their analysis for the physics of the processes and operation of the electrical engineering complex of the drive of induction motors of the main circulating pumps of the VVER-1000 nuclear reactor while powering the motors from the turbogenerator of the nuclear power plant unit.

In Fig. 2 the calculated dependencies of the generator stator phase voltages are shown.
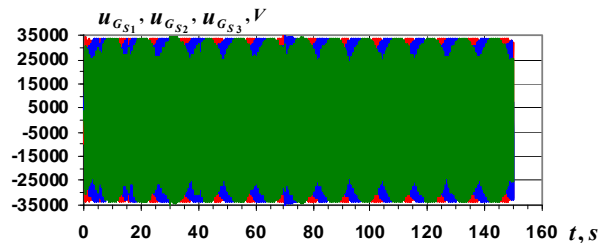
Fig. 2. u_{GS_1}, u_{GS_2}, u_{GS_3} – generator phase voltages

Figure 3 shows the calculated dependencies of the phase currents of the generator. The nature of phase voltages and currents in Fig. 2, 3 reflects the processes of start and switching off of induction motors. The amplitude of phase voltages in Fig. 2 remains constant under the action of the ACS, and the amplitude of phase currents in Fig. 3 varies depending on the induction motors operation.
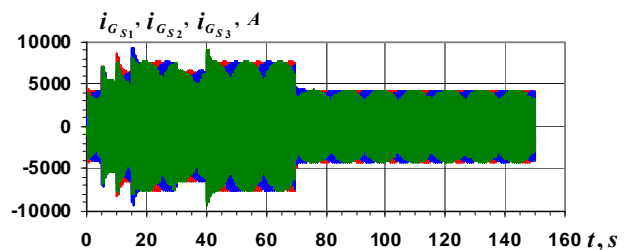
Fig. 3. i_{GS_1}, i_{GS_2}, i_{GS_3} – generator phase currents

More clear and substantive information about the nature of phase voltages and currents in this mode of operation of the generator is given by the calculated dependences of the modules of the pictorial vectors of phase voltages and stator currents of the generator, which are shown in Fig. 4.
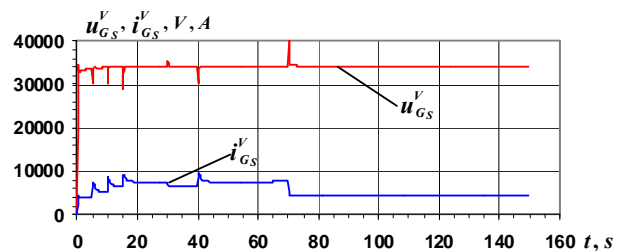
Fig. 4. u_{GS}^V, i_{GS}^V – modules of pictorial vectors of phase voltages and currents of the stator of the turbogenerator

The nature of the voltage and current curves in Fig. 4 clearly illustrates the patterns of change in the amplitude of the phase voltages and currents of the generator stator in the mode of operational switching of the IM, as well as the reaction and consequences of the action of the voltage ACS.

From Fig. 3, 4 it can be seen that during the period when the IMs are switched off ($t > 70$ s) the generator phase currents do not equal zero, although the voltage remains stable. This is due to the fact that at this interval both transformers of own need which are connected to the generator, operate in idle mode, and therefore in their primary windings the current does not equal zero in the situation with the motors switched off and has the value corresponding to this mode.

Functionally important information regarding the generator includes information about the nature of its voltage and excitation current. Therefore, in Fig. 5 the calculated dependencies of these coordinates are shown.

Fig. 5. u_{Gf}, i_{Gf} – voltage and current of the turbogenerator excitation

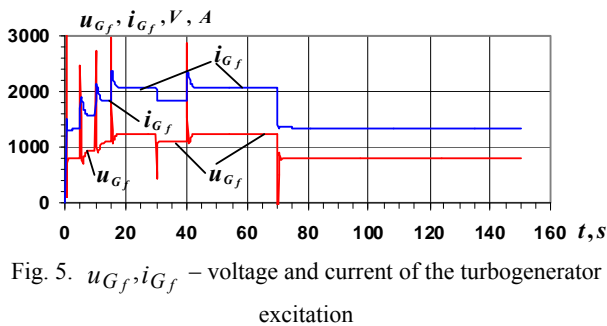It is worth noting again that the ACS of the generator stator voltage operates precisely on the function of the module of the pictorial vector of phase voltages (11).

From the point of view of the operation of the MCP's induction motor system, it is important to have information about the main coordinates (voltages and currents) of the TON. In this context, let us consider and analyze the voltages and currents of the primary and two secondary windings of the first TON. In Fig. 6 the calculated dependencies of the modules of the pictorial vectors of the phase voltages of the primary and two secondary windings of the first TON are shown.
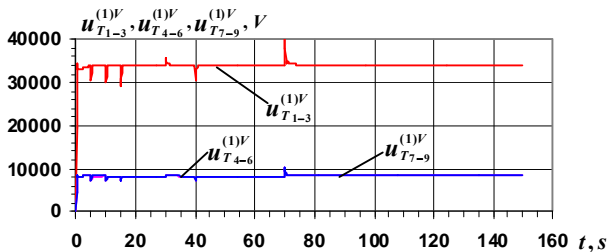

Fig. 6. $u_{T1-3}^{(1)V}, u_{T4-6}^{(1)V}, u_{T7-9}^{(1)V}$ – modules of the pictorial vectors of the voltages of the windings of the first transformer of own need

The Figure shows that the voltage of the primary winding is very close to the voltage of the generator in Fig. 4, and the voltage of the two secondary windings, the values of which coincide, corresponds to the current voltage value of 6.3 kV, which feeds the induction motors of the MCP. It is obvious that the voltages of the primary and two secondary windings of the second TON will be identical with the voltages of the first TON (Fig. 6).

Similarly to voltages, let us consider the winding currents of both transformers of own need. The modules of pictorial vectors of currents of the primary and two secondary windings of the first TON are shown in Fig. 7.
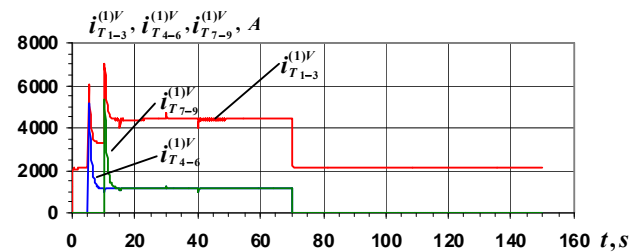
Fig. 7. $i_{T1-3}^{(1)V}, i_{T4-6}^{(1)V}, i_{T7-9}^{(1)V}$ – modules of the pictorial vectors of the currents of the primary and secondary windings of the first TON

As for the first one, the modules of the pictorial vectors of the currents of the primary and two secondary windings of the second TON are shown in Fig. 8.
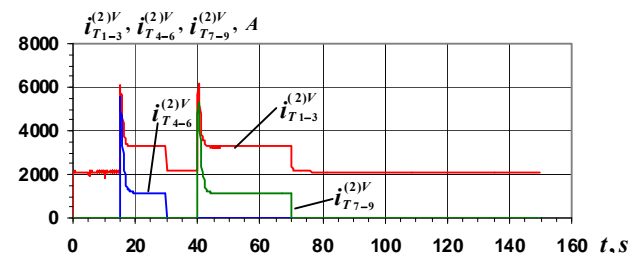
Fig. 8. $i_{T1-3}^{(2)V}, i_{T4-6}^{(2)V}, i_{T7-9}^{(2)V}$ – modules of the pictorial vectors of the currents of the primary and two secondary windings of the second TON

The calculated dependencies of the modules of the pictorial vectors of the secondary windings of the first and second TONs, which are shown in Fig. 7, 8 clearly illustrate the modes of operation of induction motors fed from the secondary windings of the TON. These Figures unambiguously and clearly show the moments of switching on and off of all four IMs, as well as the nature and frequency of the starting currents. The curves in Fig. 7, 8 also carry information on the nature and correlation of the primary and secondary windings of the TON, and together with Fig. 4 also about the ratio of the currents of the primary windings of the TON and the turbogenerator.

In the secondary windings of the transformers, the same currents flow as in the corresponding stator windings of the induction motors, which are connected by the switches. Therefore, the analysis of the currents of the secondary windings of the transformers serves at the same time for the currents of the IM stators. But to obtain more complete information about the IM stator windings currents, here we present only the instantaneous values of the phase currents of one of the randomly selected induction motors, which is the first. Therefore, the calculated dependencies of the instantaneous values of the phase currents of the first IM are shown in Fig. 9.

Fig. 9. $i_{D_{S1}}^{(1)}$, $i_{D_{S2}}^{(1)}$, $i_{D_{S3}}^{(1)}$ – instantaneous phase currents of the stator winding of the first induction motor

It can be seen from the Figure that the curve of the module of the pictorial vector of the currents of the first secondary 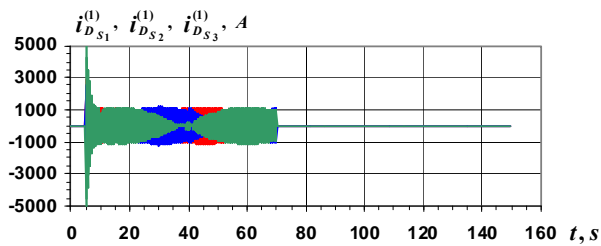winding of the first transformer $i_{T4-6}^{(1)V}$ in Fig. 7 is such that goes around the current curves in Fig. 9, which uniquely responds to the physics of electromagnetic processes occurring in the system of the MCP's IM in accordance with the circuit in Fig. 1.

Above, we have considered and analyzed the electromagnetic processes described by the electrical coordinates to which the voltages and currents belong.

For the sake of completeness of information regarding the possibilities of the mathematical model and software complex in the analysis of modes of operation of induction motors of the MCPs of the VVER-1000 nuclear reactor, let us analyze the electromechanical processes, which are regarding IMs described by their rotational electromagnetic torques and mechanical moments of resistance of the MCP. Figure 10 shows the calculated dependencies of these coordinates.

It can be seen from the Figure that at the stage of acceleration of the first IM and, accordingly, the first MCP, the electromagnetic moment of the motor is substantially greater than the moment of resistance. In steady state, they are balanced, and at the run-out stage the electromagnetic torque of the motor is zero, and the mechanical torque decreases with the regularity of the decrease of the mechanical angular frequency of the motor with the pump according to the mechanical characteristics of the whole MCP unit. It is obvious that the regularities of the electromechanical processes of the other three motors are analogous, so there is no need to state them.
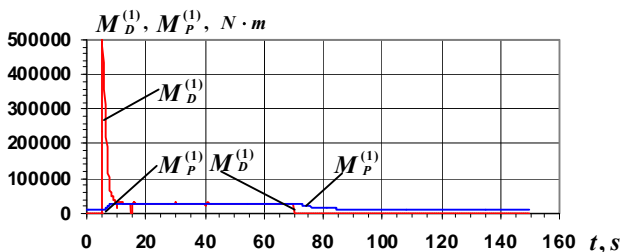

Fig. 10. $M_D^{(1)}$, $M_P^{(1)}$ – electromagnetic torque of the first induction motor and the moment of resistance of the first MCP

When it comes to the analysis of electromechanical processes of the MCP's IM of the VVER-1000 nuclear reactor, it is fundamentally important to have information about the nature and regularity of changes in the mechanical angular frequencies of rotation of the IM rotors, since these coordinates determine the productivity

of the MCP operation and, respectively, the operation of both the nuclear reactor and the unit as a whole. Therefore, Fig. 11 shows the calculated dependencies of the mechanical angular rotation frequencies of the MCP's induction motors.
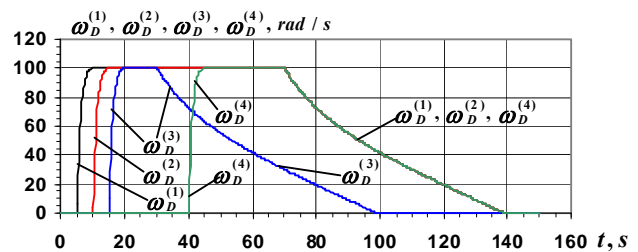

Fig. 11. $\omega_D^{(1)}$, $\omega_D^{(2)}$, $\omega_D^{(3)}$, $\omega_D^{(4)}$ – mechanical angular rotational speeds of MCP's induction motors

The Figure (as opposed to the Figures with curves of the currents) clearly shows not only the moments of switching on and off the IM, but also the time of their acceleration and running to a complete stop. Such information is critically important in ensuring the successful transition to the natural circulation of the coolant in a nuclear reactor in the event of an emergency shutdown of the power unit. To this end, the MCP's motors are further equipped with flywheels to increase the unit's run-time by the IM-MCP system.

Generalized analysis of curves in Fig. 11 and the curves of all other coordinates (the torques in Fig. 10, currents and voltages in all other Figures) shows that their character is fully consistent and fully interconnected in terms of the regularities of the electromagnetic and electromechanical processes, and at the same time it indicates a sufficiently high level of adequacy of both mathematical and numerical models. This result was achieved by describing electromagnetic and electromechanical processes by a single system of differential equations, including the ACS of the generator voltage and the rotor speed of the generator.

In the future, it is planned to carry out the research and to analyze the processes, including the transition to standup power, restart (self-start) of the IMs, as well as the analysis of the already mentioned modes of operation taking into account the dynamics of the generator rotor.

Important prospective studies (the necessity of which is especially emphasized in the scientific and technical literature [2, 4]) include the study of modes of operation of MCP's IMs during the transition to the natural circulation of the coolant of the nuclear reactor with the use of turbogenerator, which is obviously is of theoretical and practical interest in the operation of NPPs units based on the VVER-1000 nuclear reactor.

Conclusions.

1. Analysis of scientific literature indicates that the features of operation of electric motors of the MCP are stated only in the official instructions for NPP personnel, which stipulates the rules of operation: start-up, self-start, shutdown, switching to alternative power sources without a substantive scientific analysis of the regularities of the course of electromagnetic and electromechanical processes. There is clearly a lack of specific scientific research on this issue in scientific literature. The presence

of mathematical models and related software as a computer research tool would allow to investigate the modes of operation of the MCP's IMs system of the VVER-1000 nuclear reactor, necessary both in theoretical and practical aspects of exploitation of the NPP units.

2. A mathematical model of the system of MCP's induction motors has been developed, which takes into account the most important determinants that influence the course of electromagnetic and electromechanical processes, including: the mutual influence of the structural elements of the circuit of the IM system, the influence of the ACS on the operation of the TG excitation system, mutual influence of IMs and MCPs, which are driven by these motors, and also allows to study the operation of the MCPs during the self-start of the IMs and their operation during the run-out of the TG rotor.

3. A mathematical model has been developed that allows to study the most important modes of operation of the system of induction motors of MCPs with the help of modern computer technology.

4. In the first approximation, the study of electromagnetic and electromechanical processes of the system of induction motors of MCPs is carried out. In particular, the starting modes are investigated, the qualitative and quantitative parameters of the run-out of motors with large fly masses are obtained, which (according to the authors) is also the subject of a new scientific result.

REFERENCES

1. Baranov M.I. An anthology of the distinguished achievements in science and technique. Part 44: Traditional power engineering. Nuclear power stations: retrospective view, state and prospects of their development. *Electrical engineering & electromechanics*, 2018, no.3, pp. 3-16. **doi: 10.20998/2074-272X.2018.3.01.**

2. Topolnytskyi M.V. *Atomni elektrychni stantsii* [Nuclear power stations]. Lviv Polytechnic National University Publ., 2004. 562 p. (Ukr).

3. Shevchenko V.V., Kosmyn S.M. Features of work of drives engines technological pumps of reactor area of nuclear power plant. *Transactions of Kremenchuk Mykhailo Ostrohradskyi National University*, 2010, no.4(63), part 2, pp. 79-83. (Rus).

4. Feldman M.L., Chernovets A.K. *Osobennosti elektricheskoi chasti atomnykh elektrostantsii* [Features of the electrical part of nuclear power plants] Leningrad, Energoatomizdat Publ., 1983. 172 p. (Rus).

5. Plakhtyna E.H. *Matematicheskoe modelirovanie elektromashinno-ventil'nykh sistem* [Mathematical modeling of electric machine-valve systems]. Lvov, Vyshcha shkola Publ., 1986. 164 p. (Rus).

6. Vasyliv K.M. A mathematical model of thermal power plants smoke exhausters induction motors system operation modes. *Electrical engineering & electromechanics*, 2017, no.3, pp. 19-26. **doi: 10.20998/2074-272X.2017.3.03.**

7. Poliak N.A. *Sovremennye krupnye dvukhpoliusnye turbogeneratory. Elektromagnitnye kharakteristiki* [Modern large bipolar turbogenerators. Electromagnetic characteristics]. Moscow, Energiya Publ., 1972. 472 p. (Rus).

8. Fylts R.V. *Matematicheskie osnovy teorii elektromekhanicheskikh preobrazovatelei* [Mathematical foundations of the theory of electromechanical converters]. Kyiv, Naukova dumka Publ., 1979. 208 p. (Rus).

9. Kopylov I.P. *Elektricheskie mashiny*. [Electrical machines]. Moscow, Vysshaia shkola Publ., 2006. 607 p. (Rus).

10. Krause P.C., Wasynczuk O., Sudhoff S.D. *Analysis of Electric Machinery and Drive Systems*. IEEE Press, 2002. 632 p.

K.M. Vasyliv[1]*, Doctor of Technical Science, Professor,*
L.I. Mazurenko[2]*, Doctor of Technical Science, Professor,*
[1] Lviv Polytechnic National University,
12, S. Bandera Str., Lviv, 79013, Ukraine.
[2] The Institute of Electrodynamics of the NAS of Ukraine,
56, prospekt Peremogy, Kiev, 03057, Ukraine,
e-mail: karl.vasyliv@gmail.com,
mlins@ied.org.ua

V.I. Milykh, L.V. Shilkova

NUMERICAL-FIELD ANALYSIS OF THE CHARACTERISTICS OF A THREE-PHASE MAGNETIC FIELD INDUCTOR FOR THE TREATMENT OF VARIOUS SUBSTANCES WITH CURRENT STABILIZATION

Introduction. A three-phase magnetic field inductor (MFI) similar to the asynchronous motor stator, which provides processing of various substances, is considered. This is done by means of oblong ferromagnetic elements moving with a rotating magnetic field and located in its cylindrical working chamber. Problem. The aim of the work is to develop the theory and conduct practical calculations of the parameters and characteristics of the MFI that connect the electromagnetic quantities and their phase relationships in the mode of its load. Methodology. The studies are carried out on the basis of numerical calculations of the magnetic field in the MFI taking into account the ferromagnetic elements in its working chamber. The calculation model of the chamber is represented by a homogeneous anisotropic magnetic medium for which the method of determining different magnetic permeabilities by its longitudinal and transverse axes is given. In order to obtain the characteristics of the presented MFI, the method of determining the electromagnetic parameters and phase relationships of the quantities accompanying its operation has been developed. Results. The theory and results of numerical-field analysis of electromagnetic quantities, their phase relationships and corresponding characteristics of three-phase MFI are presented. Calculations of characteristics are made for the inductor load mode depending on the phase shift of the magnetomotive force of the stator winding relative to the longitudinal axis of the chamber and while ensuring the constant value of the current of this winding. The characteristics include magnetic flux coupling, EMF and stator winding voltage, phase shifts between them and current, electromagnetic moment, input and output power, electrical and magnetic loss power, power factor and efficiency. Practical value. The technique of numerical-field calculations of electromagnetic quantities and their phase relationships is developed, and also the set of characteristics which should promote designing and perfection of inductors of the considered type is received. The presented technique is universal as it allows to display their cores practically of any shape. References 11, figures 10.*
Key words: **magnetic field inductor, asynchronous motor stator, theory, numerical-field calculations, electromagnetic quantities, phase relationships, characteristics.**

Розглянуті теорія і результати чисельно-польового аналізу електромагнітних величин, їх фазових співвідношень і відповідних характеристик трифазного індуктора магнітного поля. Індуктор подібний до статора асинхронного двигуна і забезпечує обробку різних речовин. Це відбувається за допомогою довгастих феромагнітних елементів, що знаходяться в його робочій камері і рухаються з обертовим магнітним полем. Розрахункова модель камери представлена анізотропним магнітним середовищем з різною магнітною проникністю по її подовжній і поперечній осям. Розрахунки характеристик виконані в режимі навантаження індуктора залежно від фазового зсуву магніторушійної сили обмотки статора відносно подовжньої осі камери і при забезпеченні незмінної величини струму цієї обмотки. Отримана сукупність характеристик повинна сприяти проектуванню і вдосконаленню індукторів розглянутого типу. Надана методика є універсальною і дозволяє відображати їх осердя практично будь-якої форми. Бібл. 11, рис. 10.
Ключові слова: **індуктор магнітного поля, статор асинхронного двигуна, теорія, чисельно-польові розрахунки, електромагнітні величини, фазові співвідношення, характеристики.**

Рассмотрены теория и результаты численно-полевого анализа электромагнитных величин, их фазовых соотношений и соответствующих характеристик трехфазного индуктора магнитного поля. Индуктор подобен статору асинхронного двигателя и обеспечивает обработку различных веществ. Это происходит с помощью движущихся с вращающимся магнитным полем продолговатых ферромагнитных элементов, находящихся в его рабочей камере. Расчетная модель камеры представлена анизотропной магнитной средой с разными магнитными проницаемостями по ее продольной и поперечной осям. Расчеты характеристик проведены в режиме нагрузки индуктора в зависимости от фазового сдвига магнитодвижущей силы обмотки статора относительно продольной оси камеры и при обеспечении неизменной величины тока этой обмотки. Полученная совокупность характеристик должна способствовать проектированию и совершенствованию индукторов рассмотренного типа. Представленная методика является универсальной, так как позволяет отображать их сердечники практически любой формы. Библ. 11, рис. 10.
Ключевые слова: **индуктор магнитного поля, статор асинхронного двигателя, теория, численно-полевые расчеты, электромагнитные величины, фазовые соотношения, характеристики.**

Introduction. In a number of industries, magnetic mixers and separators are used to provide technological processes for mixing different mixtures or separating small objects with different electromagnetic properties [1-3]. The structure and nature of magnetic fields (MFs), which provide these processes, are very diverse. Among them are rotating MFs, which are excited by an inductor similar to the stator of a three-phase asynchronous motor (TAM).

The difference between such a magnetic field inductor (MFI) and a TAM is that instead of a rotor, a working chamber (WC) is located inside the stator, through which a liquid or loose dry mixture is passed that needs to be processed. This is carried out using small ferromagnetic elements (FEs) moving with a rotating MF and creating the so-called «vortex layer» in the WC [1, 3]. It is assumed that the FEs are made, for example, in the

form of needles or short pieces of iron wire, and they are uniformly distributed over the WC, the thin-walled shell of which is made of non-magnetic material and does not interact with MF.

An analysis of the literature shows that MFIs, despite the wide range of applications in various industries, is still not well understood. The fact is that the study of their electromagnetic parameters is carried out, as a rule, based on the theory of magnetic circuits. But in conditions of very large gaps and anisotropic low-magnetic space, the representation of the MFI structure by several homogeneous sections of the magnetic circuit is problematic.

New opportunities in research and improvement of the design of MFI appeared with the development of software for numerical calculations of MF. Their effectiveness for MFI was already shown in [4] when analyzing the MF in its transverse and longitudinal sections based on plane-orthogonal calculation models.

A working tool for the numerical calculation of the MF in [4] and in this work, a publicly available and widespread FEMM code [5] was adopted.

In the aforementioned works, MF calculations are limited to considering the ideal idling (II) mode, i.e. without the presence in the working chamber of MFI FE. These studies have provided useful information, but cannot be the end result. More advanced calculations should be aimed at studying the electromagnetic parameters and characteristics of the MFI in the load mode, which will show the essence of the operation of the MFI as part of the main device − the mixer or separator. And here the main problem is accounting of the filling of the working chamber with the FE, providing the working process.

Therefore, **the goal of this work** is to study the characteristics of the MFI in its load mode based on numerical calculations of the MF taking into account the weakly magnetic medium in its working chamber. For this, the relations of electromagnetic parameters and phase quantities in the presented MFI with a rotating magnetic field created by a three-phase winding in a working chamber filled with FE are derived.

Object of study. The electromagnetic system of the MFI is the same as in [4]. It is shown in Fig. 1 only by its cross section, which is enough to achieve the goal of this work. Rectangular (x, y) and the polar (r, α) coordinate systems with the origin of the angle from the y axis are here designated and further used.

For technological reasons, the MFI parameters were set: the radius of the working chamber $r_{re} = 0.15$ m, the active length along the axial axis $l_a = 0.3$ m. The MF inside the WC is distributed almost uniformly with magnetic flux density (MFD) in the center of 0.24 T in the ideal idle move. For this mode, the stator voltage and current are considered nominal.

The remaining parameters of the inductor are calculated by a technique close to the classical one for TAM [6], taking into account the absence of a rotor. Of the main parameters of the inductor, we present: the nominal phase voltage $U_{sN} = 220$ V and current $I_{sN} = 950$ A, the frequency $f_s = 50$ Hz. It has the number of phases $m_s = 3$ and pairs of poles $p = 1$, the number of slots

$Q_s = 42$; the number of consecutive turns of the phase winding $N_s = 28$. The radius of the bore of the core of the inductor r_{si} is 0.175 m, since it should be slightly larger than the radius of the WC in order to exclude from it an annular gap with insufficiently homogeneous MF. The inductor winding is two-layer, distributed, with relative shortening $\beta_s = 18/21$, the connection circuit is «star».

The MFI core is made of 2013 electrical steel, the sheet thickness is 0.5 mm, the filling factor $K_{Fe} = 0.97$.
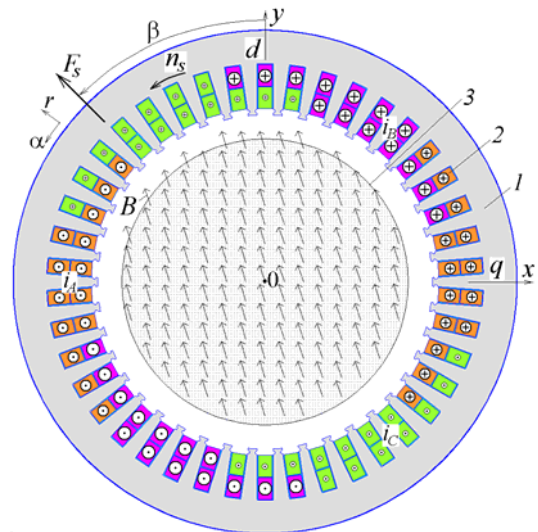
Fig. 1. Electromagnetic system of the MFI: 1 – laminated core; 2 – three-phase winding; 3 – working chamber

Fundamentals of numerical-field calculations. The source of a rotating MF in a MFI is a three-phase symmetric system of currents in the stator phase winding rods (Fig. 1):

$$
\begin{aligned}
i_A &= I_m \cos(\omega t + \beta); \\
i_B &= I_m \cos(\omega t - 2/3\pi + \beta); \\
i_C &= I_m \cos(\omega t + 2/3\pi + \beta),
\end{aligned}
\tag{1}
$$

where $I_m = \sqrt{2} I_s$ is the amplitude of the currents in the stator winding rods at the current value of the phase currents I_s; $\omega = 2\pi f_s$ is the angular frequency; t is the time; β is the initial phase of the currents, which sets the necessary for the specific mode of calculating of the MF shift of the direction of the MMF of the stator winding F_s from the y axis.

Figure 1 shows the directions of currents in the winding rods at $t = 0$ and $\beta = 45°$, and also shows the scaled distribution of the MFD vectors B in the corresponding load mode, in which the MF rotates with frequency n_s. It can be seen that the MF in the WC is almost uniform. As for the MMF of the stator winding F_s, it is oriented clearly at a given angle β.

The MF of the inductor in its central cross section is described by the well-known 2D differential equation:

$$
\mathrm{rot}\left[\frac{1}{\mu_e} \mathrm{rot}\left(\vec{k} A_z \right) \right] = \vec{k} J_z ,
\tag{2}
$$

where A_z, J_z are the axial components of the magnetic vector potential (MVP) and current density, respectively; $\vec{k}$ is the unit vector along the axial axis z; μ_e is the absolute magnetic permeability (AMP).

The research tool presented to be the numerical calculations of MFs by the Finite Element Method using the FEMM code [5] with the control it by the created Lua script like [7].

When calculating the MF, the distribution of AMP in the laminated steel core and non-magnetic space is taken into account by the well-known method. In the MFI, the problem of taking into account the magnetic properties of the medium located in the WC is new. To achieve the goal of this work, a solution to the problem arisen is necessary. A separate stage of this work is devoted to this, which we preface with the description of the state of the environment of the WC.

The principle of operation of the MFI and the magnetic state of its WC. Oblong FEs in the WC tend to be located along the lines of force of the MF and, therefore, in the direction of the vectors of the MFD. However, under the influence of the braking effect of the medium being processed, between the directions of the magnetic field and the elements rotating together, a certain angular displacement should be formed. This is a condition for the occurrence of the electromagnetic torque (EMT) M_{em}, which affects the FEs, on which the intensity and quality of technological processing of heterogeneous mixtures depend.

In fact, the EMT in the MFI is reactive, and the principle of operation of the MFI corresponds to the principle of operation of a synchronous motor [8]. By analogy with synchronous machines, in the WC, the longitudinal axis d is assigned in the direction of FEs orientation, and the transverse axis q is perpendicular to it. In the steady-state operating mode, the axes rotate together with these elements and the MF.

In Fig. 1, where a «snapshot» of electromagnetic quantities is shown a priori, the longitudinal axis d coincides with the y axis. The magnetic flux density vectors B are shifted in an angle from the d axis to the direction of rotation of the MF, and the MMF vector F_s «goes» in front, as the «leading» everything else.

An array of coordinately oriented FEs leads to a difference in the magnetic properties inside the WC in different directions, which is expressed by magnetic anisotropy. Along the longitudinal d and transverse q axes indicated in Fig. 1, different values of the AMP components μ_d and μ_q turn out to be. They depend on the configuration, relative position, and concentration of FEs.

Determination of the equivalent magnetic properties of the MFI working chamber. Under the described conditions, this task is very complex and not strictly determined in view of the possible «element» of the FEs distribution in the WC. Therefore, in principle, at this stage, its approximate solution seems achievable. An idealized model of filling the WC is proposed here, and an appropriate method for determining its equivalent magnetic properties, which can be used in the calculation model of the MFI as a whole, is developed.

The initial assumptions for the formation of the magnetic properties of the WC are:
- all FEs in the MFI are parallel to each other, which is natural under the influence of a homogeneous magnetic MF;

- FEs are distributed uniformly over the volume of the WC with a given displacement relative to each other;
- the magnetic properties of the medium in the cross section of the WC are anisotropic along mutually perpendicular axes: longitudinal d and transverse q;
- the discrete magnetic medium of the WC is replaced by a continuous medium with equivalent magnetic permeabilities μ_d and μ_q along the indicated axes;
- the MF in the WC is rather weak and the properties of the FEs correspond to the initial sections of their magnetization curves, therefore, the values of μ_d and μ_q in the calculation of the MF in MFI practically do not change.

In the described situation, the problem of determining the AMP components μ_d and μ_q for a given size and relative position of the FEs is solved on the basis of numerical calculations of the MF in the idealized model of filling the WC shown in Fig. 2.
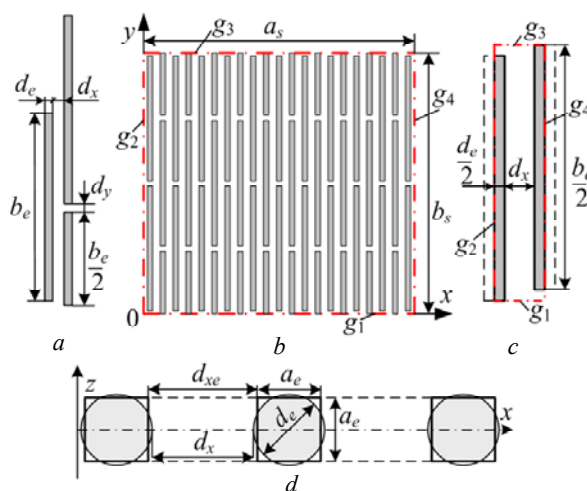
Fig. 2. Calculation model of the working chamber

In Fig. 2,*a* the basic triple of the FEs is shown with the designation of the required minimum size, which can vary. From these elements, the filling of the entire calculation model is constructed, as, for example, in Fig. 2,*b*. In the common space of the WC, from which the calculation model is extracted, the boundary lines g_1, g_2, g_3 and g_4 should be considered as lines of symmetry or periodicity. In principle, the calculation model shown in Fig. 2,*c*, can be minimal, but it is not as clear as in Fig. 2,*b*.

The key to forming the filling of the working chamber are the diameter d_e and the height b_e of the FE, as well as the gaps d_x и d_y between them. At the upper and lower borders there are halves of complete elements.

To fully reproduce the calculation model (Fig. 2,*b*), it is enough to set also the number of elements n_y by its height. In Fig. 2,*b*, for clarity, the option is given for $n_y = 2$, but the correct results will be obtained also for a different value of n_y – the main thing is that the stated symmetry conditions are observed. The remaining parameters of the WC, including the number of elements m_x along the width of the WC, were found with the condition that $a_s \approx b_s$.

To ensure the operation of the FEMM code, a Lua script has been compiled that automatically calculates the

parameters of the WC, builds its geometric model and organizes further calculations, as presented, for example, in [7] and a number of other works of the authors of this paper.

In cross section of the calculation model (Fig. 2,b) the MF is described by equation (2) and is calculated as plane-parallel. This means that, along the axial coordinate, the structure of the model should not change, which is not the case with round FE sections in the xz plane (Fig. 2d). To get around this, round sections are replaced by square ones with side a_e determined from the condition of preserving the cross-sectional area, namely: $a_e = 0{,}5\sqrt{\pi}\,d_e$. Accordingly, the equivalent gap between the elements along the width of the chamber $d_{xe} = d_x + d_e - a_e$ is recalculated.

For the calculation model, the total cross-sectional area $S_s = a_s b_s$ is calculated, as well as its part occupied by the ferromagnetic elements $S_e = n_y\, m_x\, a_e\, b_e$. Then the filling factor of the working chamber according to the cross-sectional area is: $K_{Fes} = S_e/S_s$.

It is assumed that along the axial z axis (Fig. 2,d), FEs are distributed with the same density as in the cross section. Then the same filling factor K_{Fes} will be valid on this axis, which will be taken into account when calculating the MF in 2D formulation.

The total filling of the volume of the WC FE is characterized the volumetric filling factor $K_{Fev} = K_{Fes}^2$.

The components of the magnetic permeability along the two axes of the WC are determined by calculating the magnetic fields oriented along them. Such MFs are formed by setting the corresponding boundary conditions at the boundaries of the calculation model of the WC (Fig. 2,b) for the MVP A_z.

The boundary conditions for the formation of a longitudinal MF are:

$$A_z\big|_{g2} = 0 ; \quad A_z\big|_{g4} = B_{av}a_s ; \quad \frac{\partial A_z}{\partial y}\Big|_{g1} = 0 ; \quad \frac{\partial A_z}{\partial y}\Big|_{g3} = 0 . \quad (3)$$

For the formation of a transverse MF, the boundary conditions are interchanged, namely:

$$A_z\big|_{g1} = 0 ; \quad A_z\big|_{g3} = B_{av}b_s ; \quad \frac{\partial A_z}{\partial x}\Big|_{g2} = 0 ; \quad \frac{\partial A_z}{\partial x}\Big|_{g4} = 0 . \quad (4)$$

In (3) and (4), the MF excitation factor is the estimated mean value of MFD B_{av} in WC.

Inside the domain of the calculation model (Fig. 2,b), the MF is calculated using the FEMM code by the Finite Element Method by solving the 2D differential equation (2). In this case, the nonlinear magnetic properties of the FE elements, as well as the sparse structure of the calculation area along the axial axis, are taken into account by means of a certain filling factor K_{Fes}.

For the test case, the values are taken: $d_e = 1$ mm; $b_e = 23.8$ mm; $d_x = 1.43$ mm; $d_y = 1$ mm; $n_y = 1$. Calculations using trivial formulas give: $m_x = 9$; $a_s = 21.9$ mm; $b_s = 24.8$ mm; $a_e = 0.89$ mm; $d_{xe} = 1.54$ mm; $K_{Fes} = 0.35$; $K_{Fev} = 0.122$. It is for such a structure of the computational model, Fig. 3 shows the MF images at longitudinal (a) and transverse (b) excitation.
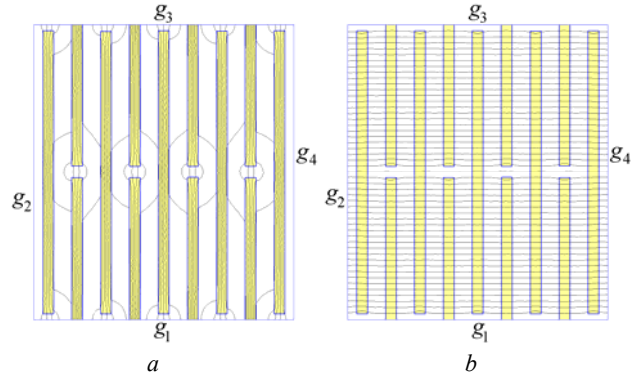

Fig. 3. Calculation model with longitudinal (a) and transverse (b) magnetic fields patterns

Using the magnetic field, the coordinate components of its strength H_x and H_y along the x and y axes are determined, and by them – the magnetic voltage drops along the vertical and horizontal lines:

$$U_{magd} = \int_0^{b_s} H_y dy ; \quad U_{magq} = \int_0^{a_s} H_x dx , \quad (5)$$

Then the average values of the components of this strength along the corresponding axes:

$$H_{yav} = U_{magd}/b_s ; \quad H_{xav} = U_{magq}/a_s \quad (6)$$

give the longitudinal and transverse components of magnetic permeability for an equivalent medium:

$$\mu_{rd} = \frac{B_{av}}{H_{yav}}\cdot\frac{1}{\mu_0} ; \quad \mu_{rq} = \frac{B_{av}}{H_{xav}}\cdot\frac{1}{\mu_0} . \quad (7)$$

Using here the magnetic constant μ_0 allows to immediately go to the relative magnetic permeability (index r has been added to identify this).

FEMM code provides obtaining U_{magd}, U_{magq}, H_{yav} and H_{xav} values using a special procedure included in the Lua script. As a result, we obtained: $U_{magd} = 1420$ A; $H_{yav} = 19090$ A/m; $\mu_{rd} = 10$; $U_{magq} = 8640$ A; $H_{xav} = 122600$ A/m; $\mu_{rq} = 1.5$.

In the general calculation area (Fig. 1), the magnetic field is described by the same equation (2) with setting in the WC of the detected magnetic anisotropy along the longitudinal and transverse axes. The propagation of the MF is limited by the outer surface of the inductor core, where the Dirichlet boundary condition is specified: $A_z = 0$.

As an example, Fig. 1 shows the vector field of the MFD obtained in the load mode for the already determined values of magnetic permeability, time, and angle $\beta = 45°$. In this case, the current value I_s was 455 A at phase voltage of the stator winding U_s equal to 220 V. At the central point of the working chamber, the MFD was 0.36 T.

Quantitative-phase relationships of electromagnetic quantities in MFI. The determination or specification of these relationships is important and necessary in the calculation of the electromagnetic parameters and characteristics of the MFI presented below.

According to the results of the calculation of the MF using FEMM code [5], we obtain EMT through the Maxwell magnetic stress tensor according to the formula [9]:

$$M_{em} = \frac{l_a}{\mu_0(r_s - r_r)} \int_{S_\delta} B_r B_\alpha r dS, \qquad (8)$$

where B_r and B_α are the radial and angular components of the MFD, respectively; r_r and r_s are the radii of the circles limiting the cross-sectional area of the gap S_δ from the sides of the WC and the stator, respectively.

The basis of the analysis of electromagnetic values of the MFI is the operation with magnetic flux linkage (MFL) of the stator phase winding. This value is calculated by the distribution of the MVP [9] through the numerical implementation of the expression:

$$\Psi = \frac{N_s l_a}{S_\varphi} \int_{S_\varphi} A_z dS \approx \frac{N_s l_a}{S_\varphi} \sum_{j=1}^{K_\varphi} A_{z,av,j} \Delta S_j, \qquad (9)$$

where S_φ, K_φ are the cross-sectional area of all finite elements with current in the phase zone of the stator winding and the number of such elements; $A_{z,av,j}$ is the average MVP value in the j-th element of the area ΔS_j.

There is a special procedure in the FEMM code that provides the determination of MFL (9), which is automated under the control of the Lua script [5, 9].

After calculating the MF with its fixed structure, the «mask» of the stator phase winding is conditionally located alternately in the stator slots in different angular positions α_k with a shift by the tooth division.

In each position of the «mask», similarly to that described in [10], the MFL is determined by the formula (9) for all slots of the phase winding and a discrete angular function of the MFL is obtained:

$$\Psi_k(\alpha_k), k=1,2,\dots,K, \qquad (10)$$

where a sufficient number of positions $K = Q_s/2$.

This periodic function is expanded into a harmonious Fourier series [8, 10], but for the purpose of this paper, the first harmonic of the MFL is enough:

$$\Psi = \Psi_m \cos(\alpha + \gamma_\psi). \qquad (11)$$

Due to the rotation of the MF with angular velocity $\Omega_s = \omega/p$ in (11) α is replaced by $\Omega_s t$, and for a stationary phase winding, the MFL becomes a temporary function:

$$\Psi = \Psi_m \cos(\omega t + \gamma_\psi). \qquad (12)$$

According to the law of electromagnetic induction, from (12) the EMF of the phase winding is obtained:

$$e = \omega \Psi_m \cos(\omega t + \gamma_\psi - \pi/2), \qquad (13)$$

where its amplitude $E_m = \omega \Psi_m$ and the initial phase $\gamma_e = \gamma_\psi - \pi/2$ are separated.

Then the effective value of the EMF of the stator phase winding:

$$E_a = \sqrt{2}\pi f_s \Psi_m. \qquad (14)$$

The set of electrical quantities taken into account in the stator phase winding is represented using the equivalent circuit shown in Fig. 4.
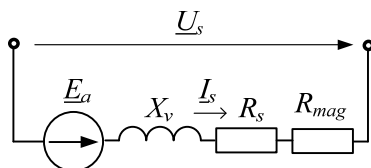

Fig. 4. Stator phase winding electrical equivalent circuit

In addition to the phase voltage U_s and current I_s, in Fig. 4 the ideal source of the already determined EMF E_a is located, as well as the ideal inductive and resistive elements characterized by the corresponding resistances: the active resistances R_s and R_{mag} represent electric and magnetic power losses, the reactance X_v – the frontal scattering of the stator winding MF. Other scattering fluxes are already taken into account in the MFL Ψ (9), determined over the entire MF in the rectilinear part of the stator winding.

The resistances R_s and X_v are calculated according to the classical methods for calculating TAM [6].

To take into account the power of magnetic losses P_{mag} in the circuit in Fig. 4, this active resistance introduced:

$$R_{mag} = \frac{P_{mag}}{m_s I_s^2}, \qquad (15)$$

and this power is determined in the stator core according to the updated method [11] after calculating the MF.

For the equivalent circuit (Fig. 4), the equilibrium voltage equation in a symbolic form is the following:

$$\underline{U}_s = -\underline{E}_a - \underline{E}_v + \underline{U}_R, \qquad (16)$$

where the EMF from the magnetic flux of frontal scattering and the voltage drop across the active resistances are presented

$$\underline{E}_v = -jX_v \underline{I}_s; \quad \underline{U}_R = (R_s + R_{mag})\underline{I}_s. \qquad (17)$$

Quantitative and phase relationships of the already mentioned and also a number of electromagnetic quantities will be provided using the vector diagram (VD) in Fig. 5,a. It is built on the identified relationships of electromagnetic quantities in the MFI in compliance with generally accepted rules of electrical engineering.
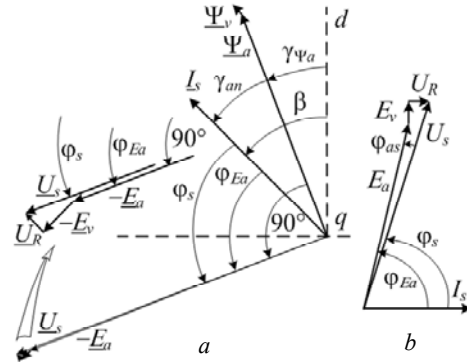
Fig. 5. Vector diagram of electrical and magnetic quantities of the stator phase winding

The angular coordinates are counted from the longitudinal axis of the WC d, which, as in Fig. 1, held vertically. Relative to it, the current vector $\underline{I}_s$ is drawn at the given angle β, and the MFL vector $\underline{\Psi}_a$ which is in (12) is drawn at the angle of the initial phase $\gamma_{\psi a}$. The MFL vector of the frontal part of the winding $\underline{\Psi}_v$ is parallel to the vector $\underline{I}_s$. The EMF vector $\underline{E}_a$, according (13), is phase-ahead from $\underline{\Psi}_a$ by 90°, therefore the vector $-\underline{E}_a$ included in (16) is ahead of $\underline{\Psi}_a$ by 90°. According to (16), the $-\underline{E}_v$ vector is perpendicular, and the vector $\underline{U}_R$ is parallel to the current vector $\underline{I}_s$. The voltage vector $\underline{U}_s$ is constructed based on the summation of vectors according

to (16). With respect to the current vector $\underline{I}_s$, the vectors $-\underline{E}_a$ and $\underline{U}_s$ received leading phase shifts φ_s and φ_{Ea}, respectively.

The EMF value E_a is found from (14), and the mentioned angle is found by the VD

$$\varphi_{Ea} = 90° - \gamma_{an} = 90° - \beta + \gamma_{\psi a}. \quad (18)$$

Then we can find $\underline{U}_s$ and φ_s. For clarity of this, a simplified (rotated and without scale) fragment of the VD is used (Fig. 5,*b*).

Active and reactive components of EMF E_a:

$$E_{a,a} = E_a\cos\varphi_{Ea} \; ; \quad E_{a,r} = E_a\sin\varphi_{Ea} . \quad (19)$$

Similar voltage U_s components:

$$U_{s,a} = E_{a,a} - U_R \; ; \quad U_{s,r} = E_{a,r} - E_\nu \quad (20)$$

give the actual value of the phase voltage and its phase shift relative to the current:

$$U_s = \sqrt{U_{s,a}^2 + U_{s,r}^2} \; ; \quad \varphi_s = \text{arctg}(U_{s,r}/U_{s,a}) . \quad (21)$$

As an example, we present the results of a test calculation carried out in relation to Fig. 1: $P_{mag} = 1906$ W; $R_{mag} = 0.00304$ Ω; $\Psi_a = 0.938$ Wb; $\gamma_{\Psi a} = 21.09°$; $E_a = 208$ V; $\varphi_{Ea} = 66.09°$; $\varphi_s = 65.77°$; $E_\nu = 10.1$ V; $U_R = 6.8$ V; $M_{em} = 324$ N·m. Separately, the values $R_s = 0.00968$ Ω and $X_\nu = 0.022$ Ω are determined.

It is from such data the picture of the distribution of MFD is a priori shown in Fig. 1and VD is built in Fig. 5,*a*. Additionally, Fig. 6 shows a picture of the magnetic force lines of the MF and the mutual correspondence of the mentioned rotation angles of different quantities for the considered MFI load mode.
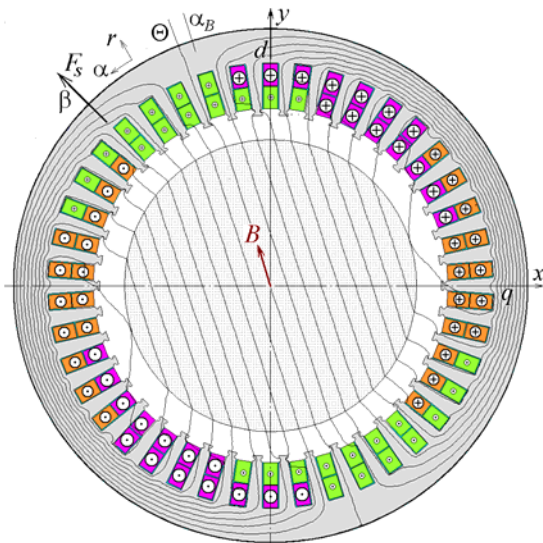

Fig. 6. MF picture in the form of force lines and angle marks for different quantities

It is noteworthy that the angle $\gamma_{\Psi a}$ turned out to be substantially smaller than β. At the same time, it was revealed that, given $\beta = 0$, the value $\gamma_{\Psi a}$ also turned out to be zero, and this corresponded to the II mode, since the EMT by (8) was zero. The rotation of the MFL vector $\underline{\Psi}_a$ from the II mode to the load mode, according to the theory of synchronous machines [8], is the load angle. Therefore, the angle $\gamma_{\Psi a}$ in Fig. 5,*a* is nothing other than the MFI load angle, i.e. $\Theta = \gamma_{\Psi a}$, which is also shown in Fig. 6.

The angle of rotation of the vector $\vec{B}$ is determined by the coordinate components of the MFD vector in the center of the WC:

$$\alpha_B = \text{arctg}(B_x / B_y) , \quad (22)$$

which is 15.1°.

Energy parameters of MFI. After calculating the MF and determining the quantitative and phase relationships of electromagnetic quantities, it is enough to quite simple calculate the energy parameters of the MFI.

Electromagnetic power in electrical terms:

$$P_{em} = m_s E_a I_s \cos\varphi_{Ea} . \quad (23)$$

On the other hand, electromagnetic power in mechanical terms can be considered as output or useful power:

$$P_{em} = P_{out} = M_{em}\Omega_s \quad (24)$$

Input or expended power:

$$P_s = m_s U_s I_s \cos\varphi_s , \quad (25)$$

where the power factor $\cos\varphi_s$ is determined by the phase shift of the voltage and current of the stator winding calculated in accordance with (21).

Power losses are composed of the power of electrical losses in the stator winding.

$$P_{el} = m_s R_s I_s^2 , \quad (26)$$

and the aforementioned magnetic losses power P_{mag} in the stator core.

Efficiency of the MFI:

$$\eta = P_{out} / P_{in}. \quad (27)$$

Characteristics of MFI. The presented theoretical base allows to calculate a number of characteristics of the MFI, connecting its electromagnetic and energy parameters, as well as the phase relationships of the corresponding quantities in the mode of a changing load. When studying characteristics, the basic ones are traditionally selected from the set of figures, while the rest are analyzed.

In MFI, the basic ones include voltage U_s and current I_s of the stator winding, which are input values for it. In this case, two variants of operation with a change in load are possible:

1) the effective current value I_s is kept constant, and the voltage and other values are calculated;

2) the effective value of the voltage U_s is kept constant, and the current and other values are calculated.

In the first case, the effective operation of the MFI at the maximum permissible level for electric losses of the stator winding power and its heating is possible, but an appropriate voltage regulator is required. In the second case, we can use the existing power supply network to power, but the stator winding and the MFI can operate in a given load range with insufficient use.

In this paper, we consider the first variant of the operation of the MFI – with the stabilization of the current value of the stator winding, leaving the second option to continue research in the following works.

At a stable value of the stator winding current, a change in the mechanical load with a change in the filling of the WC leads to a change in the EMT due to a change in the load angle and other phase relationships. Of these, for calculating the characteristics, as a variable quantity –

argument it is convenient to take the angle of the generalized initial phase of the stator winding currents β included in (1).

Then the solution of the problem of calculating the characteristics becomes quite simple: when setting the effective value of the current I_s and angle β, the MF is calculated and, according to the method expressed by formulas (1)-(27), a whole series of necessary values is obtained.

To obtain various characteristics from the calculated numerical arrays of different quantities, some of them can later be taken as an independent argument and from others – functions that are of interest to the calculator can be assigned.

In a specific calculation example of characteristics, the base value of the current $I_s = 455$ A is accepted, which was already used in the test calculation at $\beta = 45°$ and $U_s = 220$ V.

To obtain the full characteristics, the angle β range from 0 to 90° is adopted, which for sufficient «smoothness» of the graphs is carried out with a step of 5°.

The main part of the obtained characteristics is presented in Fig. 7-10. Their essence is manifested by the quantities indicated on the graphs.

We draw attention to the fact (Fig. 8) that the angles β and Θ coincide in values at the extreme points – 0 and 90°. In this case, the EMT is zero, that is, the II mode takes place. The maximum EMT value corresponds to the angle $\beta = 46°$ (Fig. 7), and here the critical load angle Θ_{cr} is 22.5° (Fig. 8).

According to the theory of synchronous machines, in the range of the angle Θ from 0 to Θ_{cr}, the operating mode of the MFI is stable. In order to have a twofold EMT margin, the load angle Θ_{nom} equal to about 7° can be considered nominal, which corresponds to the angle $\beta = 17–18°$.

Figure 7 shows that from II to this angle, the voltage, MFL, EMF and resistance R_{mag} are approximately stable – with a slight decrease with increasing load of the MFI. The same can be said about magnetic losses (Fig. 9), and electric losses are unchanged by definition, due to the stability of the current.

The electromagnetic power in electrical (23) and mechanical (24) expressions is numerically identical (Fig. 9), which can be considered as a check of the correctness of the obtained phase relationships of electrical quantities. The shape of the graphs of these powers is naturally similar to the EMT graph.

The characteristics of the power factor and efficiency (Fig. 10) show their natural growth with increasing load of the MFI. The level of efficiency in the range of stable operation corresponds to the classic electric machines of low and medium power. But the level of the power factor turns out to be very small, which is explained by the presence of large nonmagnetic gaps and a low-magnetic medium in the WC.
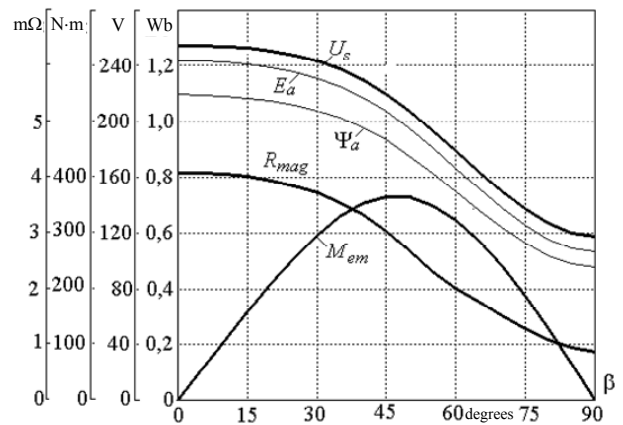
Fig. 7. Characteristics of voltage, MFL, EMF, EMT and active resistance to take into account magnetic losses
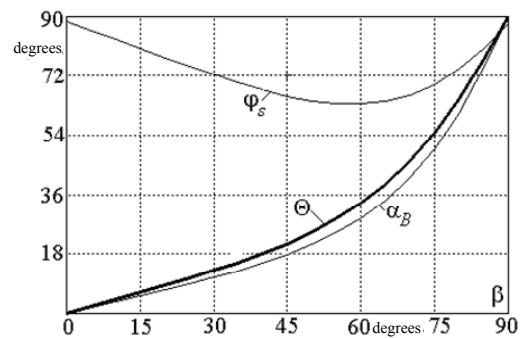
Fig. 8. Characteristics of phase relationships in MFI
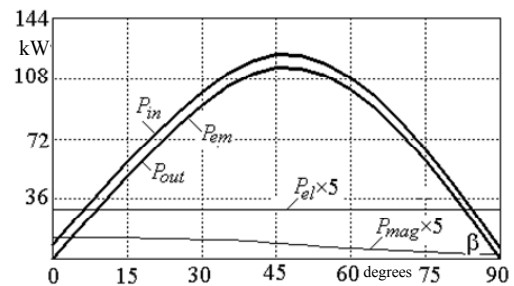
Fig. 9. Characteristics of powers and power losses
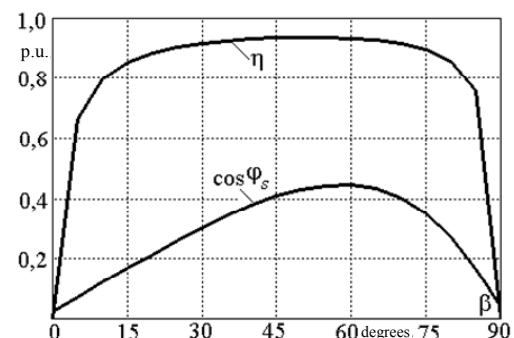
Fig. 10. Characteristics of power factor and efficiency

Conclusions.

1. Numerical-field calculation allows to accurately take into account the geometric shapes of the stator core of the MFI, its nonlinear magnetic properties and the anisotropy of the magnetic properties of the working chamber with oblong ferromagnetic elements.

2. The considered phase relationships of electromagnetic and force quantities show that, according

to the principle of operation, in the composition of the device for processing various substances, the MFI is closest to a synchronous motor.

3. One of the key elements of the developed theory and methodology for calculating electromagnetic parameters, their phase relationships and MFI characteristics is the proposed method for taking into account the magnetic anisotropy of its working chamber with filling with ferromagnetic elements.

4. In the area of stable operation, in energy terms the MFI is characterized by a rather high efficiency and a very low value of power factor. The latter is due to the presence of large gaps and a law-magnetic medium in the working chamber in the inductor's magnetic system.

5. The developed methodology for numerical-field calculations of characteristics gives a lot of useful information that can be used to design and improve MFI.

REFERENCES

1. Logvinenko D.D., Sheljakov O.P. *Intensifikacija tehnologicheskih processov v apparatah s vihrevym sloem* [Intensification of technological processes in apparatus with a vortex layer]. Kiev, Tehnika Publ, 1976. 144 p. (Rus.)

2. Zagirnyak M.V., Branspiz Yu.A., Shvedchikova I.A. *Magnitnye separatory. Problemy proektirovanija.* [Magnetic separators. Design issues]. Kiev, Tehnika Publ, 2011. 224 p. (Rus.)

3. *Kompanija GlobeCore. Apparat Vihrevogo Sloja AVS-100.* [Company GlobeCore. Vortex Layer Machine ABC-100]. Available at: https://avs.globecore.ru/products/avs-100.html (accessed 30.09.2017).

4. Milykh V.I., Shilkova L.V. Revuzhenko S.A. Numerical analysis of the magnetic field of a cylindrical three-phase magnetic separator inductor. *Bulletin of NTU «KhPI». Series: «Electric machines and electromechanical energy conversion»*, 2017, no.1(1123), pp. 76-82. (Ukr.)

5. *Finite Element Method Magnetics: OldVersions.* FEMM 4.2 11Oct2010 Self-Installing Executable. Available at: http://www.femm.info/wiki/OldVersions (accessed 15.06.2017).

6. Kopylov I.P., Goryainov F.A., Klokov B.K. *Proektirovanie elektricheskih mashin* [The design of electrical machines]. Moscow, Yurait Publ., 2011. 767 p. (Rus)

7. Milykh V.I. The system of automated formation of electrical machines computational models for the FEMM software environment. *Technical Electrodynamics*, 2018, no.4, pp. 74-78. (Ukr.) **doi: 10.15407/techned2018.04.074.**

8. Voldek A.I., Popov V.V. *Elektricheskie mashiny. Mashiny peremennogo toka* [Electrical machines. AC machines]. SPb, Piter Publ., 2010. 356 p. (Rus).

9. Milykh V.I., Polyakova N.V. Determination of electromagnetic parameters of electric machines based on numerical calculations of magnetic field. *Electrical engineering & electromechanics*, 2006, no.2, pp. 40-46. (Rus).

10. Milykh V.I. Numerically-field analysis of the adequacy of the design data of three-phase induction motors and the method of their refinement on this basis. *Technical Electrodynamics*, 2018, no.1, pp. 47-55. (Rus) **doi: 10.15407/techned2018.01.047.**

11. Milykh V.I., Shilkova L.V. The numeral-field analysis of power of magnetic losses is in the three-phase inductor of magnetic-field. *Bulletin of NTU «KhPI». Series: «Electric machines and electromechanical energy conversion»*, 2019, no.4(1329), pp. 99-106. (Ukr.) **doi: 10.20998/2409-9295.2019.4.15.**

V.I. Milykh[1]*, Doctor of Technical Science, Professor,*
L.V. Shilkova[1]*, Postgraduate Student,*
[1] National Technical University «Kharkiv Polytechnic Institute», 2, Kyrpychova Str., Kharkiv, 61002, Ukraine,
phone +380 057 7076514,
e-mail: mvikemkpi@gmail.com, larisa_lv@ukr.net

M.I. Baranov, S.G. Buriakovskyi, A.S. Hrytsenko, V.A. Kostiuk

RESULTS OF INVESTIGATIONS OF THERMAL RESISTIBILITY OF PROTOTYPES OF ALUMINUM ALLOY PANELS OF FUEL TANK OF AIRPLANE TO DIRECT ACTION OF NORMALIZED COMPONENTS OF ARTIFICIAL LIGHTNING CURRENT

Purpose. Implementation of calculation-experimental determination of thermal resistibility of walls of aluminum alloy panels of different thickness of fuel tank of the airplane designed in Ukraine to direct action on them of normalized components of current of artificial lightning. Methodology. Theoretical bases of thermophysics, bases of theoretical electrophysics, bases of measuring technique, electrophysics bases of technique of high-voltage and large pulsed currents. Results. The results of calculation-experimental investigations of thermal resistibility of prototypes with the necessary sheeting flat rectangular panels of fuel tank of the designed airplane are resulted measuring 550 mm x 800 mm and from 1.2 to 4 mm thick of aluminum alloy B95 is easily soiled to direct action on them in obedience to the operating requirements of normative documents of the USA SAE ARP 5412 and SAE ARP 5416 of A-, B- and C*- component of current of artificial lightning (1A area), and also D-, B- and C*- components of current of artificial lightning (2A area) with the normalized amplitude-temporal parameters (ATPs). It is determined that the tested panels of fuel tank of airplane in 1.2 mm, 1.5 mm and 1.8 mm thick for an area of 1A and 1.2 mm and 1,5 mm thick for an area of 2A are thermally unstable to the direct shots in them of plasma channel of a storm discharge imitated in laboratory terms with the indicated components of current of artificial lightning. It is shown that thermal resistibility to lightning of the tested panels of fuel tank of airplane is determined of ATP shortened protracted C*- components of current of artificial lightning, causing appearance in them of the rounded small holes of melting the radius of r_k and depth of h_k. For finding by a calculation by the sizes of r_k and h_k in the indicated panels of fuel tank of airplane, struck in an air atmosphere a direct blow in them the imitated storm discharge, the proper close correlations are recommended. The capacity of these calculation correlations is confirmed results executed by the powerful high-voltage generator of impulsive current of artificial lightning of type of UITOM-1 of model experiments created in Ukraine. Originality. The calculation and experimental estimations of thermal resistibility of flat duralumin panels of fuel tank of the airplane designed in Ukraine are first executed to the direct action on them for the areas of 1A and of 2A of plasma channel of the imitated storm discharge with the normalized indicated documents of ATP flows on it (to the channel) A (D)-, B- and C*- components of current of artificial lightning. Practical value. Taking into account the executed calculation-experimental investigations a practical conclusion is done that for prevention in the case of direct blow in the being in an air atmosphere airplane of plasma channel of lightning with normalized ATPs indicated components of its pulsed current of self-ignition of fuel steams in the examined duralumin tank of the designed airplane and its catastrophe the thickness of wall of an aluminum alloy B95 of this tank with the proper sheeting must make no less than 1.8 mm for the area of 2A and no less than 2 mm for the area of 1A. References 19, tables 2, figures 17.
Key words: **lightning, fuel tank of airplane, prototype of panel of fuel tank, thermal resistibility to lightning, components of current of lightning, generator of current of artificial lightning, calculation, experiment**.

Наведено результати досліджень термічної стійкості виготовлених в заводських умовах з необхідними покриттями випробувальних зразків (ВЗ) розміром 550 мм × 800 мм і товщиною від 1,2 до 4 мм плоских панелей з високоміцного алюмінієвого сплаву марки В95 паливного бака розробляємого вітчизняного літака до прямої дії на них для зон 1А та 2А нормованих за вимогами нормативних документів США SAE ARP 5412 і SAE ARP 5416 A (D)-, В- і C*- компонент струму штучної блискавки. Показано, що вказані ВЗ панелей паливного бака літака товщиною 1,2 мм, 1,5 мм і 1,8 мм для зони 1А та товщиною 1,2 мм і 1,5 мм для зони 2А не задовольняють вимогам термічної стійкості до прямої дії на них використовуваних компонент струму штучної блискавки з нормованими амплітудно-часовими параметрами (АЧП). Розрахунково-експериментальним шляхом із застосуванням капілярного контролю встановлено, що для зон 1А та 2А пряма дія відповідних компонент струму штучної блискавки з нормованими АЧП на ВЗ панелей паливного бака літака вказаною товщиною призводить до їх наскрізного проплавлення, здатного викликати вибух паливної пари в баці літака, що розглядається, і його катастрофу. Бібл. 19, табл. 2, рис. 17.
Ключові слова: **блискавка, паливний бак літака, зразок панелі паливного бака, термічна блискавкостійкість, компоненти струму блискавки, генератор струму штучної блискавки, розрахунок, експеримент.**

Приведены результаты исследований термической стойкости изготовленных в заводских условиях с необходимыми защитными покрытиями испытательных образцов (ИО) размером 550 мм × 800 мм и толщиной от 1,2 до 4 мм плоских панелей из высокопрочного алюминиевого сплава марки В95 топливного бака разрабатываемого отечественного самолета к прямому воздействию на них для зон 1А и 2А нормированных по требованиям нормативных документов США SAE ARP 5412 и SAE ARP 5416 A (D)-, В- и С*- компонент тока искусственной молнии. Показано, что указанные ИО панелей топливного бака самолета толщиной 1,2 мм, 1,5 мм и 1,8 мм для зоны 1А и толщиной 1,2 мм и 1,5 мм для зоны 2А не удовлетворяют требованиям термической стойкости к прямому действию на них используемых компонент тока искусственной молнии с нормированными амплитудно-временными параметрами (АВП). Расчетно-экспериментальным путем с применением капиллярного контроля установлено, что для зон 1А и 2А прямое действие соответствующих компонент тока искусственной молнии с нормированными АВП на ИО панелей топливного бака самолета указанной толщины приводит к их сквозному проплавлению, способному вызвать взрыв топливных паров в рассматриваемом баке самолета и его катастрофу. Библ. 19, табл. 2, рис. 17.
Ключевые слова: **молния, топливный бак самолета, образец панели топливного бака, термическая молниестойкость, компоненты тока молнии, генератор тока искусственной молнии, расчет, эксперимент.**

Introduction. At direct strokes to aircrafts of linear lightning developing in the atmosphere of our planet with average frequency of up to 100 discharges per second across the globe [1], the amplitude-temporal parameters (ATPs) of the flowing pulsed current as directly in the

plasma channel of its discharge and external structural elements of the aircraft, and in the electrical circuits of the on-board radio and electrical engineering, as well as electronic equipment aircraft can take hazardous levels for electrodynamic and thermal resistibility of main devices and systems of aircraft [2]. According to the requirements of the applicable US regulatory documents SAE ARP 5412 [3] and SAE ARP 5416 [4], relating to direct lightning strikes to aerospace equipment during flight, the pulsed lightning current of the atmospheric discharge contains the following three main components: pulsed $A-$, intermediate $B-$ and long-term $C-$ components. In this case, the normalized ATPs of the pulsed $A-$ lightning current components according to [3, 4] take the following numerical values: current amplitude $I_{mA}=\pm200$ kA (with tolerance of ±10 %); current action integral $J_A=2\cdot10^6$ A^2·s (with tolerance ±20 %); time t_{mA} corresponding to the current amplitude I_{mA} is $t_{mA}\leq50$ µs; duration τ_{pA} of the current flow must be equal to $\tau_{pA}\leq500$ µs. The aperiodic intermediate $B-$ component of the simulated lightning current has the following ATPs [3, 4]: average current $I_{LB}=\pm2$ kA (with tolerance ±20 %); transferred electric charge $q_B=\pm10$ C (with tolerance ±10 %); the duration τ_{pB} of the current flow is $\tau_{pB}=5$ ms (with tolerance ±10 %). In the case under consideration, the normalized ATPs of the aperiodic long-term $C-$ lightning current component should have the following numerical values [3, 4]: current amplitude $I_{mC}=\pm(200\text{-}800)$ A; transferred electric charge $q_C=\pm200$ C (with tolerance ±20 %); duration τ_{pC} of the current flow is $\tau_{pC}=(0.25\text{-}1)$ s. In addition, the modified (shortened) long-term C^*- lightning current component is characterized by the following ATPs [3, 4]: average current of at least $I_{LC*}=\pm400$ A; duration τ_{pC*} of the current flow is $\tau_{pC*}=(15\text{-}45)$ ms. We point out that when simulating in laboratory conditions the total current of linear lightning and full-scale tests for lightning resistibility of an aircraft, instead of the $A-$ component, the $D-$ component can be used with the following ATPs [3, 4]: current amplitude $I_{mD}=\pm100$ kA (with tolerance ±10 %); current action integral $J_D=0.25\cdot10^6$ A^2·s (with tolerance o±20 %); time t_{mD} corresponding to the current amplitude I_{mD} is $t_{mD}\leq25$ µs; duration τ_{pD} of the current flow must be equal to $\tau_{pD}\leq500$ µs.

Currently, in Ukraine and Eastern Europe countries, only the Scientific-&-Research Planning-&-Design Institute «Molniya» of the National Technical University «Kharkiv Polytechnic Institute» has a powerful high-voltage high-current lightning current generator (LCG) that provides reproduction of all the above components of linear lightning current with ATPs normalized by [3, 4] on tested for lightning resistibility objects of aviation and rocket and space technology [5-7]. This LCG of type UITOM-1 was developed and created in 2007 by the employees of the Scientific-&-Research Planning-&-Design Institute «Molniya» of the National Technical University «Kharkiv Polytechnic Institute» [5]. Stationary LCG of type UITOM-1 with nominal energy consumption of up to 1.2 MJ (at a cost of at least USD 1.2 million [8]), which contains 5 separate high-voltage pulsed current generators (PCGs) simultaneously operating on a common electrical load for electrical voltage of ±5 kV to

±50 kV [5], is located on a high-voltage test site with area of 21 hectares of the specified Institute, geographically located in a picturesque forest 75 km south of Kharkiv near the urban village Andreevka.

The tasks of ensuring the electrodynamic and thermal resistibility of various aircrafts (airplanes, rocket carriers, etc.) to direct effects in the earth air atmosphere on their metal (composite) structures, airborne devices and systems of powerful lightning discharges are relevant in all industrialized countries of the world and are of great practical interest.

The goal of the paper is the calculation-experimental determination of the thermal resistibility of the walls of duralumin panels of various thicknesses of the fuel tank of the aircraft designed in Ukraine to the direct effect of normalized components of the artificial lightning current on them.

1. Problem definition. We proceed from the fact that on the tested for lightning resistibility in the discharge circuit of the indicated high-voltage high-current LCG of the UITOM-1 type [5] a prototype of a flat panel made of high-strength aluminum alloy grade B95 (plan size 550 mm × 800 mm and wall thickness h: 1.2 mm; 1.5 mm; 1.8 mm; 2 mm; 2.5 mm; 3 mm; 3.5 mm; 4 mm) of the fuel tank of the domestic aircraft under development with the double-sided protective coatings required by the technological requirements, a high-current plasma channel of a lightning discharge simulated under laboratory conditions for zones 1A (A-, B- and C^*-lightning current components [3, 4]) and 2A (D-, B- and C^*- lightning current components [3, 4]), for which the used components of the artificial lightning current satisfy the ATPs normalized according by [3, 4] act. We believe that the thermal resistibility of the test sample (TS) of the aircraft's fuel tank panel is determined by the depth h_k of the hole (crater) of the penetration of the TS wall in the binding zone on its outer flat surface of the plasma channel of a thunderstorm discharge simulated in atmospheric air having a cylindrical shape [9]. Then the condition of thermal resistibility of the studied duralumin panels of the aircraft fuel tank to direct action on them of lightning reproduced at a high-voltage laboratory can be written in the following integral form:

$$h_k < h. \tag{1}$$

We believe that during the direct action of the plasma channel of a lightning discharge on the prototype of the aircraft's fuel tank panel, the rounded binding zone of radius r_k remains almost stationary relative to the outer flat surface of the TS. We assume that the volume V_k of TS wall's metal (alloy) molten by current of artificial lightning determines the volume and nature of the zone of its thermal damage from the action of the channel binding of this lightning discharge at the indicated location. We perform a calculated assessment of the results of the thermal effect of a simulated lightning strike to the aircraft fuel tank panel TS assuming that during this transient (no more than 50 ms) shock, the thermophysical characteristics of the material of the aircraft fuel tank panel under study are unchanged. Let the temperature T_0 of the investigated TS of the panels of the fuel tank of the aircraft of the air environment be room temperature and equal to 20 °C [10].

We carry out experimental photo-registration of a thermal spark penetrating through the TS wall of an airplane's fuel tank panel when it is fused by a plasma channel of lightning simulated by UITOM-1 type LCG using the original technology developed by us, based on the use of an insulating light-tight camera (LTC) in the form of the correct pyramids with a height of about 1 m (Fig. 1). Here, in the area of the rectangular base of the pyramidal LTC, the TS is rigidly fixed using an integral rubber gasket (see Fig. 1), and in the area of its apex, a Zenit-12XP camera with a Kodak color film having a photosensitivity of at least 200 units ISO is fixed. Preliminary experimental studies have shown that in order to ignite fuel vapors in an aircraft tank, a thermal spark should emit in them (vapors) by pulsed way an energy approximately equal to at least 200 μJ.
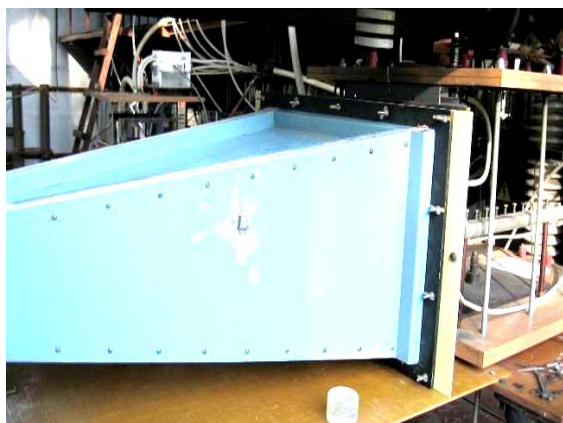

Fig. 1. General view of the insulating pyramidal LTC with vertically mounted on its end a flat panel TS of 550×800 mm in plan and thickness of $h = 3$ mm of the aircraft's fuel tank, galvanically connected to the high-current discharge circuit of the UITOM-1 high-voltage test setup, before direct exposure to it of plasma channel discharge with a pulsed current of artificial lightning with normalized ATPs

We point out that in addition to deciphering the photo-registration data in LTC of possible sparks during thermal burn-through of the walls of the test samples by the lightning channel, their lightning resistibility after laboratory tests will, if necessary, be determined by conducting a separate capillary laboratory control in order to detect penetration of a defectoscopic penetrant at the test pulses supply points to these samples [4].

We assume that if condition (1) is met, the geometric configuration of the penetration hole of the metal on the wall of the aircraft's fuel tank panel has the shape of a round cone with a height h_k with a base radius r_k on the outer surface of the panel and a vertex directed inward to the wall, and if condition (1) is not fulfilled and a small through penetration (burn-through) of the wall ($h_k \geq h$) of the panel under consideration from the thermal action of lightning on it, it takes the shape of a truncated round cone with a zone of its truncation on its inner surface [11]. At significant through penetration (burn-through) of the wall ($h_k \gg h$) of the aircraft's fuel tank panel, the geometric configuration of its penetration hole transforms into the shape of a round cylinder [11].

We use the statement, confirmed by our own numerous experimental data, that the volume V_k, of the

material of the aircraft's fuel tank panel TS molten from the direct action of the thunderstorm discharge channel the aircraft's fuel tank panel which is dangerous for local through penetration of the studied tank wall of the aircraft is determined by the long-term C- or shortened long-term C^*- components of the normalized artificial lightning current [7, 11]. Note that from the standpoint of thermal action on structural elements of the aircraft A (D)- and B- components of the normalized artificial lightning current cause only surface melting of the metal wall of its sheathing, which is not dangerous for the survivability of an aircraft during a thunderstorm [7, 11].

To initiate electric breakdown of an air gap of up to 50 mm in length in a two-electrode system (TES) «high-voltage electrode-TS» and the formation of an artificial lightning plasma channel in the air above the TS, we use an electrically exploding wire (EEW) [3, 4]. As an EEW, we use a thin copper wire with a diameter of 0.1 mm and a length of up to 50 mm. Between the flat surface of the TS and the edge of the EEW, we ensure that the air gap in the TES is no more than 2 mm long.

First, it is required to carry out, according to (1), an approximate calculation estimation of the thermal resistibility of the prototype of the indicated panel of the aircraft's fuel tank to the direct action of the simulated lightning channel on it (prototype), and then, using the UITOM-1 type LCG [5], to carry out the experimental verification of thermal lightning resistibility of the TS of the panel under consideration to direct impact of the plasma channel of artificial lightning into it.

2. Calculation estimation of the thermal resistibility of samples of aircraft's fuel tank panels to artificial lightning current. In the calculation estimation of the volume V_k of the wall material molten by a cylindrical plasma channel with an artificial lightning current in the TS of the duralumin panel of the aircraft's fuel tank, we use the well-known relation, which has the following analytical form [12, 13]:

$$V_k = U_{ac} q_C d_0^{-1} [C_0 (T_m - T_0) + C_m]^{-1}, \qquad (2)$$

where U_{ac} is the near-electrode voltage drop in the TS zone, which plays the role of an anode electrode in the TES of the discharge circuit of the UITOM-1 type installation at a given negative polarity of C (C^*)- components, B- component and the first half-waves of A (D)- components of artificial lightning current, V; q_C is the amount of electricity (charge) carried by C (C^*)- components of artificial lightning current, C; d_0 is the density of the material of the panel of the aircraft's fuel tank, kg / m³; C_0 is the specific heat of the material of the panel of the aircraft's fuel tank, J/(kg·°C); C_m is the specific heat of fusion of the material of the panel of the fuel tank of the aircraft, J/kg; T_m is the melting temperature of the material of the aircraft's fuel tank panel, °C, T_0 is the temperature of the ambient air of the TS, °C.

In Table 1, in the first approximation, using the quantitative data from [7, 14, 15], the main thermophysical characteristics for the aluminum alloy of the grade B95 of the studied experimental fuel tank panels of the aircraft under development are given.

Main thermophysical characteristics of the material of the experimental duralumin fuel tank panels of the designed aircraft [7, 14, 15]

Characteristic	Dimension	Value
U_{ac}	V	8.2
d_0	kg/m³	2790
C_0	J/(kg·°C)	920
T_m	°C	638
C_m	J/kg	390·10³

Using, to the first approximation, the conical shape of the hole (crater) for penetrating the flat wall of the aircraft's fuel tank panel with a volume of $V_k = \pi r_k^2 h_k / 3$, taking into account (2) for its depth h_k in the wall under study, from the direct thermal action of the plasma channel with radius r_k of lightning discharge on it, we have:

$$h_k = 3(\pi r_k^2)^{-1} U_{ac} q_C d_0^{-1} [C_0(T_m - T_0) + C_m]^{-1}. \quad (3)$$

For the estimated calculation of the radius r_k (m) of the simulated lightning discharge channel with shortened long-term C^*- component of the lightning current in its rounded supporting zone on the outer flat surface of the studied panel of the aircraft's fuel tank, we use the following empirical dependence [7, 16]:

$$r_k = 0,11 \cdot 10^{-3} (I_{mC^*})^{1/2}, \quad (4)$$

where I_{mC^*} is the modulus of the maximum current for the shortened long-term C^*- component of the artificial lightning current in the plasma cylindrical channel of the discharge, which transfers the electric charge q_{C^*}.

Then, regarding the flow in the channel of artificial lightning of the shortened long-term C^*- current component, from (3), (4) for the depth h_k (m) of the conical penetration hole in the wall of the studied panel of the aircraft's fuel tank, we obtain in the final form the following approximate relationship:

$$h_k = 78,92 \cdot 10^6 (I_{mC^*} d_0)^{-1} U_{ac} q_{C^*} [C_0(T_m - T_0) + C_m]^{-1}. \quad (5)$$

To evaluate the working capacity at $T_0 = 20$ ° C of the obtained calculation relationship (5), which determines, at a direct lightning strike on an aircraft, the depth h_k of the penetration hole in the wall of the considered flat panel of its fuel tank, we use the numerical data given in Table 1, as well as the following initial parameters corresponding to the conditions for conducting thermal tests for lightning resistibility of the TS for zones 1A and 2A using the UITOM-1 type installation: $I_{mC^*} = 1000$ A; $q_{C^*} = 6.1$ C. After substituting the indicated initial data in (5), we find that the sought value h_k assumes a numerical value equal to approximately 1.48 mm. From this, taking into account (1) and the calculation estimation for h_k carried out according to (5), for determining the thermal resistibility of a plane panel with thickness h of the aircraft's fuel tank to a direct impact to it of a lightning discharge channel with shortened long-term C^*- component of the artificial lightning current, we can preliminary conclude that tested duralumin panels of the indicated tank with wall thickness h of 1.2 mm and 1.5 mm with high probability, and with h=1.8 mm with a possible degree of probability may not satisfy the accepted condition of their thermal resistibility to normalized pulsed lightning current action.

3. Equipment for experimental verification of thermal lightning resistibility of samples of aircraft's fuel tank panels. This verification is feasible by placing the indicated TS of duralumin panels of the fuel tank of the aircraft into the gap of the high-current discharge circuit of the LCG of type UITOM-1, general view of which is shown in Fig. 2.

Fig. 2. General view of a high-voltage high-current test facility of the type UITOM-1 (developed by the Scientific-&-Research Planning-&-Design Institute «Molniya» of the National Technical University «Kharkiv Polytechnic Institute») which simulates the direct effect of the main components of the artificial lightning current on the TS of the metal panel of a domestic aircraft's fuel tank (in the foreground is a desktop with a three-electrode controlled air switch for voltage of ±50 kV and an air exhaust system, and in the background are powerful high-voltage generators PCG-A, PCG-D, PCG-B, PCG-C and PCG-C*) [5, 6]

Figure 3 shows the electrical equivalent circuits of the discharge circuits of five powerful high-voltage generators (PCG-A, PCG-D, PCG-B, PCG-C and PCG-C*) of the UITOM-1 type test facility, modeling respectively A-, D-, B-, C- and C*- components of the artificial lightning current and synchronously operating on a common low-inductance and low-resistance concentrated $R_L L_L$ load (R_L=50 mΩ; L_L=1 μH) [5, 6]. It can be seen that in the discharge circuit of the LCG used, the active resistance R_S=0.158 mΩ of the low-resistance measuring shunt of the ShK-300M1 type, which passed the state metrological certification at the State Enterprise «Kharkiv Standard Metrology» (certificate of verification of measuring equipment No. 06/4113 of April 14, 2017) is connected in series with the indicated electrical load equivalent. Table 2 shows the main technical characteristics of the shunt type ShK-300M1 [7, 17].

Figure 4 shows general view of a measuring disk coaxial shunt of the ShK-300M1 type, and Fig. 5 presents a view of this shunt assembly with shielded coaxial communication line of the measuring path and SDN-300 voltage divider matched on to this path, the coaxial connectors 1:1 and 1:2 of which are connected to the coaxial inputs of three digital storage oscilloscopes (DSO) for recording ATPs of A (D)-, B- and C (C*)- components of the current of artificial lightning. Oscilloscopes of the Tektronix TDS 1012 type, which were metrologically

verified by the State Enterprise «Kharkiv Standard Metrology» (for example, calibration certificate No. 08/2128K of 05.16.2017) and placed in a buried measuring metal bunker remote from the UITOM-1 installation for reduce the influence of interference at a distance of 60 m [7, 17] have been used as DSO.
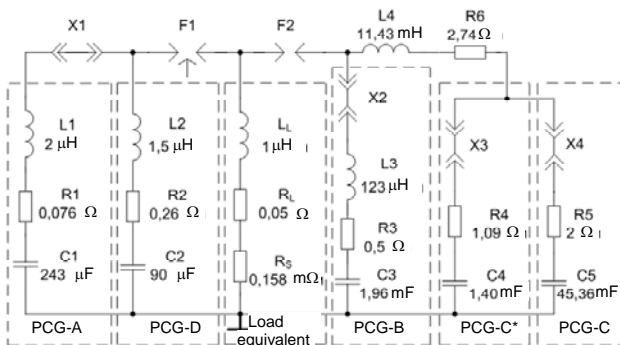

Fig. 3. Electrical equivalent circuits for the discharge circuits of five separate high-voltage PGSs (PCG-*A*, PCG-*D*, PCG-*B*, PCG-*C* and PCG-*C**) and a powerful LCG type UITOM-1 as a whole with one common electric active-inductive $R_L L_L$ load (F1, F2 - three- and two-electrode high-current air switches for voltage ±50 kV and ±5 kV, respectively; X1-X4 - electrical jumpers; R_S=0.158 mΩ - active resistance of a measuring coaxial shunt of type ShK-300M1; R1-R5, L1 -L3 - own electrical parameters of the circuits of PCG-*A*, PCG-*D*, PCG-*B*, PCG- *C** and PCG-*C*; R6, L4 - electric of forming elements for circuits of PCG-*C* and PCG-*C**) [5, 6]

Table 2

Technical characteristics of the high-voltage high-current measuring shunt ShK-300M1 [17, 18]

Shunt name	Characteristic's value		
	R_S, mΩ	K_S, A/V	Mass, kg
ShK-300M1	0.158±1 %	K_{SA}=12625	3.1
		K_{SC}=6312	

Note. K_S=2/R_S is the shunt conversion coefficient, A/V; K_{SA} is the shunt conversion coefficient when measuring in the LCG discharge circuit of ATPs of *A*- and *D*- components of artificial lightning current, A/V (from the 1:1 coaxial connector of a special voltage divider (SVD) type SDN-300); K_{SC} is the shunt conversion coefficient when measuring in the LCG discharge circuit of the ATPs of *B*- ,*C*- and *C**- components of the artificial lightning current, A/V (from the 1:2 coaxial connector of the SDN-300 voltage divider matched on)

Fig. 4. General view of a measuring disk shunt of a coaxial design of the ShK-300M1 type, installed in a high-current discharge circuit of a high-voltage test setup of the UITOM-1 type and used for simultaneous recording on the screens of three storage oscilloscopes of ATPs of *A* (*D*)-, *B*- and *C* (*C**)- components of the artificial lightning current [17, 18]

Fig. 5. General view of the measuring disk coaxial shunt of the ShK-300M1 type assembled with a shielded triaxial cable communication line (70 m long) and a matched on special voltage divider of the SDN-300 type with two coaxial connectors 1:1 and 1:2 connected by short pieces of cable to the coaxial inputs of the corresponding digital storage oscilloscopes [7, 17]

Data in Fig. 3 shows that in the discharge circuits of the PCG-*A* and PCG-*D* generators a controlled three-electrode air switch F_1 with massive steel electrodes for voltage of ±50 kV is installed, and in the discharge circuits of the PCG-*B*, PCG-*C* and PCG-*C** generators, there is a two-electrode air switch F_2 with graphite electrodes for voltage of ±5 kV [5, 19]. After a simultaneous charge from two parallel-operating from a single-phase industrial network with frequency of 50 Hz of the boost-rectifier devices of the high-voltage capacitors of the corresponding PCGs of the UITOM-1 test facility to the required by the conditions of obtaining in the TS of necessary by [3, 4] ATPs of the current pulses of artificial lightning of constant electric voltage of negative polarity (for capacitors of the PCG-*A* and PCG-*D* up to voltage U_{CA} in the range –(21-21.5) kV; for capacitors of the PCG-*B* and PCG-*C** up to voltage U_{CC} in the range –(3.1-3.8) kV) and feeding from a special generator developed by the Scientific-&-Research Planning-&-Design Institute «Molniya» of the National Technical University «Kharkiv Polytechnic Institute» of an igniting microsecond voltage pulse of negative polarity with amplitude of up to 100 kV [5, 19] to switch F_1 (see Fig. 3) there was a high-current discharge of pre-charged high-voltage capacitors of the applied PCG generators on the outer flat surface of the aircraft's fuel tank panel TS.

Figure 6 shows the test circuit of the UITOM-1 type high-voltage installation, corresponding to the case of using for the purposes of experimental verification of lightning resistibility of the TS of the fuel tank panels of the aircraft to the effects on them only of *C**- component of artificial lightning current from the PCG- *C**.

An experimental determination of the lightning resistibility of the TS of the fuel tank panels of the aircraft at the direct influence of the plasma channel of the simulated lightning discharge on them was carried out on the indicated UITOM-1 type test setup containing four indicated PCGs (see Fig. 3). Moreover, when modeling for the purpose of testing the TS of the artificial lightning current pulses for zone 1A, three parallel operating PCGs were used: PSG-*A*, PCG-*B* and PCG-*C**. During the reproduction of simulated pulsed lightning currents during the TS test for zone 2A, the following three parallel operating PCGs: PCG-*D*, PCG-*B* and PCG-*C** were used.
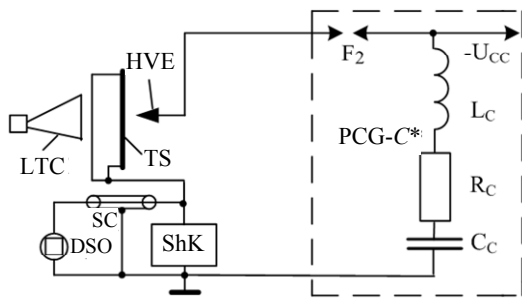
Fig. 6. A test circuit using a high-voltage high-current installation of the UITOM-1 type to determine the lightning resistibility of prototypes of flat panels of a fuel tank of a domestic aircraft at direct exposure to them of air lightning discharge from PCG, simulating only the modified (shortened) long-term C^*- component of the artificial lightning current (PCG-C^*- generator, reproducing C^*- component of lightning current; TS - test sample; HVE - high-voltage electrode, on which an electrically exploding thin copper wire is fixed; LTC - light-tight camera for photographic recording of a thermal spark; SC - shielded cable of a coaxial communication line; DSO - digital oscilloscope; ShK - disk coaxial shunt for measuring ATPs of artificial lightning current pulses having an active resistance of $R_S=(0.158\pm0.001)$ mΩ and conversion coefficients K_S equal to 12625 A/V (for measuring the A- and D- components of the lightning current) and 6312 A/V (for measuring the B- and C^*- components of the lightning current); $R_C\approx3.83$ Ω, $L_C\approx11.43$ mH, $C_C\approx1.4$ mF - electrical parameters of the PCG-C^* discharge circuit; F_2 - PCG-C^* two-electrode air switch for voltage ±5 kV with graphite electrodes, controlled in operation by applying an igniting microsecond voltage pulse with an amplitude of -100 kV to a three-electrode air switch F_1 (voltage ±50 kV) in the discharge circuit of PCG-A (PCG-D); U_{CC} - PCG-C^* charging voltage)

Estimation of the lightning resistibility of the TS of the aircraft's fuel tank panels after feeding them of required in accordance with the recommendations specified in the US documents SAE ARP 5412 [3] and SAE ARP 5416 [4] current pulses of artificial lightning was carried out by:

• external inspection of the TS of the panels of the aircraft's fuel tank in order to determine the integrity of their structure in the zone of direct impact in them of the lightning channel;

• photo-recording with the help of the LTC and a camera (Fig. 7) of possible thermal sparks from the internal flat surface of the TS during direct exposure from the above-mentioned high-voltage PCG generators of the UITOM-1 type test installation to their external surface of the corresponding current pulses of artificial lightning for zones 1A and 2A;

• carrying out, after high-voltage high-current tests of pilot duralumin panels on the LCG of the type UITOM-1, of capillary control of the TS.

4. Test results for thermal lightning resistibility of samples of aircraft's fuel tank panels for zones 1A and 2A. Figure 8 shows general view of the TS of the panel being examined for lightning resistibility ($h=3$ mm) of the aircraft's fuel tank immediately after direct exposure to it of the full normalized current of artificial lightning, characteristic of zone 1A. Experimental verification at the UITOM-1 type LCG (see Fig. 2) of the thermal lightning resistibility of the TS of flat panels 4 mm, 3.5 mm, 3 mm, 2.5 mm, 2 mm, 1.8 mm and

Fig. 7. Appearance of a pyramidal LTC with a camera at its small end (the camera is covered with a black lightproof protective cover) during the current registration of thermal sparks from the internal surface of the TS, rigidly and vertically mounted on its large end

1.5 mm thick of the aircraft's tank for zones 1A and 2A showed that through penetration of their walls was not visually observed.

Fig. 8. General view of the TS of a flat panel with a plan size of 550×800 mm (thickness $h=3$ mm) of the aircraft's fuel tank, vertically mounted on the end face of an insulating LTC and connected by flexible massive copper buses to a high-current discharge circuit of the UITOM-1 high-voltage test setup, immediately after direct exposure to it (top right) of the plasma channel of the discharge with pulsed current of artificial lightning simulating the direct thermal effect on the TS of normalized current pulses of the air lightning discharge for zone 1A

The later processing of films from the camera mounted on the end of the LTC and recording possible thermal sparks from the inner surface of the TS of the panels showed that there were no thermal points or sparking on the inside of these panels either. At direct impact on the indicated TS of the aircraft's fuel tank panels of the plasma high-current channel of artificial lightning current with normalized ATPs of its A (D)-, B- and C^*- component, there was only local fusion of the outer surface of the TS in the binding zone on it of this high-current channel of air simulated lightning discharge with the formation, firstly, of a rounded molten hole

(from the action of A (D)- lightning current component) with a diameter of up to 60 mm and a shallow depth (up to 50 microns) and, secondly, of a central rounded reflow crater (from the action of C^*- lightning current components) with a diameter of up to 7.4 mm and a depth of up to 1.5 mm.

The experimental results of the laboratory capillary inspection of the TS conducted later by the personnel of the special unit of Antonov Company revealed the penetration of a defectoscopic penetrant through duralumin panels 1.5 mm and 1.8 mm thick tested for zone 1A, and also through duralumin panels tested for zone 2A with thickness h=1.5 mm. These results indicate the presence in the TS of through defects for the indicated cases.

The above experimental results correlate well with the calculated data obtained by (4) for radius r_k≈3.6 mm (at I_{mC*}=1110 A) and according to (5) for depth h_k≈1.4 mm (at q_{C*}=6.4 C) of a rounded penetration hole of a wall of tested on the described powerful high-voltage high-current LCG type UITOM-1 the flat duralumin panel of the fuel tank of the designed aircraft.

Figures 9-11 show the oscillograms of the artificial lightning current components typical for zone 1A that act in the discharge circuit of the LCG type UITOM-1 on the IO of thickness h=1.5 mm of the flat duralumin panel of the aircraft's fuel tank. A visual examination of this TS after testing it in the LCG circuit for thermal lightning resistibility (Fig. 12) did not give direct results on the presence of through penetration in its wall from a direct impact of the simulated lightning current components A-, B- and C^*- with normalized ATPs. Only the further application of the method of capillary control of the place of thermal damage to the TS for zone 1A confirmed the presence of through penetration of the wall of the duralumin panel with thickness h=1.5 mm of the aircraft's fuel tank.

Figures 13-15 show the oscillograms of the artificial lightning current components typical for zone 2A that act in the UITOM-1 type LCG discharge circuit on the TS with thickness h=1.5 mm of a flat duralumin panel of the aircraft's fuel tank. From the data of a visual inspection of this TS, it follows that for zone 2A, the D-, B- and C^*- components of the artificial lightning used in tests of the TS of thickness h=1.5 mm of the plane duralumin panel of the aircraft's do not cause through penetration of its wall visible to the naked eye. This is also evidenced by the registration results for zone 2A with the help of a camera installed in the LTS of possible thermal sparks from the inner surface of the TS with thickness h=1.5 mm of its wall. At the same time, the possible through penetration in this case of the wall under consideration with thickness h=1.5 mm of the aircraft's fuel tank is indicated by the calculated data by (5) for the depth h_k≈1.3 mm (at q_{C*}=6.16 C) and according to (4) for radius r_k≈3.7 mm (at I_{mC*}=1148 A) of the rounded hole of its penetration due to the action of the lightning channel on it.
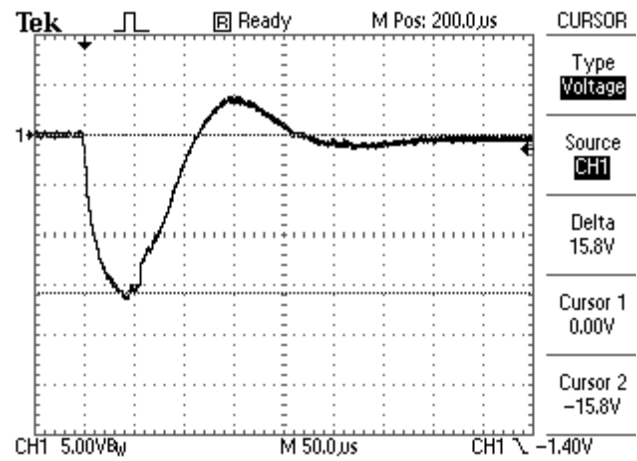

Fig. 9. Oscillogram of the pulsed A- component of the current of artificial lightning acting on the TS (point 5′, zone 1A) of thickness h=1.5 mm (I_{mA}= –15.8 V×12625 A/V = –199.5 kA; t_{mA}=42 μs; J_A=1.98·10^6 A^2·s)
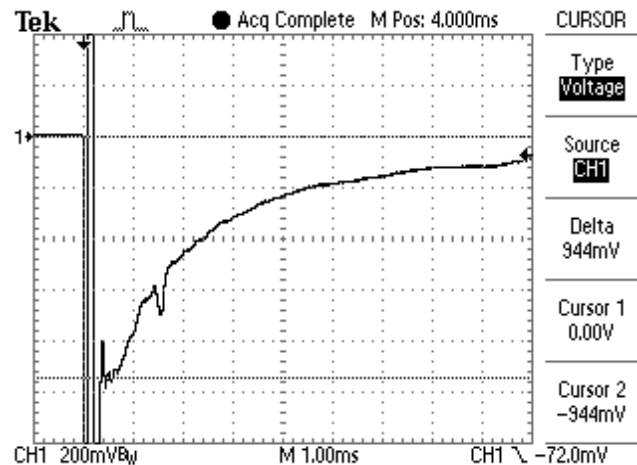
Fig. 10. Oscillogram of the intermediate B- component of the current of artificial lightning acting on the TS (point 5′, zone 1A) of thickness h=1.5 mm (I_{mB}= –0.944 V×6312 A/V= –5958 A; I_{LB}=q_B/τ_{pB}= –2400 A; τ_{pB}=5 ms; q_B= –12 C)
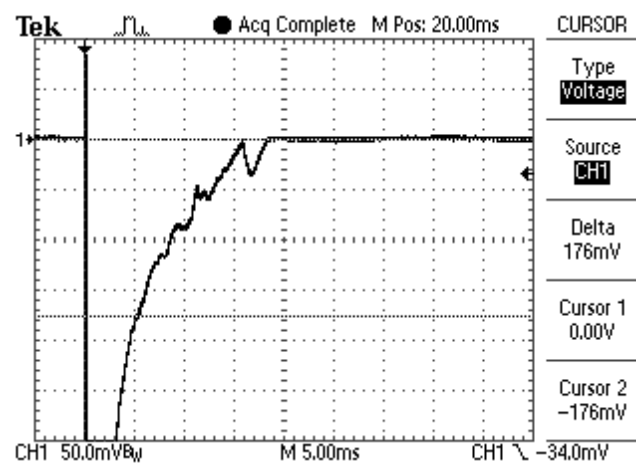

Fig. 11. Oscillogram of the shortened long-term C^*- component of the current of artificial lightning acting on the TS (point 5′, zone 1A) of thickness h=1.5 mm (I_{mC*}= –0.176 V×6312 A/V= –1111 A; I_{LC*}=q_{C*}/τ_{pC*}= –426 A; τ_{pC*}=13.6 ms; q_{C*}= –5.79 C)

Fig. 12. General view from the binding zone on the outer surface of the TS of a flat duralumin panel (h=1.5 mm) of the airplane's fuel tank of the plasma channel simulated at the UITOM-1 type installation of the lightning discharge of the results of the direct impact on this TS for zone 1A of the normalized components of the artificial lightning current, characterized by local thermal damage of the wall of the TS of the panel at the place of impact of the lightning channel to it
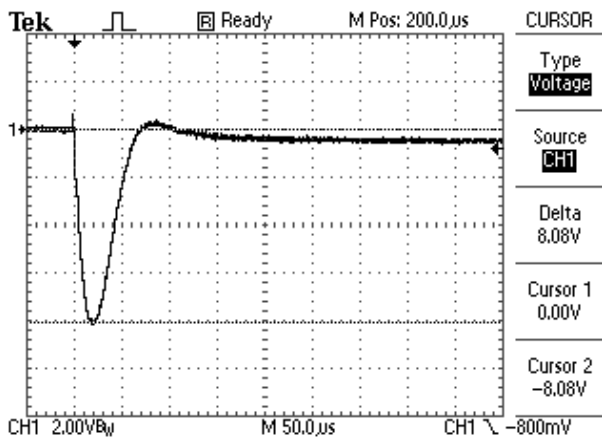

Fig. 13. Oscillogram of the repeated pulsed D- component of the lightning current acting on the TS (point 3', zone 2A) of thickness h=1.5 mm
(I_{mD}= –8.08 V×12625 A/V= –102 kA; t_{mD}=20 μs;
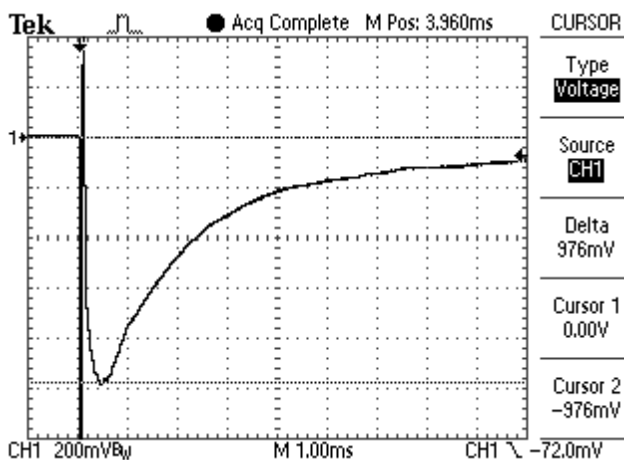J_D=0.26·10^6 A^2·s)

Fig. 14. Oscillogram of the intermediate B- component of the lightning current acting on the TS (point 3', zone 2A) of thickness h=1.5 mm
(I_{mB} = –0.976 V×6312 A/V= –6160 A; I_{LB}=q_B/τ_{pB}= –2366 A;
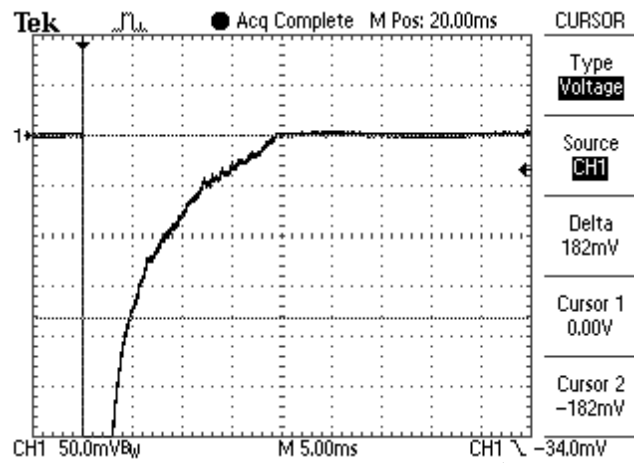τ_{pB}=5 ms; q_B= –11.83 C)

Fig. 15. Oscillogram of the shortened long-term C^*- component of the lightning current acting on the TS (point 3', zone 1A) of thickness h=1.5 mm
(I_{mC*}= –0.182 V×6312 A/V= – 1148 A; I_{LC*}=q_{C*}/τ_{pC*}= –416 A;
τ_{pC*}=14.8 ms; q_{C*}= –6.16 C)

The application at the final stage of the research carried out to the tested for thermal lightning resistibility in zone 2A in the discharge circuit of the UITOM-1 installation for a panel sample of high-strength aluminum alloy grade B95 with thickness of h=1.5 mm of the method of capillary control of the damage site of the TS from a direct impact of the channel of simulated lightning confirmed its through penetration.

Figure 16 shows the results of direct action for zone 1A on the TS of a flat duralumin panel with thickness h=1.2 mm of the aircraft's fuel tank of the corresponding artificial lightning current components with normalized ATPs. It is clearly seen that such an effect on the TS of the simulated at the LCG type UITOM-1 type the lightning discharge channel leads to through penetration of the wall of the duralumin panel of the aircraft's tank in the place of its (channel) binding on the outer surface of the TS. Here, the ATPs of the components of the artificial lightning current recorded in DSO for zones 1A and 2A did not differ significantly from the numerical data characteristic of their oscillograms shown in Fig. 9-11, 13-15.

Fig. 16. General view from the binding zone on the outer surface of the TS of a flat duralumin panel (h=1.2 mm) of the aircraft's fuel tank of the plasma channel simulated by the UITOM-1 installation of a lightning discharge of the results of direct exposure to this TS for zone 1A of the normalized components of the artificial lightning current, characterized by through local penetration of the TS panel wall at the point of impact of the lightning channel

Note that this through penetration from the direct thermal action of the plasma channel of the simulated lightning discharge of the wall of a flat duralumin panel with thickness h=1.2 mm of the aircraft's fuel tank (see Fig. 16) is unambiguously indicated by as the results of photographic recording of thermal sparks with an insulating pyramidal LTC from internal surface of the TS, as well as by the calculated estimation by (5) of the depth r_k and by (4) of the radius r_k of the hole for its penetration.

Figure 17 shows the results of direct thunderstorm discharges effect simulated on the LCG type UITOM-1 with normalized values of the ATPs of their current components for zone 1A to a wall with thickness of h=1.2 mm of the TS from the side of its inner surface. The experimental data shown in Fig. 17, confirm the conclusion that the TS with the necessary protective coatings of a panel made of an aluminum alloy of grade B95 with thickness h=1.2 mm of the aircraft's fuel tank for zone 1A does not satisfy condition (1) and is thermally unstable to direct action on it of A-, B- and C^*- current components of artificial lightning with ATPs normalized according to [3, 4].
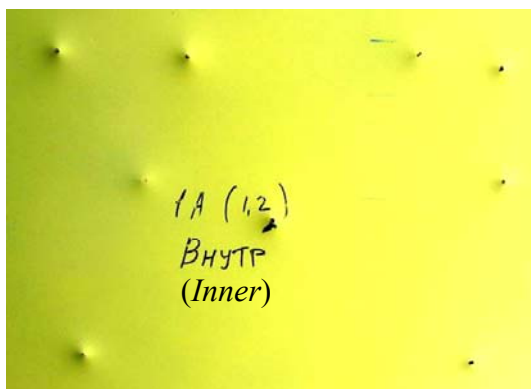

Fig. 17. General view of the TS of a flat duralumin panel (h=1.2 mm) of the aircraft's fuel tank from the side of its inner surface, the outer surface of which at various points in the discharge circuit of the UITOM-1 type installation was subjected to direct impacts of pulsed components of artificial lightning current corresponding to zone 1A

Conclusions.

1. The results of the calculation-experimental investigations carried out at the Scientific-&-Research Planning-&-Design Institute «Molniya» of the National Technical University «Kharkiv Polytechnic Institute» regarding the thermal resistibility of prototypes with required by technological conditions protective coatings of flat rectangular panels of a fuel tank with size of 550 mm × 800 mm and thickness h from 1.2 to 4 mm made of high-strength aluminum alloy of brand B95 of the designed domestic aircraft to direct impact on them according to the current requirements of US regulatory documents SAE ARP 5412 and SAE ARP 5416 of A-, B- and C^*- components of the current of artificial lightning (1A zone), as well as D-, B- and C^*- components of the artificial lightning current (zone 2A) with normalized ATPs indicate that the studied panels with thickness h=1.2 mm, h=1.5 mm and h=1.8 mm for zone 1A, as well as with thickness h=1.2 mm and h=1.5 mm for zone 2A are thermally unstable ($h \leq h_k$) to direct impacts in them of

a plasma channel of a lightning discharge simulated under laboratory conditions with the used components of a pulsed current of artificial lightning.

2. The thermal lightning resistibility of the studied panels with thickness h of the aircraft's fuel tank is determined by the ATPs of the shortened long-term C^*- current component of the artificial lightning, which causes the appearance of rounded penetration holes with radius r_k and depth h_k in them. To find the values of r_k and h_k in the indicated panels of the aircraft's fuel tank, struck in the earth's air atmosphere by a direct impact of a simulated lightning discharge in them, approximate calculated relationships (4), (5) are recommended. The operability of these relationships is confirmed by the results of field experiments performed using a powerful generator of pulsed current of artificial lightning of the UITOM-1 type.

3. In the event of a direct impact on a plane in an air atmosphere of a lightning plasma channel with normalized ATPs of the indicated components of its pulsed current, to prevent ignition of fuel vapors in the tank under study with walls made of high-strength aluminum alloy grade B95 and corresponding double-sided protective coatings of the designed aircraft and its accident, the thickness h of the wall of this fuel tank must be at least 1.8 mm when the tank is located in zone 2A of its lightning strike and at least 2 mm the tank is located in zone 1A of its lightning strike.

REFERENCES
1. Yuman M.A. *Molniya* [Lightning]. Moscow, Mir Publ., 1972. 327 p. (Rus).
2. Uman M.A. Natural and artificially-initiated lightning and lightning test standards. *Proceedings of the IEEE*, 1988, vol.76, no.12, pp. 1548-1565. **doi: 10.1109/5.16349.**
3. SAE ARP 5412: 2013. Aircraft Lightning Environment and Ralated Test Waveforms. SAE Aerospace. USA, 2013. − pp. 1-56.
4. SAE ARP 5416: 2013. Aircraft Lightning Test Methods. SAE Aerospace. USA, 2013. − pp. 1-145.
5. Baranov M.I., Koliushko G.M., Kravchenko V.I., Nedzel'skii O.S., Dnyshchenko V.N. A Current Generator of the Artificial Lightning for Full-Scale Tests of Engineering Objects. *Instruments and Experimental Technique*, 2008, no.3, pp. 401-405. **doi: 10.1134/s0020441208030123.**
6. Baranov M.I., Buriakovskyi S.G., Rudakov S.V. The tooling in Ukraine of model tests of objects of energy, aviation and space-rocket engineering on resistibility to action of pulsed current of artificial lightning. *Electrical engineering & electromechanics*, 2018, no.4, pp. 45-53. **doi: 10.20998/2074-272X.2018.4.08**.
7. Baranov M.I. *Izbrannye voprosy elektrofiziki. Monografiya v 3kh tomakh. Tom 2, Kn. 2: Teoriia elektrofizicheskikh effektov i zadach* [Selected topics of Electrophysics. Monograph in 3 Vols. Vol.2, Book 2. A theory of electrophysical effects and tasks]. Kharkiv, Tochka Publ., 2010. 407 p. (Rus).
8. Knopfel' G. *Sverkhsil'nye impul'snye magnitnye polia* [Ultra strong pulsed magnetic fields]. Moscow, Mir Publ., 1972. 391 p. (Rus).
9. Raiser Yu.P. *Fizika gazovogo razryada* [Physics of gas discharge]. Moscow, Nauka Publ., 1987. 592 p. (Rus).
10. Kuhling H. *Spravochnik po fizike. Per. s nem.* [Dictonary on Physics. Translated from German]. Moscow, Mir Publ., 1982. 520 p. (Rus).
11. Baranov M.I., Nosenko M.A. Influence of the thermal action of artificially-initiated lightning current on specimens of the

metal skin of an aircraft. *Journal of Engineering Physics and Thermophysics*, 2009, vol.82, no.5, pp. 978-987. **doi: 10.1007/S10891-009-0272-z.**

12. Baranov M.I., Kniaziev V.V., Rudakov S.V. Calculation and experimental estimation of results of electro-thermal action of rationed by the international standard IEC 62305-1-2010 impulse current of short blow of artificial lightning on the thin-walled coverage from stainless steel. *Electrical engineering & electromechanics*, 2017, no.1, pp. 31-38. **doi: 10.20998/2074-272X.2017.1.06.**

13. IEC 62305-1: 2010 «Protection against lightning. Part 1: General principles». Geneva, IEC Publ., 2010.

14. Available at: https://en.wikipedia.org/wiki/Duralumin (accessed 20 May 2018).

15. Available at: https://znanija.com/task/26630096 (accessed 10 June 2018).

16. Abramov N.R., Kuzhekin I.P., Larionov V.P. Characteristics of penetration of the walls of metal objects when exposed to lightning. *Electricity*, 1986, no.11, pp. 22-27. (Rus).

17. Baranov M.I., Buriakovskyi S.G., Rudakov S.V. The metrology support in Ukraine of tests of objects of energy, aviation and space-rocket engineering on resistibility to action of pulses of current (voltage) of artificial lightning and commutation pulses of voltage. *Electrical engineering & electromechanics*, 2018, no.5, pp. 44-53. **doi: 10.20998/2074-272X.2018.5.08.**

18. Baranov M.I., Kniaziev V.V., Rudakov S.V. The coaxial shunt for measurement of current pulses of artificial lightning with the amplitude up to ±220 kA. *Instruments and Experimental Technique*, 2018, vol.61, no.4, pp. 501-505. **doi: 10.1134/S0020441218030156**

19. Baranov M.I., Rudakov S.V. Electrothermal action of the pulse of the current of a short artificial-lightning stroke on test specimens of wires and cables of electric power objects. *Journal of Engineering Physics and Thermophysics*, 2018, vol.91, no.2, pp. 544-555. **doi: 10.1007/s10891-018-1775-2.**

M.I. Baranov[1], *Doctor of Technical Science, Professor,*
S.G. Buriakovskyi[1], *Doctor of Technical Science, Professor,*
A.S. Hrytsenko[2], *Lead Research Engineer,*
V.A. Kostiuk[2], *Chief Designer,*
[1] Scientific-&-Research Planning-&-Design Institute «Molniya»,
National Technical University «Kharkiv Polytechnic Institute»,
47, Shevchenko Str., Kharkiv, 61013, Ukraine,
phone +38 057 7076841,
e-mail: baranovmi@kpi.kharkov.ua,   sergbyr@i.ua
[2] Antonov Company,
1, Akademika Tupoleva Str., Kyiv, 03062, Ukraine,
phone +38 044 4543233,   e-mail: info@antonov.com

Yu.V. Batygin, E.A. Chaplygin, S.A. Shinderuk, V.A. Strelnikova

NUMERICAL ESTIMATES OF CURRENTS AND FORCES IN LINEAR TOOLS OF THE MAGNETIC-PULSE ATTRACTION OF METALS. PART 2: HIGH ELECTRICAL CONDUCTANCE METALS

Purpose. The purpose of the present work is substantiating workability of the linear tools of the magnetic-pulse attraction of thin-walled sheet metals with high electrical conductance, the principle of which is based on the force interaction of two conductors with unidirectional currents during intensive penetration of the acting electromagnetic fields. Constructively, one of these conductors in the linear tools is the so-called main current lead (an analog of the inductor in EMF) and the second one is the part of the sheet metal which has to be deformed. Methodology. For numerical estimates the analytical dependences are obtained with help of the methods of electromagnetic field theory as well the standard programs from the Wolfram Mathematica package used. Results. The fulfilled calculations illustrate the amplitude-temporal dependences for the excited currents and forces under the demanded decrease of the operating frequencies of the acting electromagnetic fields. The efficiency of the linear magnetic-pulse tools is based on the excitation of the mutual attraction forces of conductors with low-frequency unidirectional currents. Originality. By the example of aluminum, which is the main raw material in modern aviation and automotive industry, it has been found that for processing the metals with high electrical conductance demand a significant decreasing operating frequencies, what is necessary for intensifying the penetration processes of acting fields and, accordingly, for exciting the real attractive forces. Practical value. The results of the work allow formulating the based recommendations for the creation and practical application of the linear magnetic-pulse attraction tools for the progressive technologies of restoring the damaged areas of bodies coatings from the thin-walled sheet metals with the high specific electrical conductivity. References 10, figures 4.
Key words: **metals with high electrical conductance, intensive field penetration, magnetic-pulse attraction of conductors with unidirectional currents, linear tools for eliminating dents in body coatings.**

Мета. Метою роботи є обґрунтування дієздатності лінійних інструментів магнітно-імпульсного притягання тонкостінних листових металів з високою питомою електропровідністю, принцип дії яких заснований на силовій взаємодії провідників з односпрямованими струмами при інтенсивному проникненні збуджених полів. Методика. Для чисельних оцінок використовувалися аналітичні залежності, отримані за допомогою методів теорії електромагнітного поля, і стандартні програми з пакету «Wolfram Mathematica». Результати. Проведені обчислення ілюструють амплітудно-часові залежності для збуджених струмів і сил при необхідному зниженні робочих частот діючих електромагнітних полів. Обґрунтовано дієвість лінійних магнітно-імпульсних інструментів, заснованих на збудженні сил взаємного притягання провідників з низькочастотними односпрямованими струмами. Наукова новизна. На прикладі з алюмінієм, який є основним сировинним матеріалом у сучасному авіа- та автомобілебудуванні, встановлено, що для металів з високою питомою електропровідністю потрібно значне зниження робочих частот, що необхідно для інтенсифікації процесів проникнення діючих полів і, відповідно, для збудження реальних сил притягання. Практичне значення. Результати роботи дозволяють сформулювати обґрунтовані рекомендації щодо створення та практичного застосування лінійних інструментів магнітно-імпульсного притягання в прогресивних технологіях відновлення пошкоджених ділянок корпусних покриттів з тонкостінних листових металів з високою питомою електропровідністю. Бібл. 10, рис. 4.
Ключові слова: **метали з високою питомою електропровідністю, інтенсивне проникнення поля, магнітно-імпульсне притягання провідників з односпрямованими струмами, лінійний інструмент усунення вм'ятин в корпусних покриттях.**

Цель. Целью работы является обоснование дееспособности линейных инструментов магнитно-импульсного притяжения тонкостенных листовых металлов с высокой удельной электропроводностью, принцип действия которых основан на силовом взаимодействии проводников с однонаправленными токами при интенсивном проникновении возбуждаемых полей. Методика. Для численных оценок использовались аналитические зависимости, полученные с помощью методов теории электромагнитного поля, и стандартные программы из пакета «Wolfram Mathematica». Результаты. Проведенные вычисления иллюстрируют амплитудно-временные зависимости для возбуждаемых токов и сил при требуемом понижении рабочих частот действующих электромагнитных полей. Обоснована действенность линейных магнитно-импульсных инструментов, основанных на возбуждении сил взаимного притяжения проводников с низкочастотными однонаправленными токами. Научная новизна. На примере с алюминием, который является основным сырьевым материалом в современном авиа- и автомобилестроении, установлено, что для металлов с высокой удельной электропроводностью требуется значительное понижение рабочих частот, что необходимо для интенсификации процессов проникновения действующих полей и, соответственно, для возбуждения реальных сил притяжения. Практическое значение. Результаты работы позволяют сформулировать обоснованные рекомендации по созданию и практическому применению линейных инструментов магнитно-импульсного притяжения в прогрессивных технологиях восстановления повреждённых участков корпусных покрытий из тонкостенных листовых металлов с высокой удельной электропроводностью. Библ. 10, рис. 4.
Ключевые слова: **металлы с высокой удельной электропроводностью, интенсивное проникновение поля, магнитно-импульсное притяжение проводников с однонаправленными токами, линейный инструмент устранения вмятин в корпусных покрытиях.**

Introduction. The growing interest in advanced environmentally friendly high-performance technologies based on the use of pulsed magnetic field energy is due to

the practical needs of various branches of modern industry, including not only the production of nomenclature products, but also their recovery from damage during operation [1-3].

An extensive sector of processing technologies, the development of which is determined by the requirements of, for example, vehicle manufacturers, combines a set of methods for the restoration of metal coatings of the elemental base of their hull components. The demand for such technologies follows from the negatives of operational practice. So, dents on the surface of the aircraft lead to a change in its aerodynamic characteristics and a number of possible emergency situations. Damage to the bodies of water and land vehicles is not only a violation of aesthetics. In some force majeure circumstances, they can cause crashes on the water and deaths on the roads [4].

Literature review. Well-known and widespread mechanical dent-cleansing technologies are simple and relatively cheap to implement. But their performance, reliability, quality and environmental performance remain very low. So, quite often, the mechanical pulling of a dent metal leads to a violation of its integrity. The problem that has arisen requires its own separate approach to solving it.

Using the energy of pulsed magnetic fields opens up new possibilities for creating progressive restoration technologies that are free from the above disadvantages. Among them, the elimination of dents using linear tools of magnetic-pulse attraction of damaged sections of thin-walled sheet metal coatings of automobile bodies, airframes and water vehicles. The effectiveness of such tools is based on Ampere law, according to which conductors with unidirectional currents experience mutual attraction [5, 6]. Structurally, such conductors in a linear tool are the main current lead (an analog of an inductor in traditional magnetic pulse metal processing [1, 3]) and a restored area of damaged metal. Geometrically, they (current lead and processed metal) are parallel. Electrically, their connection with respect to common point contacts with a high-voltage power source can be parallel or serial [1, 7, 8]. As follows from physical considerations, the main obstacle to the effective excitation of the electrodynamic forces of interaction between the conductors in such a system is the induction effects, and, respectively, which the current in the main current lead induces a countercurrent in the sheet workpiece, and the current in its metal induces a countercurrent in the main conductor.

In general, the main advantages of a linear tool of magnetic-pulse attraction of sheet metals are, first of all, the simplicity of technical implementation, high production rates and the reliability of the production operation performed (in the sense of preservation of the restored object) [8]. Among the promising technologies of magnetic-pulse attraction of sheet metals, allowing the restoration of damaged areas from the outside of the vehicle bodies, it is worth noting the theoretically and experimentally sound proposals formulated by the authors of [9, 10].

Concluding our review of publications on this topic, we emphasize the versatility of magnetic-pulse power tools on sheet metals with various electrophysical characteristics. The objects of processing can be not only of steel, but also of aluminum alloys. Moreover, the latter are increasingly used for the manufacture of light and durable technical structures for various purposes. From the physical point of view, the noted universality is provided by the possibilities of adjusting the operating frequencies from the source of the acting electromagnetic fields, which allows the attraction or repulsion of predetermined sections of sheet metals in any stamping and restoration production operations [1, 3, 7].

The goal of the paper is determination of conditions and performance assessment of linear tools of magnetic-pulse attraction of specified sections of sheet metals with a high value of electrical conductance.

To achieve this goal, it is necessary to calculate the characteristics of electrodynamic processes while lowering the operating frequencies of current pulses, which, physically, allows to vary the intensity of the penetration of excited fields into the metal elements of the object of study. The result of the calculations should be the numerical estimates and the physical and mathematical illustrations necessary to determine the conditions for the effective excitation of electrodynamic forces in the working areas of linear tools of magnetic-pulse attraction. In fairness, it should be noted that a similar problem has already been considered by the authors of publications [7, 8]. However, the direct use of the formulas obtained by them for calculations and analysis of the ongoing processes is not possible due to the limited results found in [7, 8] for the formulation and solution of the problems under consideration.

In solving this problem, we use the physic-mathematical model of the magnetic-pulse attraction tool under study and the functional dependencies for the characteristics of the ongoing electrodynamic processes described in [6]. For clarity of the further presentation, we indicate the main provisions, partially repeating the publication material [6].

Accepted assumptions and problem definition:

• schematic diagrams of the implementation of magnetic-pulse attraction of thin-walled metals in linear tools, as well as the calculation model (cross section of the system under study) are presented in Fig. 1;

• non-magnetic sheet metal (for example, aluminum or its alloys) with sufficiently large transverse dimensions, the thickness d and the electrical conductance γ is subject to attraction;

• there is geometric symmetry with respect to the ZOX coordinate plane. Along the abscissa axis OX, the system under study has a sufficiently large extent, so that the corresponding differentiation operator is $\partial/\partial x = 0$;

• in the main current lead connected to the high-voltage power source and in a parallel section of sheet metal, exciting currents with given amplitude-temporal characteristics flow only in the longitudinal direction (Fig. 1,b).
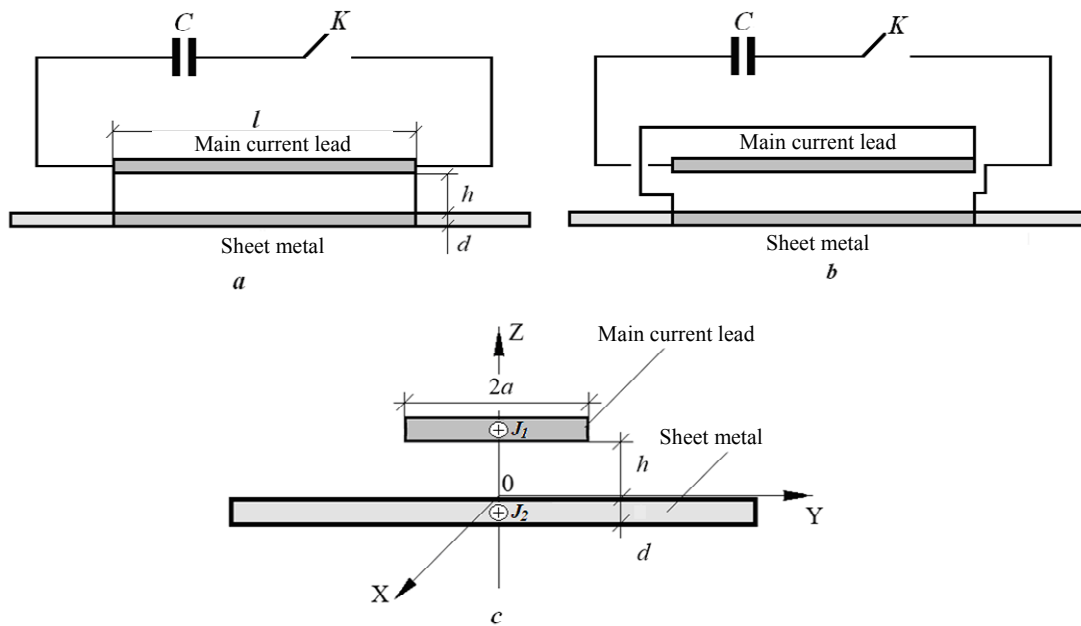
Fig. 1. Linear tools of magnetic-pulse attraction of thin-walled sheet metals:
a – circuit diagram of parallel connection, *b* – circuit diagram of serial connection; *c* – calculation model;
C – capacitive energy storage, *K* – switch; $J_{1,2}$ – flowing currents in the current lead and the metal being processed

Solution algorithm. As follows from the assumptions made, nontrivial components of the electromagnetic field vector are excited in the system under study: $E_x \neq 0$, $H_{y,z} \neq 0$, which are found by integrating the Maxwell equations.

From Ohm law in differential form, the currents induced in the main current lead and the corresponding section of the sheet metal are determined from the known electric field strength. The superposition of the current from the high-voltage power source and the induced current makes it possible to find the amplitude-temporal characteristics of the total currents in each of the conductive elements of the linear tool of magnetic-pulse attraction.

To maximize the force interaction of the conductors, the currents flowing in them should be the same (this condition is practically ensured by the appropriate choice of the parameters of the linear tool). In this case, according to Ampere law, the force of attraction, excited in the working area between the main current lead and sheet metal, is found as a value proportional to the square of the currents flowing in them.

Omitting the cumbersome calculated analytical dependences rather strictly justified and given in [6], we turn to numerical estimates of the characteristics and analysis of processes in a linear tool of magnetic-pulse attraction.

Numerical estimates are carried out for the following initial data:

1. Aluminum sheet samples with thickness of d = 0.0008 m and the specific conductance of $\gamma = 3.75 \cdot 10^7$ 1/Ω·m are subject to deformation.

2. The tool's main current lead is also made of aluminum of the same thickness as the object being processed (the electrodynamic system «aluminum-aluminum» is considered).

3. The length and width of the working area l = 0.06 ... 0.1 m and $2a$ = 0.01 m, respectively, the distance between the conductors of the linear tool is $h = 0.002$ m.

4. The main current lead and the given section of the metal being processed are identical, geometrically and electrically parallel, so that the exciting currents flowing in the circuit of each of them are the same.

Note. According to Ampere law, the last initial premise makes it possible to achieve maximum forces of interaction of conductors with unidirectional currents [5, 6].

The parameters of current pulses are determined by the characteristics of the power source – magnetic pulse installation МИУС-2 [2], developed and created at the Laboratory of Electromagnetic Technologies of the Department of Physics of Kharkiv National Automobile and Highway University [1]. We assume that for the specified electrical installation:

1. The maximum voltage on the capacitive storage is U = 2000 V.

2. The natural operating frequency (in a short-circuit discharge circuit) is f_{max} = 7000 Hz and the relative attenuation coefficient is $\delta/\omega = 0.3$.

3. The temporal shape of the exciting current in the attraction operation is an aperiodic unipolar signal with operating frequency of f_p = 1000 ... 1500 Hz and the relative attenuation coefficient of $\delta/\omega \approx 0.3$.

4. The tool is connected to the power source through a matching device, providing a decrease in the operating frequency to the required value, with the coefficient of energy transfer to the working area of $K \approx 4$.

The calculations were carried out similarly to how it was done in [6] using standard programs from the Wolfram Mathematica package. Separately, it should be pointed out that the mathematical rigor of the performed calculations (with an average error up to ~ 7.5 %) was established by the appropriate choice of the intervals of numerical integration and the number of terms in the sums of discrete expansions in the expressions for the characteristics of the electromagnetic processes under study.

Graphs of excited currents and electrodynamic attractive forces depending on their phase ($\varphi = \omega \cdot t$, ω is the circular frequency, t is time) are presented in Fig. 2-4.
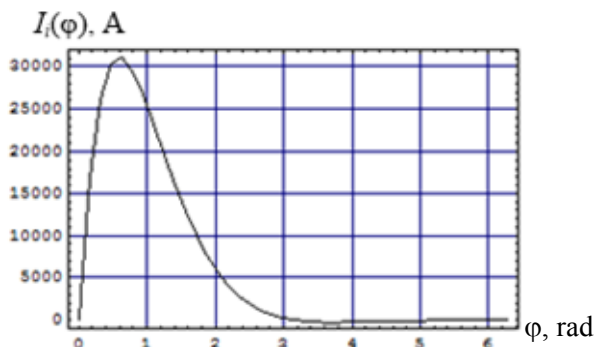

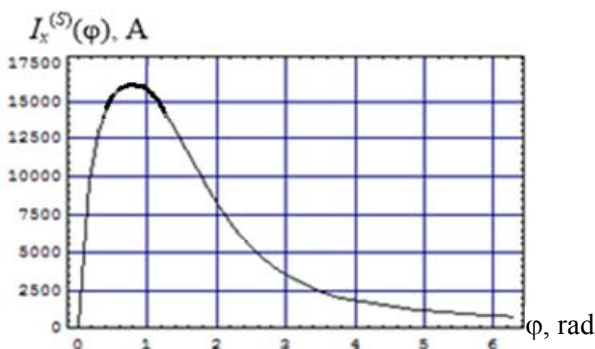Fig. 2. Excitation current from a high voltage power source

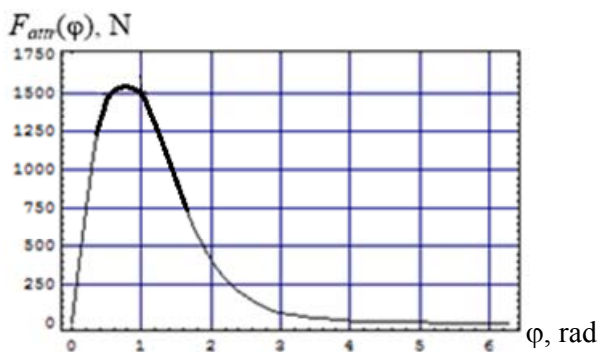Fig. 3. Total current in each of the conductors of the linear tool

Fig. 4. Excited magnetic-pulse attraction force

An analysis of the results of the calculations shows that:

• in the accepted operating conditions of a linear instrument, induction effects have a significant influence on electromagnetic processes in the conductors of the system under study;

• the amplitude of the total current in the main current lead and sheet metal decreases and is up to ~ 49 % of the current amplitude from a high-voltage power source (~ 32 kA – source, ~ 15.7 kA – induced current, ~ 16.3 kA – total current);

• the amplitude of the excited attractive force is close to ~ 1520 N;

• under accepted conditions, this force indicator should provide magnetic-pulse attraction of sheet aluminum (metal with high electrical conductance) using the linear tool under consideration [3];

• an appropriate choice of the geometry of the working zone and the temporal characteristics of the exciting current makes it possible to obtain fairly close numerical indicators of electrodynamic processes in the system under study when working with both aluminum and steel [6].

Conclusions.

1. On the example of aluminum processing, the performance conditions of linear tools of magnetic-pulse attraction of specified sections of sheet metals with high value of electrical conductance are determined.

2. It has been established that successful magnetic-pulse attraction is possible at sufficiently low operating frequencies of exciting currents (~ 1500 Hz), which provides intensive penetration of electromagnetic fields into the conductors of the tool of the production operation and the excitation of powerful forces of magnetic pressure from the outside.

3. It is shown that, under the accepted conditions, induction effects have a significant influence on electromagnetic processes in the conductors of a linear tool and reduce the excited currents by ~ 45 % relative to the current from the high-voltage power source.

REFERENCES
1. Batygin Yu.V., Chaplygin E.A., Shinderuk S.A., Strelnikova V.A. The main inventions for technologies of the magnetic-pulsed attraction of the sheet metals. A brief review. *Electrical engineering & electromechanics*, 2018, no.3, pp. 43-52. **doi: 10.20998/2074-272X.2018.3.06.**
2. Eguia I., Mangas A., Iturbe R., Gutierrez Ma.A. Electromagnetic forming of longitudinal strengthening ribs in roll formed automotive profiles. *Proceedings of 4th International Conference on High Speed Forming. ICHSF 2010, Columbus*, 2010, pp. 198-207. **doi: 10.17877/DE290R-12593.**
3. Psyk V., Risch D., Kinsey B.L., Tekkaya A.E., Kleiner M. Electromagnetic forming – A review. *Journal of Materials Processing Technology*, 2011, vol.211, no.5, pp.787-829. **doi: 10.1016/j.jmatprotec.2010.12.012**.
4. Welcome to BETAG Innovation. Available at: http://www.betaginnovation.com (accessed 17 June 2018).
5. Landau L.D., Lifshits E.M. *Elektrodinamika sploshnyh sred T. 8* [Continuum Electrodynamics. Vol.8]. Moscow, Fizmatlit Publ., 2005. 656 p. (Rus).

6. Batygin Yu.V., Chaplygin E.A., Shinderuk S.A., Strelnikova V.A. Numerical estimates of currents and forces in linear tools of the magnetic-pulse attraction of metals. Part 1: Low electrical conductance metals. *Electrical engineering & electromechanics*, 2019, no.5, pp. 40-44. **doi: 10.20998/2074-272X.2019.5.07.**
7. Batygin Yu.V., Chaplygin E.A., Shinderuk S.A. Calculation of fields and currents in the induction system with the attractive screen and the additional coil as a tool for the straightening. *Electrical engineering & electromechanics*, 2015, no.1, pp. 57-62. (Rus). **doi: 10.20998/2074-272X.2015.1.11**.
8. Batygin Yu.V., Chaplygin E.A., Sabokar O.S. Magnetic pulsed processing of metals for advanced technologies of modernity – a brief review. *Electrical engineering & electromechanics*, 2016, no.5, pp. 35-39. **doi: 10.20998/2074-272X.2016.5.05**.
9. Gnatov A., Argun S. New method of car body panel external straightening: tools of method. *International Journal of Vehicular Technology*, 2015, vol.2015, pp. 1-7. **doi: 10.1155/2015/192958.**
10. Hnatov A., Arhun S., Dziubenko O., Ponikarovska S. Choice of electric engines connection circuits in electric machine unit of electric power generation device. *Majlesi Journal of Electrical Engineering*, 2018, vol.12, no.4, pp. 85-93.

Yu.V. Batygin[1]*, Doctor of Technical Science, Professor,*
E.A. Chaplygin[1]*, Candidate of Technical Science, Associate Professor,*
S.A. Shinderuk[1]*, Candidate of Technical Science, Associate Professor,*
V.A. Strelnikova[1]*, Postgraduate Student,*
[1] Kharkiv National Automobile and Highway University,
25, Yaroslava Mudrogo Str., Kharkov, 61002, Ukraine,
phone +380 57 7003852,
e-mail: yu.v.batygin@gmail.com;   chaplygin.e.a@gmail.com;
s.shinderuk.2016102@ukr.net;   v.strelnikova91@gmail.com

G.V. Bezprozvannych, A.V. Roginskiy

EFFICIENCY OF APPLICATION OF SEMICONDUCTIVE COATINGS FOR REGULATION OF ELECTRIC FIELD IN HIGH-VOLTAGE INSULATION OF ELECTRIC MACHINES

Introduction. Intensification of competition and the desire to reduce the cost of high-voltage electric machines due to a significant increase in the electrical and thermal loads of the electrical insulation system complicate the operation of anti-corona coatings on the insulation surface of the stator winding and increase the intensity of discharge processes, which significantly reduce the life of the insulation in case of failure of the coatings. Purpose. The analysis of the efficiency of alignment of the electric field along the insulation surface of the stator winding of high-voltage electric machines with semiconductor anti-corona coatings. Methodology. A method for calculating the electric potential distribution along the surface of the winding insulation during the use of semiconductive coatings providing alignment decrease the electric field and eliminating the appearance of moving discharges. The reliability of the calculations is confirmed by experimental studies of the potential distribution over the surface of the anti-corona semiconducting non-linear coating along the frontal part of the samples of the rod of the hydrogenerator for a linear voltage of 20 kV. Practical value. The proposed methodology for calculating the distribution of the electric field over the surface of the insulation and the anti-corona semiconductive coating can be applied to justify the length of the coating in the frontal part of high-voltage electrical machines depending on the electrophysical characteristics of the coating, electrical insulation, and thickness. The results of an experimental verification of the stability of the nonlinear properties of coatings during prolonged electrical and thermal aging of specially made coating samples are presented. References 14, figures 6.

Key words: **frontal part of the rod, external partial discharges, electric field, regulation of the electric field, semiconductive coating, surface resistivity, distribution of electric potential, stability of nonlinear properties, long-term electric and thermal aging**.

Представлена методика розрахунку розподілу електричного поля по поверхні ізоляції і протикоронного напівпровідного покриття в лобовій частині стрижня високовольтної електричної машини. Отримано в залежності від питомого поверхневого опору напівпровідного покриття розподіл електричного потенціалу по поверхні протикоронного покриття та ізоляції. Обґрунтовано діапазон значень питомого поверхневого опору протикоронного покриття для ефективного регулювання електричного поля. Достовірність розрахунків підтверджено експериментальними дослідженнями розподілу потенціалу по поверхні протикоронного напівпровідного нелінійного покриття уздовж лобової частини зразків стрижнів гідрогенератора на лінійну напругу 20 кВ. Представлено результати експериментальної перевірки стабільності нелінійних властивостей покриттів в процесі тривалого електричного і теплового старіння спеціально виготовлених зразків покриття. Ефективність регулювання електричного поля напівпровідними покриттями підтверджено результатами випробувань зразків стрижнів гідрогенератора СВ -1500 / 100-12 в початковому стані і після комплексного тривалого впливу електричного поля і температури. Бібл. 14, рис. 6.

Ключові слова: **лобова частина стрижня, зовнішні часткові розряди, електричне поле, регулювання електричного поля, протикоронне напівпровідне покриття, питомий поверхневий опір, розподіл електричного потенціалу, стабільність нелінійних властивостей, тривале електричне і теплове старіння.**

Представлена методика расчета распределения электрического поля по поверхности изоляции и противокоронного полупроводящего покрытия в лобовой части стержня высоковольтной электрической машины. Получено в зависимости от удельного поверхностного сопротивления полупроводящего покрытия распределение электрического потенциала по поверхности противокоронного покрытия и изоляции. Обоснован диапазон значений удельного поверхностного сопротивления противокоронного покрытия для эффективного регулирования электрического поля. Достоверность расчетов подтверждена экспериментальными исследованиями распределения потенциала по поверхности противокоронного полупроводящего нелинейного покрытия вдоль лобовой части образцов стрежней гидрогенератора на линейное напряжение 20 кВ. Представлены результаты экспериментальной проверки стабильности нелинейных свойств покрытий в процессе длительного электрического и теплового старения специально изготовленных образцов покрытия. Эффективность регулирования электрического поля полупроводящими покрытиями подтверждена результатами испытаний образцов стрежней гидрогенератора СВ 1500/100-12 в исходном состоянии и после комплексного длительного воздействия электрического поля и температуры . Библ. 14, рис. 6.

Ключевые слова: **лобовая часть стержня, внешние частичные разряды, электрическое поле, регулирование электрического поля, противокоронное полупроводящее покрытие, удельное поверхностное сопротивление, распределение электрического потенциала, стабильность нелинейных свойств, длительное электрическое и тепловое старение.**

Introduction. One of the main problems in the manufacture of high-voltage electric machines is the suppression of external partial discharges that occur in the slot part of the winding due to the potential difference between the insulation surface and the stator core and in

the frontal part due to a sharp jump in the electric field at the exit of the winding from the slot [1-3].

The regulation of the electric field in the insulation of the stator winding, which suppresses partial discharges in the air gaps between the insulation surface and the slot walls and elimination of the sliding discharges along the insulation surface in the places where the windings exit the stator slot, consists in the use of conductive and semiconductive coatings. Intensification of competition and the desire to reduce the cost of high-voltage electric machines due to a significant increase in the electrical and thermal loads of the electrical insulation system complicate the operation of anti-corona coatings on the insulation surface of the stator winding and increase the intensity of discharge processes, which significantly reduce the life of the insulation in case of coating failure [4-9]. In connection with the foregoing, the need arises for the use of anti-corona coatings that provide effective regulation of the electric field during operation of high-voltage electric machines.

The goal of the paper is analysis of the efficiency of alignment of the electric field along the insulation surface of the stator winding of high-voltage electric machines with semiconductive anti-corona coatings.

Problem definition. Case insulation of the stator winding is the most loaded element, subjected to the simultaneous influence of an electric field, temperature and thermomechanical stresses. Particularly high requirements for modern insulation systems are imposed in connection with the design and manufacture of powerful air-cooled turbo-generators. The permissible working electric field strength of the case insulation (in the region of the flat side of the rod) reaches values (3-3.2) kV/mm for insulation made by vacuum-injection impregnation for conductors with optimized geometry (with rounded corners) [2, 3]. An increase in the requirements for the reliability of powerful electric machines has led to the need to use in the manufacture of stator case insulation of materials characterized by increased stability of physico-chemical and electrical insulation properties. Traditionally, combined mica tapes are used for this purpose, in which glass tapes are used as a substrate, and mica papers impregnated with epoxy resin are used as a dielectric barrier. The increase in the content of mica in mica paper provides a significant increase in long-term electrical insulation strength [10]. The level of electric field at which the electrical insulation of the slot of the rod works depends on the nominal voltage of the machine, the thickness of the insulation, and the configuration of the surface of the copper of the rod and the slot of the stator. As a rule, modern powerful turbogenerators have slots and rods of a rectangular shape. With this shape of the electrodes, the maximum values of the electric field strength [11] occur at the corners of the current-carrying rod (Fig. 1, curve 5: the equipotential surface is $\varphi = \pi$, the force line number is $\psi = 0$), and the insulation is extremely irregularly loaded over the slot volume. In the corner of the slot, i.e. for $\varphi = 0$ and $\psi = 0$, the electric field strength is 0 (Fig. 1,

curve 3). The degree of alignment of the electric field in the stator slot is characterized by the coefficient of electric field non-uniformity K equal to the ratio of the maximum field strength E_{max} taking place in the slot to the uniform field strength E_{midl}, i.e. at a sufficient distance from the angle of the current-carrying rod (Fig. 1, curve 1: equipotential surface $\varphi = \pi/2$ and $\psi \rightarrow \infty$).

The slot part of the stator winding section is installed in the slot of the core freely, the existing irregularities and the spread in the dimensions of the slot of the core and section determine the presence of some air gap (not more than 1 mm) between the insulation surface and the core. A two-layer insulation system is formed: solid insulation – gaseous dielectric (air). Breakdown of the air interlayer (partial discharge), which is under conditions of a strong inhomogeneous electric field, will occur at a voltage lower than the working one [11-13].
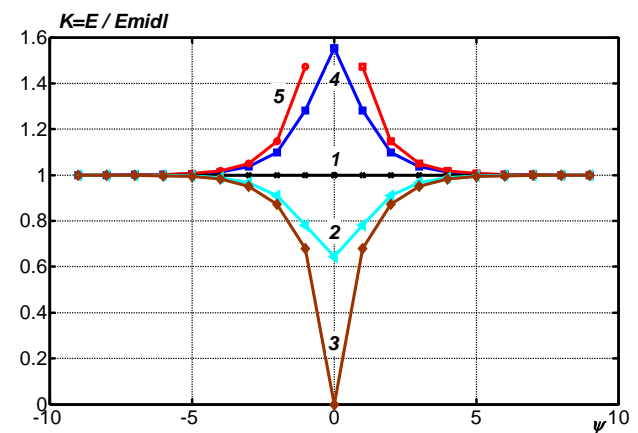

Fig. 1. The coefficient of non-uniformity of the electric field K in the slot of the stator winding of the turbogenerator for linear voltage of 20 kV:
curve 1 – $\varphi = \pi/2$ and $\psi \rightarrow \infty$;
curve 2 – $\varphi = \pi/4$ and $\psi = 0$; curve 3 – $\varphi = 0$ and $\psi = 0$;
curve 4 – $\varphi = 3/4\pi$ and $\psi = 0$; curve 5 – $\varphi = \pi$ and $\psi = 0$

A semiconductive coating electrically connected to the walls of the slot is applied over the insulation of the rod. Such a coating with a low value of specific surface resistance («*conductive*») provides contact at many points between the coating and the walls of the slot, that is, the entire surface of the slot part is grounded. As a result, the potential difference between the insulation surface and the slot wall is eliminated. This is usually graphite-based tape or varnish. On the one hand, the conductivity of the coating should be sufficient to eliminate partial discharges in the slot, which develop when a potential difference occurs between the insulation surface and the stator. On the other hand, it should not be less than a certain level at which the stator sheets are closed, which in turn leads to the appearance of eddy currents and an increase in losses. The specific surface resistance of the slot coating ρ_s lies in the range $(10^2 - 10^4)$ Ω, which reduces the probability of breakdown of air gaps between the rod and the slot wall.

In the frontal parts, the rods with insulation are in a gas environment. Most of the voltage falls on the gas

gaps. In this case, the component of the electric field strength along the surface becomes less than the critical intensity of the beginning of ionization of air or hydrogen [11-13]. The slot (conductive) coating extends beyond the slot to eliminate corona at the exit of the winding from the slot, where the electric field strength in the air is high enough for the development of discharge processes. In the absence of protective measures at the place where the rod exits from the slot, there is a sharp jump in the electric field strength, which can lead to the appearance of external edge discharges (corona and discharges along the surface of solid insulation) on the surface of the frontal part of the coil or rod of the electric machine. To eliminate the effect of corona, it is necessary to ensure a smooth distribution of the electric potential over the insulation surface of the frontal parts of the rods.

Regulation of the electric field in the frontal part of the insulation of the stator winding of high-voltage electric machines. An anti-corona coating which has large values of specific surface resistance (10^5-10^9) Ω is used in the frontal part [6-8]. In the frontal parts, a semiconductive layer is applied over a length of 20–25 cm. For this purpose, semiconductive coatings made on the basis of enamel are used [6-8], in which fillers are conductive powders: carbon black or graphite with a linear current-voltage characteristic. The dispersion of carbon black or graphite significantly affects the operational properties of anti-corona protection [9].

Most preferred are nonlinear coatings with a pronounced increasing dependence of the specific surface conductivity on the electric field strength (Fig. 2).

The coating creates a section of length l_s with specific surface resistance ρ_s (Fig. 3), and the surface resistance of the coating is much less than the surface insulation resistance ρ_{inss}. Because $\rho_s \ll \rho_{inss}$, then the component of the electric field strength E_{Os} along the insulation surface at the point O decreases. But at the end of the coating (at point K), a new region is formed with a sharply uniform field.
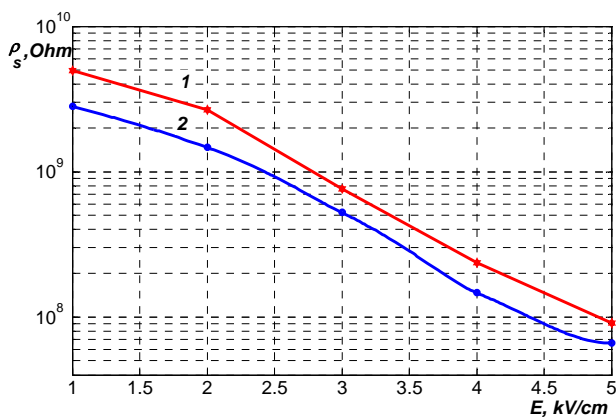
Fig. 2. Experimental dependence of the electric field strength of the rectified frequency of the specific surface resistance of the anti-corona coating based on a nonlinear compound (curve 1) and the coating in the form of a tape (curve 2)
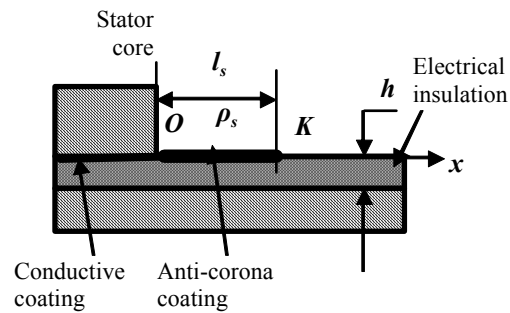
Fig. 3. Schematic representation of a fragment of the frontal Part of the rod with insulation and anti-corona coating

In the absence of a semiconductive coating, the electric field strength at point O

$$E_{oo} = U_o \sqrt{\omega \rho_{inss} C_s} = U_o \sqrt{\omega \rho_{inss} \varepsilon_0 \varepsilon / h}, \quad (1)$$

where U_o is the potential (voltage) at the point O; $\omega = 2\pi f$ is the circular frequency; $C_s = \varepsilon_0 \varepsilon / h$ is the insulation capacitance of thickness h with dielectric permeability ε; $\varepsilon_0 = 8.85 \cdot 10^{-12}$ F/n is the electric constant.

In the presence of a semiconductive coating, the electric field becomes equal

$$E_{Os} = U_o \sqrt{\omega \rho_s \varepsilon_0 \varepsilon / h}, \quad (2)$$

i.e. coating provides a reduction of E_{oo} in $\sqrt{\rho_{inss} / \rho_s}$ times.

Capacitive currents flowing through a semiconductive coating cause a voltage drop along the coating, resulting in E_K becomes less in comparison with E_{oo}, i.e. in the absence of coating. The electric field strength at the edge of the coating is determined by the expression

$$E_K = 2U_o \sqrt{\omega \rho_{inss} \varepsilon_0 \varepsilon / h} \exp(-\sqrt{\omega \rho_s \varepsilon_0 \varepsilon / 2h} \cdot l_s). \quad (3)$$

By choosing the values of l_s and ρ_s, it is possible to reduce E_{oo} and E_K to acceptable levels at which there are no surface discharges.

The condition for choosing the values of the specific surface resistance ρ_s of the semiconductive coating is the inequality $E_{Os} \leq E_{Od}$, which together with expression (1) for determining the electric field strength at the point O E_{oo} makes it possible to determine the upper boundary of the specific surface resistance of the semiconductive coating

$$\rho_s \leq \frac{E_{Od} \, h}{\omega \varepsilon_0 \varepsilon U_{so}^2}, \quad (4)$$

where U_{so} is the calculated voltage value, E_{Od} is the permissible electric field strength at point O (in air, at the highest operating voltage of power frequency), determined, for example, on the basis of the Paschen empirical law for gaseous dielectrics [13, 14].

The choice of coating length l_s is determined from the condition

$$l_s \geq \sqrt{\frac{2h}{\omega \rho_s \varepsilon_0 \varepsilon}} \ln\left(\frac{2U_{so}}{E_{Kd}} \sqrt{\frac{\omega \rho_{inss} \varepsilon_0 \varepsilon}{h}}\right). \quad (5)$$

The permissible value of the electric field strength E_{Kd} at point K depends on the thickness of the insulation h, the electrical characteristics of the insulation and the semiconductive coating, respectively.

Figure 4 shows the influence of the specific surface resistance of the anti-corona coating ρ_s on the potential distribution over the semiconductive coating (curves 1, 2, and 3) and over the insulation surface (curves 1', 2', and 3') of the stator winding of the high-voltage electric machine on the linear voltage U_l =20 kV along the frontal part of the rods. Curves 1 and 1' correspond to the values of the specific surface resistance of the anti-corona coating ρ_s =5·10⁶ Ω; curves 2 and 2' – ρ_s =5·10⁷ Ω; curves 3 and 3' – ρ_s =5·10⁸ Ω (Fig. 4). Higher values of the specific surface resistance of the semiconductive layers lead to lower voltages on the insulation of the frontal parts of the rods (compare curves 1' and 3' in the region of small l_s values). An increase in the specific surface resistance of the coating causes a decrease in the length of the semiconductive coating.
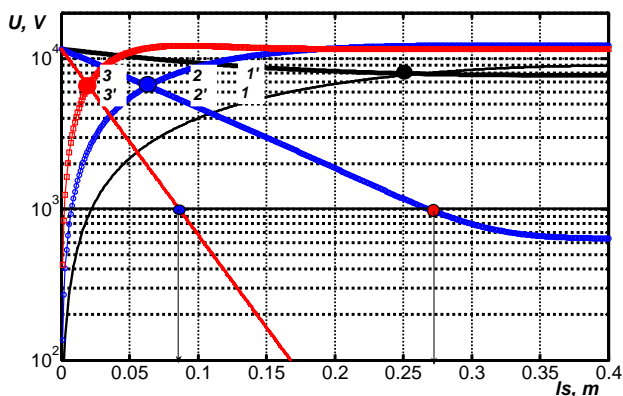

Fig. 4. Potential distribution over the surface of the anti-corona coating (curves 1, 2, and 3) and insulation (curves 1', 2', and 3'), respectively

An increase in ρ_s from 5·10⁶ Ω to 5·10⁸ Ω leads to the intersection of the potential distribution curves over the surface of the anti-corona coating and insulation, i.e. equality of potentials, with significantly smaller, more than 25 times, values of the distance l_s (compare curves 1, 1' and 3, 3' in Fig. 4). The length of the semiconductive coating, which ensures a decrease in potential at point K of no less than 10 times relative to the maximum value at point O, can be taken equal to 27.5 cm and 7 cm for coatings with specific surface resistance values of 5·10⁷ Ω and 5·10⁸ Ω, respectively (see curves 2' and 3' in Fig. 4). In this case, the voltage on the insulation surface does not exceed 1 kV. For a semiconductive coating with a specific surface resistance of 5·10⁶ Ω, the electric field alignment efficiency is extremely low (see curve 1' in Fig. 4).

The correspondence between the calculated (curves 1 and 2) and experimental (points No. 3–6) results of the distribution of the electric potential over the surface of the anti-corona coating along the frontal part is shown in Fig. 5. In the samples of the rod of the hydrogenerator CB 1500/100-12, an anti-corona coating based on a nonlinear

compound (symbols under No. 3, 4) and in the form of a tape (symbols under No. 5, 6) is used. The applied voltage of the rectified frequency corresponds to 10.5 kV (symbols under No. 3, 5 in Fig. 5) and 15.75 kV (symbols under No. 4, 6 in Fig. 5), respectively. The model dependencies of the potential distribution over a semiconductive coating (curves 1 and 2 in Fig. 5) for the stator winding of a high-voltage electric machine with linear voltage of 20 kV correspond to a specific surface resistance of 5·10⁸ Ω (curve 1) and 5·10⁷ Ω (curve 2), respectively.
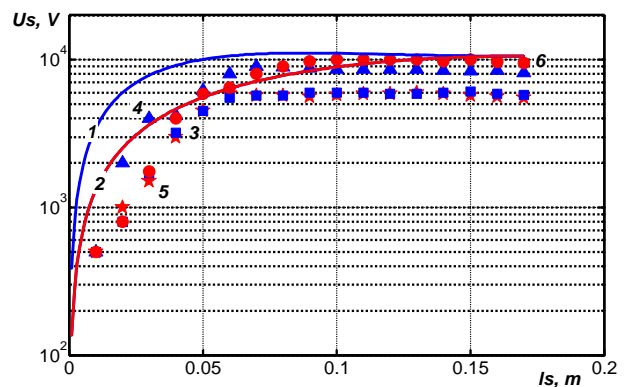
Fig. 5. On the reliability of the results of calculating the potential distribution over the surface of the anti-corona coating along the frontal part of the rods of a high-voltage electric machine

Stability of nonlinear properties of semiconductive anti-corona coatings during the process of electric and thermal aging. The stability verification of the nonlinear properties of the coatings was carried out according to the results of prolonged electrical and thermal aging of specially manufactured samples. Samples of 10 pieces for each type of coating were subjected to electric aging at electric field of 2.5 kV/cm of power frequency for 220 hours, followed by thermal aging at temperature of 175 °C for 100 hours. Electric aging was carried out in two cycles: the first was 60 hours, the second was 160 hours. In the initial state and after each cycle of electric and thermal aging, the measurements of the specific surface resistance were carried out at the rectified test voltage. Figure 6 shows a 3D diagram of the dynamics of changes in the specific surface resistance of nonlinear anti-corona coating samples during aging (ρ_{sa}) relative to the initial, before aging, state (ρ_s) depending on the electric field strength. The numbers in Fig. 6 relate to: anti-corona coating based on a nonlinear compound – 1, 2, 3; anti-corona nonlinear coating in the form of a tape in one layer in the half-overlap – 4, 5, 6 and in two layers in the half-overlap – 7, 8, 9 after the cycles of electrical and thermal aging, respectively.
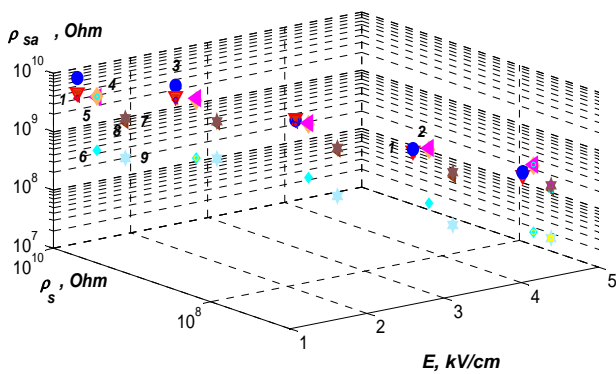
Fig. 6. Dynamics of changes in the specific surface resistance of anti-corona semiconductive coatings during the process of prolonged electrical and thermal aging of samples

For a nonlinear coating in the form of a compound, an increase in the specific surface resistance after aging cycles is observed, which is, probably, due to the additional polymerization of the compound under the influence of electric and thermal effects, which act as initiators of the polymerization process. For a nonlinear coating in the form of a tape after cycles of electric aging, an increase in the specific surface resistance relative to the initial state is also noted. After heat aging, there is a slight decrease in ρ_{si}. It is important that the nonlinearity of the specific surface resistance of the coatings is maintained in the entire range of the electric field strength. After thermal aging, the lower boundary of ρ_{si} corresponds to 10^7 Ω (see Fig. 6, No. 3, 6, 9), which indicates that the regulation of the electric field is sufficient (see Fig. 5, curves 1 and 2).

The stability of the properties of nonlinear anti-corona semiconductive coatings is confirmed by the test results of the samples of the rod of the CB 1500/100-12 hydrogenerator in the initial state and after the combined exposure to an electric field of power frequency voltage of $2.5 \cdot U_l / \sqrt{3}$ and temperature of 120 °C for 260 hours. In the initial state: by the distribution of electric potential along a nonlinear anti-corona coating along the length of the frontal part (see Fig. 3). After complex exposure: by visual absence of glow when applying test voltage exceeding the nominal voltage by 50%; by visual absence of sliding discharges when testing the insulation of the slot part of the rods with test voltage equal to $(3U_l/\sqrt{3})+3)$ kV; by appearance of the coating; by high values of insulation overlap voltage.

Conclusions. A technique is proposed for calculating the distribution of electric potential over the insulation surface along the frontal part of the rods of a high-voltage electric machine using semiconductive coatings that ensure equalization of the electric field strength and elimination of sliding discharges.

The distribution of electric potential over the surface of the anti-corona coating and insulation in the frontal part of the rod of the high-voltage electric machine is obtained with variations in the specific surface resistance of the semiconductive coating.

The proposed technique can be applied to justify the length of the coating in the frontal part of high-voltage electrical machines, depending on the electrophysical characteristics of the coating, electrical insulation and thickness.

The calculated data obtained are consistent with experimental studies of the potential distribution over the surface of the anti-corona semiconductive nonlinear coating along the frontal part of the samples of the hydrogenerator rods for linear voltage of 20 kV.

An experimental verification has been made of the stability of the nonlinear properties of specially made coating samples during long-term electrical and thermal aging, as well as of samples of CB 1500/100-12 hydrogenerator rods in the initial state and after complex exposure to electric field of 26.25 kV of power frequency and temperature of 120 °C for 260 hours.

REFERENCES
1. Grubelnik W., Roberts J., Koerbler B., Marek P. A new approach in insulation systems for rotating machines. *Proceedings Electrical Insulation Conference and Electrical Manufacturing Expo*, 2005. **doi: 10.1109/eeic.2005.1566267**.
2. Dal Mult G., Oldrati A., Zuninow F. New insulation systems for upgrading large turbogenerator driven by gas and steam turbines. *Proceedings of 16th International Conference DISEE*, 2001, pp. 97-100.
3. *Insulating Systems for High-Voltage Rotating Machines*. Available at: https://www.vonroll.com/userfiles/downloads/15357234653101 05/1.02.1_HV%20MOTORS_EN.pdf (accessed 15.08.2018).
4. Ogonkov V.G., Serebryannikov S.V. *Elektroizoliatsionnye materialy i sistemy izoliatsii dlia elektricheskikh mashin. V dvukh knigakh. Kn. 2* [Electrical insulation materials and insulation systems for electrical machines. In 2 books. Book 2]. Moscow, Publishing house MEI, 2012. 304 p. (Rus).
5. Espino-Cortes F.P., Cherney E.A., Jayaram S. Effectiveness of stress grading coatings on form wound stator coil groundwall insulation under fast rise time pulse voltages. *IEEE Transactions on Energy Conversion*, 2005, vol.20, no.4, pp. 844-851. **doi: 10.1109/tec.2005.853745**.
6. Okamoto T., Yoshiyuki I., Kawahara M., Yamada T., Nakamura S. Development of potential grading layer for high voltage rotating machine. *Conference Record of the 2004 IEEE International Symposium on Electrical Insulation*. **doi: 10.1109/elinsl.2004.1380524**.
7. Malamud R.E., Bagaley Yu.V. New anti-corona enamel. *Electrotechnical industry*, 1963, no.7, pp. 11-15. (Rus).
8. Malamud R.E., Bagaley Yu.V. Study of the laws of obtaining nonlinear properties of semiconducting enamels based on silicon carbide powders. *Electricity*, 1976, no.9, pp. 63-66. (Rus).
9. Gegenava A.G. Properties of anti-corona coating of stator windings of high voltage electric machines. *Electricity*, 2002, no.9, pp. 64-66. (Rus).
10. Bezprozvannych G.V., Boyko A.N., Roginskiy A.V. Effect of a dielectric barrier on the electric field distribution in high-voltage composite insulation of electric machines. *Electrical engineering & electromechanics*, 2018, no.6, pp. 63-67. **doi: 10.20998/2074-272X.2018.6.09**.
11. Naboka B.G., Bezprozvannych A.V. *Metodicheskie ukazaniia k resheniiu zadach optimizatsii konstruktsii vysokovol'tnykh izoliatsionnykh promezhutkov po kursu*

«Raschet i konstruirovanie izoliatsii» [Methodical instructions to solving structural optimization of high insulation spaces on the course «Calculation and design of isolation»]. Kharkov, 1988. 30 pp. (Rus).

12. Kuchinsky G.S. *Chastichnye razriady v vysokovol'tnykh konstruktsiiakh* [Partial discharges in high voltage structures]. Leningrad, Energiia Publ., 1979. (Rus).

13. Bezprozvannych A.V. High electric field and partial discharges in bundled cables. *Technical electrodynamics*, 2010, no.1, pp. 23-29. (Rus).

14. Bezprozvannych G.V., Kyessayev A.G., Mirchuk I.A., Roginskiy A.V. Identification of technological defects in high-voltage solid insulation of electrical insulation structures on the characteristics of partial discharges. *Electrical engineering & electromechanics*, 2019, no.4, pp. 53-58. **doi: 10.20998/2074-272X.2019.4.08.**

G.V. Bezprozvannych[1], *Doctor of Technical Science, Professor,*
A.V. Roginskiy[2], *Postgraduate Student,*
[1] National Technical University «Kharkiv Polytechnic Institute»,
2, Kyrpychova Str., Kharkiv, 61002, Ukraine,
phone +380 57 7076010,
e-mail: bezprozvannych@kpi.kharkov.ua
[2] SE Plant Electrotyazhmash,
299, Moskovsky Ave., Kharkiv, 61089, Ukraine,
e-mail: roginskiy.av@gmail.com

V.Yu. Rozov, V.S. Grinchenko, A.V. Yerisov, P.N. Dobrodeyev

EFFICIENT SHIELDING OF THREE-PHASE CABLE LINE MAGNETIC FIELD BY PASSIVE LOOP UNDER LIMITED THERMAL EFFECT ON POWER CABLES

This paper deals with a mitigation of a three-phase cable line magnetic field by a new type of passive shield. We consider a cable line with a flat arrangement of cables. The developed single-loop shield has an asymmetric magnetic coupling with the cable line, due to the use of two different ferromagnetic cores. Its high shielding efficiency is experimentally confirmed. As the developed shield is 0.2÷0.3 m away from the cable line, its thermal effect on the cable line is negligible. As the result, we obtain expressions for the shielding efficiency, parameters of the shield and the cores. References 18, figures 5.
Index terms: **cable line, magnetic field, passive loop, shielding, magnetic core.**

Запропоновано новий тип пасивного екрану для зменшення магнітного поля трифазних кабельних ліній електропередачі із прокладанням кабелів за схемою «у площині». Розроблений одноконтурний екран має несиметричний магнітний зв'язок з кабельною лінією, обумовлений використанням двох різних феромагнітних осердь, та характеризується підтвердженою експериментально високою ефективністю екранування при мінімальному тепловому впливі на кабельну лінію за рахунок відалення від неї екранних кабелів на відстань 0,2÷0,3 м. Отримано співвідношення для визначення ефективності екранування, параметрів екрану та осердь. Бібл. 18, рис. 5.
Ключові слова: **кабельна лінія, магнітне поле, екранування, контурний екран, феромагнітне осердя.**

Предложен новый тип пассивного экрана для уменьшения магнитного поля трехфазных кабельных линий электропередачи с прокладкой кабелей по схеме «в плоскости». Разработанный одноконтурный экран имеет несимметричную магнитную связь с кабельной линией, обусловленную использованием двух разных ферромагнитных сердечников, и характеризуется подтвержденной экспериментально высокой эффективностью экранирования при минимальном тепловом воздействии на кабельную линию за счет удаления от нее экранных кабелей на расстояние 0,2÷0,3 м. Получены соотношения для определения эффективности экранирования, параметров экрана и сердечников. Библ. 18, рис. 5.
Ключевые слова: **кабельная линия, магнитное поле, экранирование, контурный экран, ферромагнитный сердечник.**

Introduction. High-voltage three-phase cable lines are widely used in developed countries for the electric energy transmission in cities, and as well they have good prospects in Ukraine. The fact is that cable lines have several advantages over traditional overhead lines.

Firstly, the width of the protection zone of widely used in cities 110 kV overhead lines is 40 m, while the width of the protection zone of 110 kV cable lines does not exceed 2 m [1]. Therefore, the cable line route does not require the alienation of large and expensive urban land. Secondly, the magnetic field level of overhead lines does not meet modern requirements in terms of environmental safety. According to [1, 2] the power frequency magnetic field should not exceed 0.5 µT in a living space and 10 µT in an urban area. In [3, 4] it was shown experimentally and by numerical simulation, that the magnetic field can exceed the reference level of 0.5 µT in houses located near overhead lines. At the same time, this standard is usually fulfilled for the cable line magnetic field, since the distance between cables is an order less than the distance between overhead line conductors. So the magnetic field decreases faster when moving away from the cable line [5].

However the magnetic field often exceeds the reference level of 10 µT for urban areas directly above the cable line. Modern three-phase cable lines are made of single-core cables with XLPE insulation. The distance between cables is at least 0.5 m [1, 2] in junction zones of 35÷110 kV cable lines. In this case the magnetic field can exceed the allowable level more than 4 times, that forces to take measures to reduce it.

Various types of passive shields [6–12] and systems of active shielding [13, 14] are used to reduce the cable line magnetic field. An advantage of passive shields is the absence of electrical energy sources, used in active systems to create a compensating magnetic field. By the criteria of operating principle, passive shields can be divided into electromagnetic shields [6, 7], magnetic shields [8, 9], and passive loops [10–12]. The most technologically advanced shield is a passive loop type HMCPL with ferromagnetic elements, through the use of which a relatively high efficiency of the magnetic field shielding is achieved [10, 11]. Fig. 1 shows an example of a practical implementation of HMCPL. A significant disadvantage of this type of shield is a proximity of cables of the shield to cables of the cable line, that is necessary to ensure the required shielding efficiency. This leads to the additional heating of the cable line and to the reducing of its capacity.

Fig. 1. Passive loop type HMCPL with ferromagnetic cores and cables of shield arranged on cable line

The goal of the paper is the development of a passive loop to reduce the magnetic field in junction zones of cable lines, that has a minimal thermal effect on the cable line while maintaining high shielding efficiency.

The object of the study is the magnetic field of the cable line with flat arrangement of cables used in junction zones [1, 2].

The main idea of this work is to use a shield made of a passive loop and two ferromagnetic cores to compensate the dipole component of the cable line magnetic field (Fig. 2). The dipole component prevails at reference points, that are distant from the cable line by two cable line width or more. Wherein cables of the shield are 0.2÷0.3 m away from the cable line, that allows to minimize the thermal effect. Ferromagnetic cores enhance the magnetic coupling between the shield and the cable line and ensure high shielding efficiency.

Single-loop shield with ferromagnetic cores and asymmetric magnetic coupling with cable line. It was shown in [15] that the Clarke transformation allows to represent three-phase current as a superposition of three components: α-, β-, and "zero" component. If the power line is symmetrical, the currents of the "zero" component are equal to zero. Based on this, in [16] the magnetic field of a three-phase power line with the conductors arranged in the same plane (horizontal or vertical) is considered as a superposition of the α- and β-component of the magnetic field, which are created by the corresponding current components. Also it was shown that the β-component of the magnetic field is several times greater than the α-component. A qualitative explanation is given in [17]. It is noted that the β-component of the cable line magnetic field is essentially its dipole component.

According to [15], the β-component of currents of the flat cable line flows in a closed contour formed by conductors of two outer cables. The amplitude of the β-component current is $\sqrt{3}/2$ times greater than the amplitude of the conductor current, and the phase shift relative to the conductor current is $\pm\pi/6$ depending on the cable. To compensate the β-component of the cable line magnetic field, sections P_1P_2 and P_3P_4 of the proposed single-loop shield (Fig. 2, *a*) are parallel to the cable line. These sections are distant from the cable line and they are arranged at some height H to minimize the thermal effect of the shield currents on the cable line.

The length of sections P_1P_2 and P_3P_4 is denoted by l. The characteristic dimensions of sections P_4P_1 and P_2P_3 are much smaller than l, so l can be considered as the length of the shield.

Two ferromagnetic cores are installed on outer cables in the section P_4P_1. Each core covers the shield cable and the corresponding cable of the cable line. Each core is splittable to simplify the installation of the proposed single-loop shield (Fig. 2, *b*). Marking letters of cores correspond to cables of the cable line. Each core is characterized by three parameters: effective magnetic permeability μ, cross-section S_{core} and length l_{core} of the core midline.
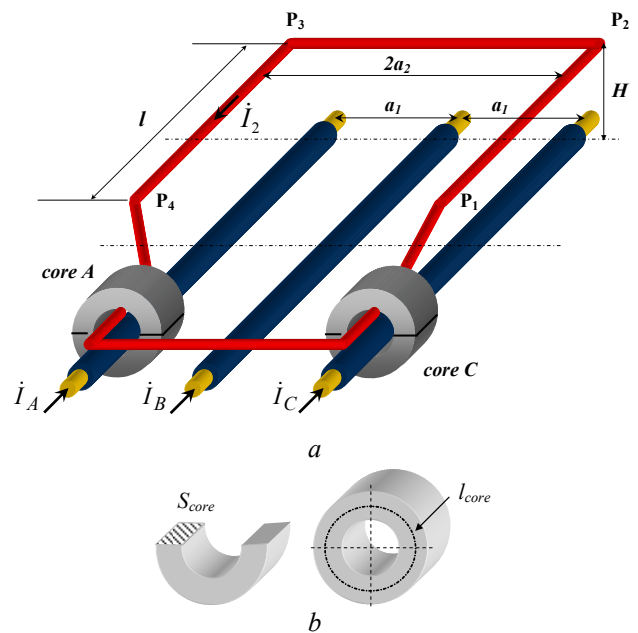
Fig. 2. Design of proposed single-loop shield (*a*) with ferromagnetic cores (*b*)

In general, the presented single-loop shield is characterized by the following parameters:

− the height H of the arrangement above the cable line;

− the width $2a_2$ of the shield (the distance between parallel sections P_1P_2 and P_3P_4);

− the length l of the shield (the length of sections P_1P_2 and P_3P_4);

− conductivity σ and cross-sectional radius r of the shield cables;

− set of parameters μ, S_{core}, l_{core} for each of cores (where the index "*core*" takes values A and C for the core on the left and right cable, respectively).

Single-loop shield efficiency. Since the shield length l is several times greater than $2a_2$ and the characteristic dimension of the section P_4P_1, then we analyze the magnetic field in the two-dimensional approximation. We choose the coordinate system with the abscissa axis located 0.5 m height above the ground level. So the abscissa axis matches the reference plane of the magnetic field normalization. The ordinate axis passes through the central cable of the cable line (Fig. 3). Then among the points from the *x*-axis, the non-shielded magnetic field of the cable line is maximum at the origin.

Fig. 3. Cross-section of cable line (black points) and cables of single-loop shield (gray points)

We consider a three-phase cable line with a positive sequence of conductor currents. Then current phasors in cables of the cable line are the following:

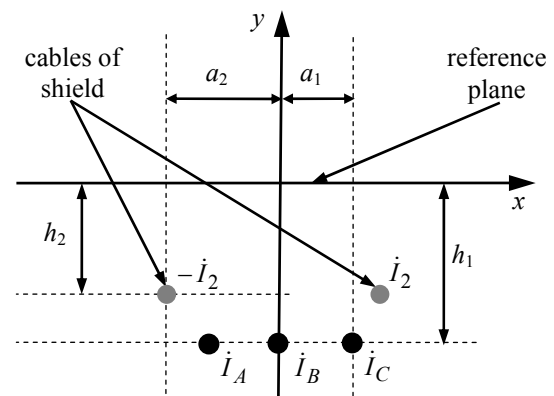$$\dot{I}_A = \sqrt{2}\,I\,e^{-j\cdot\frac{2\pi}{3}}, \quad \dot{I}_B = \sqrt{2}\,I, \quad \dot{I}_C = \sqrt{2}\,I\,e^{j\cdot\frac{2\pi}{3}}, \quad (1)$$

where I is the RMS current in the cable line; j is an imaginary unit.

Applying the Clarke transform to the system of currents (1) and calculating the RMS values of α- and β-components of the cable line magnetic field at the origin, we obtain:

$$B_\alpha = \frac{\mu_0 I}{2\pi h_1}\cdot\frac{a_1^2}{a_1^2+h_1^2}, \quad B_\beta = \sqrt{3}\cdot\frac{\mu_0 I}{2\pi h_1}\cdot\frac{a_1 h_1}{a_1^2+h_1^2}, \quad (2)$$

where h_1 is the distance from the cable line to the reference plane of the magnetic field normalization; a_1 is the distance between adjacent cables of the cable line; $\mu_0 = 4\pi\cdot10^{-7}$ H/m is a vacuum permeability.

Since vectors of the α- and β-components of the cable line magnetic field are mutually perpendicular at the origin, then the magnetic field is equal to the square root of the sum of squares B_α and B_β. We obtain the expression for the maximum shielding factor SF from (2) and the accepted assumption about the compensation of the β-component magnetic field by the single-loop shield:

$$SF = \frac{\sqrt{B_\alpha^2+B_\beta^2}}{B_\alpha} = \sqrt{1+3\cdot\left(\frac{h_1}{a_1}\right)^2}. \quad (3)$$

To reach the maximum shielding factor, the field created by the single-loop shield at the origin must be opposite to the β-component of the cable line magnetic field. This condition gives the expression for the required phasor current in the single-loop shield:

$$\dot{I}_2 = -\dot{I}_1\cdot\frac{a_1}{a_2}\cdot\frac{a_2^2+h_2^2}{a_1^2+h_1^2}, \quad (4)$$

where h_2 is the distance from shield cables to the reference plane; $\dot{I}_1 = j\sqrt{\dfrac{3}{2}}\,I$ is the phasor of the β-component of cable line currents.

Note that the height of the arrangement of the shield above the cable line (outside the core location area) is $H = h_1 - h_2$.

Calculation of parameters of ferromagnetic cores. We use the approach from [18] to analyze the current induced in the single-loop shield. Using complex forms of Ohm's law and Faraday's law of induction, we write down the following relation for a closed contour of the shield:

$$\dot{I}_2\cdot2R = -j\omega\cdot\left(\dot{\Phi}_1+\dot{\Phi}_2+\dot{\Phi}_A+\dot{\Phi}_C\right), \quad (5)$$

where $R = l/\left(\sigma\pi r^2\right)$ is a DC resistance of the section P_1P_2; $\omega = 2\pi\cdot50$ s^{-1} is an angular current frequency; $\dot{\Phi}_1, \dot{\Phi}_2$ are phasors of magnetic flux of cable line currents and shield currents, respectively, through the closed contour of the shield; $\dot{\Phi}_A, \dot{\Phi}_C$ are phasors of magnetic flux running through A and C cores located on the left and on the right cables, respectively.

Expressions for magnetic fluxes have the following form:

$$\dot{\Phi}_1 = M\cdot\dot{I}_1, \quad M = l\cdot\frac{\mu_0}{2\pi}\cdot\ln\frac{(a_1+a_2)^2+(h_1-h_2)^2}{(a_1-a_2)^2+(h_1-h_2)^2},$$

$$\dot{\Phi}_2 = L\cdot\dot{I}_2, \quad L = l\cdot\frac{\mu_0}{\pi}\cdot\left(\frac{1}{4}+\ln\frac{2a_2}{r}\right),$$

$$\dot{\Phi}_A = -L_A\cdot\left(\dot{I}_A-\dot{I}_2\right), \quad L_A = \frac{\mu\mu_0 S_A}{l_A}, \quad (6)$$

$$\dot{\Phi}_C = L_C\cdot\left(\dot{I}_C+\dot{I}_2\right), \quad L_C = \frac{\mu\mu_0 S_C}{l_C}.$$

We substitute (6) into (5) and solve the resulting equation with respect to $\dot{I}_2$. Comparing (4) and the solution, we obtain the following:

$$\begin{cases} L_A - L_C = \dfrac{2\sqrt{3}\,R}{\omega}\cdot\dfrac{a_1}{a_2}\cdot\dfrac{a_2^2+h_2^2}{a_1^2+h_1^2}, \\[3mm] L_A + L_C = -\dfrac{\omega(L_A-L_C)L-2\sqrt{3}\,R\,M}{\omega(L_A-L_C)-2\sqrt{3}\,R}. \end{cases} \quad (7)$$

The expressions (6)–(7) allow to calculate values of inductances introduced by ferromagnetic cores and to determine their parameters. Note that inductances L_A and L_C can take both positive or negative values. The inductance sign determines the mutual orientation of the core and the shield contour (Fig. 4).

In general, values of L_A and L_C are different and can differ by an order or more. This is one of the characteristic features of the proposed shield, that can be classified as a single-loop shield with asymmetric magnetic coupling with a cable line.

Design features of single-loop shield with asymmetric magnetic coupling. There are two competing factors when choosing the height H of the shield above the cable line and the width $2a_2$ of the shield. On the one hand, a decrease of these parameters leads to an increase of the required shield current according to (4). Also it leads to the convergence of the shield and the cable line. Accordingly, the thermal effect on the cable line increases. On the other hand, the analysis of the magnetic field distribution along the x-axis shows that the decrease of H and $2a_2$ allows to ensure the high shielding efficiency of the magnetic field in a wider region.
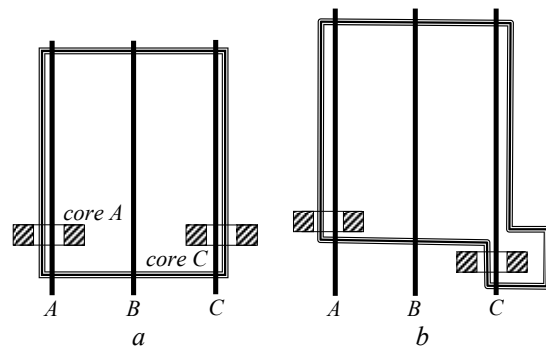

Fig. 4. Mutual orientation of cores and shield contour:
(a) $L_A>0$, $L_C>0$; (b) $L_A>0$, $L_C<0$

The carried out analysis together with the results of the heat problem solution, which are not presented in this paper, allow to recommend $H=0.4 \cdot a_1 \div 0.6 \cdot a_1$, $a_2 = 1.5 \cdot a_1$. In other words, if the distance between adjacent cables of the cable line is taken as a unit of length, then the recommended width of the shield is 3 units, and it is recommended to arrange cables of the shield at a height of $0.4 \div 0.6$ units above the cable line. At these conditions the shield practically does not affect the thermal mode of the cable line.

The technique from [2] can be used to find the length l of the shield (Fig. 2).

The required inductances L_A and L_C of ferromagnetic cores used in the shield design are calculated using (7).

If L_A and L_C are positive, then cores are installed as shown in Fig. 4, a. If one of the values is negative, then the orientation of the shield current direction relative to the core should be reversed. In this case, the mutual arrangement of cores and the shield contour is shown in Fig. 4, b.

The magnetic permeability, the cross-sectional area, and the length of the midline of each core are chosen according to (6) based on the absolute value of its inductance.

A full-scale model of the proposed single-loop shield with asymmetric magnetic coupling was experimentally studied. An experimental setup contains a 10 m long physical model of a three-phase cable line (Fig. 5). The reference plane of the magnetic field normalization is 2 m height above the cable line, the distance between adjacent cables is 0.5 m. The loop of the shield is made of a single-core copper cable. Cores are made of transformer steel. The experiment was carried out when the width of the shield is 1.5 m and the height of shield arrangement above the cable line is 0.3 m. The experimentally confirmed shielding efficiency of the magnetic field is 7.
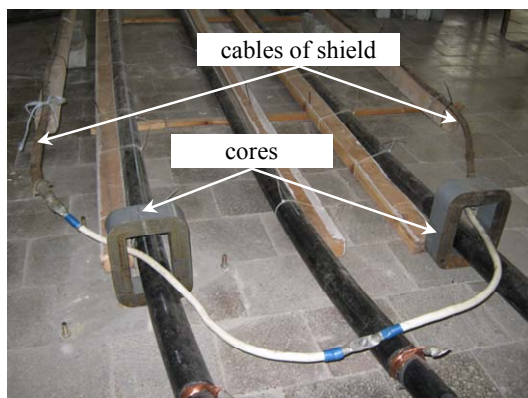

Fig. 5. Experimental setup for studying efficiency of shielding of cable line magnetic field by single-loop shield with asymmetric magnetic coupling

Conclusions.

1. We propose a single-loop shield with ferromagnetic cores and asymmetric magnetic coupling. It ensures high shielding efficiency of the magnetic field, and it is distant from the cable line by a height equal to $0.4 \div 0.6$ of the distance between adjacent power cables. This allows to minimize the thermal effect on the cable line in comparison with known passive loops having similar shielding efficiency.

2. We theoretically justified and experimentally confirmed that the shielding factor is equal to 7, when the distance between adjacent cables of the cable line is 0.5 m (typical for junction zones), the recommended width of the shield is 1.5 m, the shield is 0.3 m height above the cable line, and the reference plane of the magnetic field normalization is 2 m height above the cable line.

REFERENCES
1. Electrical installation regulations. 5th ed. Kharkiv, Minenergovugillya of Ukraine, 2014. 793 p. (Ukr).
2. SOU-N MEV 40.1-37471933-49:2011.2. Design of cable lines with voltage up to 330 kV. Guidance. Kyiv, Minenergovugillya of Ukraine Publ., 2017. 139 p. (Ukr).
3. Pelevin D.Ye. Screening magnetic fields of the power frequency by the walls of houses. *Electrical Engineering & Electromechanics*, 2015, no.4, pp. 53-55. (Rus). **doi: 10.20998/2074-272X.2015.4.10**.
4. Rozov V., Grinchenko V. Simulation and analysis of power frequency electromagnetic field in buildings closed to overhead lines. *2017 IEEE 1st Ukraine Conference on Electrical and Computer Engineering*, pp. 500-503. **doi: 10.1109/UKRCON.2017.8100538**.
5. Rozov V.Yu., Reutskyi S.Yu., Pelevin D.Ye., Yakovenko V.N. The research of magnetic field of high-voltage ac transmissions lines. *Technical Electrodynamics*, 2012, no.1, pp. 3-9.
6. del-Pino-López J.C., Cruz-Romero P., Serrano-Iribarnegaray L., Martínez-Román J. Magnetic field shielding optimization in underground power cable duct banks. *Electric Power Systems Research*, 2014, vol.114, pp. 21-27. **doi: 10.1016/j.epsr.2014.04.001**.
7. Cardelli E., Faba A., Pirani A. Nonferromagnetic open shields at industrial frequency rate. *IEEE Transactions on Magnetics*, 2010, vol.46, no.3, pp. 889-898. **doi: 10.1109/TMAG.2009.2031110**.
8. De Wulf M., Wouters P., Sergeant P., Dupré L., Hoferlin E., Jacobs S., Harlet P. Electromagnetic shielding of high-voltage cables. *Journal of Magnetism and Magnetic Materials*, 2007, no.316, pp. 908-911. **doi: 10.1016/j.jmmm.2007.03.137**.
9. Ruiz J.R.R., Morera X.A. Magnetic shields for underground power lines. *Renewable Energy & Power Quality Journal*, 2004, vol.1, no.2, pp. 137-140. **doi: 10.24084/repqj02.230**.
10. Canova A., Giaccone L. Magnetic mitigation of HV cable junction zone. *8th International Conference on Insulated Power Cables*, 2011, Paper B.1.6.
11. Canova A., Bavastro D., Freschi F., Giaccone L., Repetto M. Magnetic shielding solutions for the junction zone of high voltage underground power lines. *Electric Power Systems Research*, 2012, vol.89, pp. 109-115. **doi: 10.1016/j.epsr.2012.03.003**.
12. del-Pino-López J.C., Cruz-Romero P. The effectiveness of compensated passive loops for mitigating underground power cable magnetic fields. *IEEE Transactions on Power Delivery*, 2011, vol.26, no.2, pp. 674-683. **doi: 10.1109/TPWRD.2009.2039150**.
13. Kuznetsov B.I., Nikitina T.B., Bovdui I.V. High voltage power lines magnetic field system of active shielding with compensation coil different spatial arrangement. *Electrical engineering & electromechanics*, 2019, no.4, pp. 17-25. **doi: 10.20998/2074-272X.2019.4.03**.
14. Bravo-Rodríguez J.C., del-Pino-López J.C., Cruz-Romero P. A survey on optimization techniques applied to magnetic field

mitigation in power systems. *Energies*, 2019, vol.12, no.7, p. 1332. **doi: 10.3390/en12071332**.

15. Duesterhoeft W.C., Schulz M.W., Clarke E. Determination of instantaneous currents and voltages by means of alpha, beta, and zero components. *Transactions of the American Institute of Electrical Engineers*, 1951, vol.70, no.2, pp. 1248-1255. **doi: 10.1109/T-AIEE.1951.5060554**.

16. Walling R.A., Paserba J.J., Burns C.W. Series-capacitor compensated shield scheme for enhanced mitigation of transmission line magnetic fields. *IEEE Transactions on Power Delivery*, 1993, vol.8, no.1, pp. 461-469. **doi: 10.1109/61.180369**.

17. Rozov V., Grinchenko V., Tkachenko O., Yerisov A. Analytical calculation of magnetic field shielding factor for cable line with two-point bonded shields. *IEEE 17th International Conference on Mathematical Methods in Electromagnetic Theory*, 2018, pp. 358-361. **doi: 10.1109/MMET.2018.8460425**.

18. Rozov V.Yu., Grinchenko V.S., Tkachenko A.O. Calculation of magnetic field of three-phase cable lines with two-point bonded cable shields covered by ferromagnetic cores. *Electrical Engineering & Electromechanics*, 2015, no.5, pp. 44-47. (Rus). **doi: 10.20998/2074-272X.2017.5.06**.

V.Yu. Rozov, Dr.Sc., Corr. Member of the National Academy of Sciences of Ukraine,
V.S. Grinchenko, Ph.D.,
A.V. Yerisov,
P.N. Dobrodeyev, Ph.D.,
[1] State Institution "Institute of Technical Problems of Magnetism of the National Academy of Sciences of Ukraine",
19, Industrialna Str., Kharkiv, 61106, Ukraine,
e-mail: Rozov@nas.gov.ua

A. Hinda, M. Khiat, Z. Boudjema

FUZZY SECOND ORDER SLIDING MODE CONTROL
OF A UNIFIED POWER FLOW CONTROLLER

Purpose. *This paper presents an advanced control scheme based on fuzzy logic and second order sliding mode of a unified power flow controller. This controller offers advantages in terms of static and dynamic operation of the power system such as the control law is synthesized using three types of controllers: proportional integral , and sliding mode controller and Fuzzy logic second order sliding mode controller. Their respective performances are compared in terms of reference tracking, sensitivity to perturbations and robustness. We have to study the problem of controlling power in electric system by UPFC. The simulation results show the effectiveness of the proposed method especially in chattering-free behavior, response to sudden load variations and robustness. All the simulations for the above work have been carried out using MATLAB / Simulink. Various simulations have given very satisfactory results and we have successfully improved the real and reactive power flows on a transmission line as well as to regulate voltage at the bus where it is connected, the studies and illustrate the effectiveness and capability of UPFC in improving power.* References 25, tables 2, figures 10.*
Key words: **UPFC, FACTS, PI, second order sliding mode, fuzzy logic.**

Цель. *В настоящей статье представлена усовершенствованная схема управления, основанная на нечеткой логике и режиме скольжения второго порядка унифицированного контроллера потока мощности. Данный контроллер обладает преимуществами с точки зрения статической и динамической работы энергосистемы, например, закон управления синтезируется с использованием трех типов контроллеров: пропорционально-интегрального, контроллера скользящего режима и контроллера скользящего режима нечеткой логики второго порядка. Их соответствующие характеристики сравниваются с точки зрения отслеживания эталонов, чувствительности к возмущениям и надежности. Необходимо изучить проблему управления мощностью в энергосистеме с помощью унифицированного контроллера потока мощности (UPFC). Результаты моделирования показывают эффективность предложенного метода, особенно в отношении отсутствия вибрации, реакции на внезапные изменения нагрузки и устойчивости. Все расчеты для вышеуказанной работы были выполнены с использованием MATLAB/Simulink. Различные расчетные исследования дали весьма удовлетворительные результаты, и мы успешно улучшили потоки реальной и реактивной мощности на линии электропередачи, а также регулирование напряжения на шине, к которой она подключена, что позволяет изучить и проиллюстрировать эффективность и возможности UPFC для увеличения мощности.* Библ. 25, табл. 2, рис. 10.*
Ключевые слова: **унифицированный контроллер потока мощности (UPFC), гибкая система передачи переменного тока (FACTS), PI (пропорционально-интегральный) контроллер, скользящий режим второго порядка, нечеткая логика.**

Introduction. In recent years, the electrical power distribution system are suffering from significant power flow quality (PQ) problems, which are characterized by low power factor, poor voltage profile, voltage stability, load unbalancing, and supply interruptions. These power quality issues have attracted attention to the researchers both in academic and industry. As a result, many power quality standards were proposed in [1]. By the reason of these power quality issues, the use of flexible AC transmission system (FACTS) controllers in power system has been of worldwide interest for increasing the power transfer capability and enhancing power system controllability and stability due to their speed and flexibility. In addition, converter based FACTS controllers are capable of independently controlling both active and reactive power flow in the power system [2].

Unified power flow controller (UPFC) is the member of FACTS device. It is the most versatile and powerful FACTS device [3]. The fundamental theory of UPFC is that, the phase angle affects flow of real power and the magnitude of voltage affects flow of reactive power [4, 5].

This device consists of two other FACTS devices: the Static Synchronous Series Compensator (SSSC) and the Static Synchronous Compensator (STATCOM), the SSSC injects a an almost sinusoidal voltage, of variable magnitude in series with the system voltage provides the most cost effective solution to mitigate voltage sags by improving power quality level that is required by customer and the STATCOM connected by a common DC link capacitor. It can simultaneously perform the

function of transmission line real/reactive power flow control in addition to UPFC bus voltage/shunt reactive power control [6].

Though UPFC implies many advantages, but its controller design still being a matter of challenge since it is a multi-variable controller. In literature, a lot of works have been presented with diverse control diagrams of UPFC for various power system applications. Recently, the sliding mode control (SMC) method has been widely used for robust control of nonlinear systems. Several papers have been published based on SMC of UPFC [7-9]. Nevertheless, the deficiency of this type of control, which is the chattering phenomenon caused by the discontinuous control action. To resolve this problem, several modifications to the usual control law have been proposed, the most popular being the boundary layer approach [10, 11].

Fuzzy logic is a technology based on engineering experience and observations. In fuzzy logic, an exact mathematical model is not necessary because linguistic variables are used to define system behavior rapidly. One way to improve sliding mode controller performance is to combine it with fuzzy logic to form a fuzzy sliding mode controller. The design of a sliding mode controller incorporating fuzzy control helps in achieving reduced chattering, simple rule base, and robustness against disturbances and nonlinearities.

This paper discusses the capability of UPFC on controlling independently the active and reactive power in

the power transmission line and the improvement of the transient and dynamic stability of the power system by the UPFC are examined. Active and reactive powers are controlled using three types of controllers: Proportional-Integral (PI) and SMC and Fuzzy logic second order sliding mode controller (FLSOSMC). Their performances are compared in terms of reference tracking, sensitivity to perturbations and robustness.

Structure of the UPFC. For many years, UPFC is considered as the most versatile of the FACTS device one that can be used to enhance steady state stability, dynamic stability and transient stability, which combines the good features of STATCOM and SSSC. Fig. 1 shows the basic structure of UPFC which is consists of two voltage sourced converters (VSC) and used to provide galvanic isolation and adjust the voltage levels in the supply system. It is composed of two inverters with PWM control (Pulse Width Modulation), which are operated from a DC link provided by a dc storage capacitor. One is connected in parallel and the other in series with the transmission line [12]. The detailed structure and the functionality of the UPFC can be found in [13].
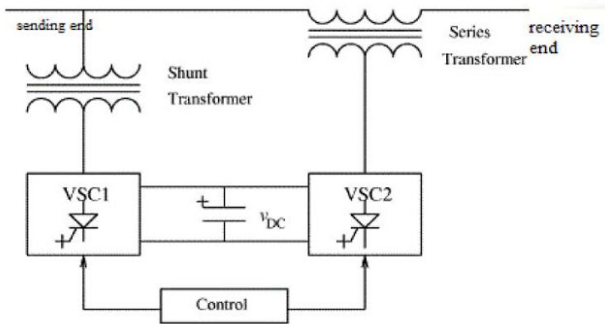

Fig. 1. Basic structure of the UPFC.

The modeling of the UPFC. Figure 2 represents the simplified model circuit of the UPFC.
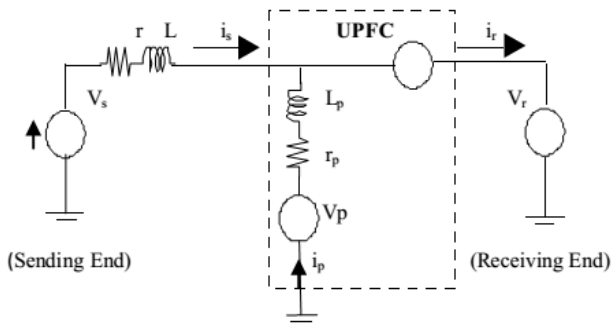

Fig. 2. Equivalent circuit of the UPFC

Applying Kirchhoff law on equivalent circuit shown in Fig. 2, the dynamic equations of the UPFC series branch is

$$\frac{d}{dt}\begin{bmatrix} I_{sa} \\ I_{sb} \\ I_{sc} \end{bmatrix} = \begin{bmatrix} -r/L & 0 & 0 \\ 0 & -r/L & 0 \\ 0 & 0 & -r/L \end{bmatrix}\begin{bmatrix} I_{sa} \\ I_{sb} \\ I_{sc} \end{bmatrix} + $$
$$+ \begin{bmatrix} 1/L & 0 & 0 \\ 0 & 1/L & 0 \\ 0 & 0 & 1/L \end{bmatrix}\begin{bmatrix} V_{sa} - V_{ca} - V_{ra} \\ V_{sb} - V_{cb} - V_{rb} \\ V_{sc} - V_{cc} - V_{rc} \end{bmatrix}. \quad (1)$$

Using Park transformation, the equations (1) will be written as

$$\frac{d}{dt}\begin{bmatrix} I_{sd} \\ I_{sq} \end{bmatrix} = \begin{bmatrix} -r/L & +\omega \\ -\omega & -r/L \end{bmatrix}\begin{bmatrix} I_{sd} \\ I_{sq} \end{bmatrix} + $$
$$+ \begin{bmatrix} 1/L & 0 \\ 0 & 1/L \end{bmatrix}\begin{bmatrix} V_{sd} - V_{cd} - V_{rd} \\ V_{sq} - V_{cq} - V_{rq} \end{bmatrix}. \quad (2)$$

The modeling of the UPFC shunt branch. The complete mathematical model of the UPFC shunt is given similarly by the following matrix

$$\frac{d}{dt}\begin{bmatrix} I_{pa} \\ I_{pb} \\ I_{pc} \end{bmatrix} = \begin{bmatrix} -r_p/L_p & 0 & 0 \\ 0 & -r_p/L_p & 0 \\ 0 & 0 & -r_p/L_p \end{bmatrix}\begin{bmatrix} I_{pa} \\ I_{pb} \\ I_{pc} \end{bmatrix} + $$
$$+ \begin{bmatrix} 1/L_p & 0 & 0 \\ 0 & 1/L_p & 0 \\ 0 & 0 & 1/L_p \end{bmatrix}\begin{bmatrix} V_{pa} - V_{ca} - V_{ra} \\ V_{pb} - V_{cb} - V_{rb} \\ V_{pc} - V_{cc} - V_{rc} \end{bmatrix}. \quad (3)$$

Since the system is assumed to be a balanced one, it can be transformed into a synchronous d-q-o frame by applying Park's transformation. The matrix form (3) is given as follows

$$\frac{d}{dt}\begin{bmatrix} I_{pd} \\ I_{pq} \end{bmatrix} = \begin{bmatrix} -r_p/L_p & +\omega \\ -\omega & -r_p/L_p \end{bmatrix}\begin{bmatrix} I_{pd} \\ I_{pq} \end{bmatrix} + $$
$$+ \begin{bmatrix} 1/L_p & 0 \\ 0 & 1/L_p \end{bmatrix}\begin{bmatrix} V_{pd} - V_{cd} - V_{rd} \\ V_{pq} - V_{cq} - V_{rq} \end{bmatrix}. \quad (4)$$

The modeling of the UPFC continues branch. For the DC-side circuit, based on the power balance equation in the output and input of UPFC, The net real power exchanged by both the converters through DC side should be zero to keep the capacitor voltage constant [14]. The DC voltage V_{dc} dynamics across the capacitor is given by the following equation

$$\frac{dV_{dc}}{dt} = \frac{1}{CV_{dc}}\left(P_e - P_{ep}\right), \quad (5)$$

where P_e – active power absorbed of the AC system

$$P_e = v_{ca} \cdot i_{sa} + v_{cb} \cdot i_{sb} + v_{cc} \cdot i_{sc};$$

where P_{ep} – active power injected by the shunt inverter AC system

$$P_{ep} = v_{pa} \cdot i_{pa} + v_{pb} \cdot i_{pb} + v_{pc} \cdot i_{pc}.$$

By performing Park transformation, the DC voltage V_{dc} dynamics across the capacitor can be described by the following equations

$$\frac{dV_{dc}}{dt} = \frac{1}{CV_{dc}}\left(v_{pd} \cdot I_{pd} + v_{pq} \cdot I_{pq} - v_{cd} \cdot I_{rd} - v_{cq} \cdot I_{rq}\right). \quad (6)$$

Control of the parallel converter. The ordinary working principle of the parallel compensation of STATCOM is described as follows: active power control which means stabling the capacitor voltage of the DC side; reactive power control which means stabling the terminal voltage [15]. According to the system of equations (2) the control strategy of parallel compensation (STATCOM) is decoupling of the two current loops control, to reduce the interaction between the active and reactive power. The control block diagram is shown in Fig. 3.
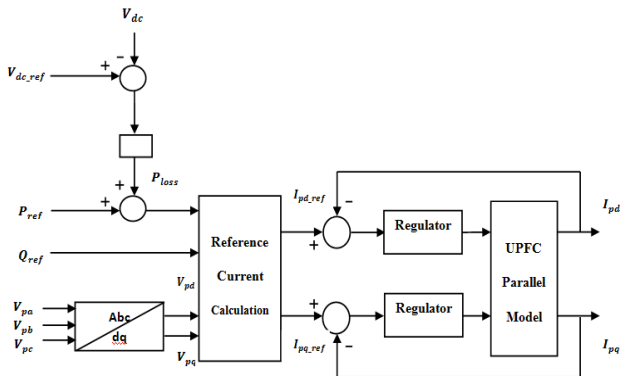
Fig. 3. Control system of shunt part

Control of the series converter. The SSSC regulate the active and reactive power flow on the transmission line where the UPFC is installed by injection voltage of which the amplitude and the phase both can be adjusted. The control strategy of the series compensator is decoupling of the two current loops control. The diagram of control circuits of SSSC is given in the Fig. 4.
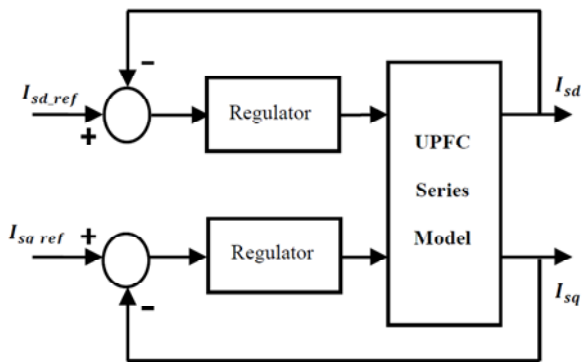

Fig. 4. Control system of series part

In this section, we have chosen to compare the performances of the UPFC with two different controllers: PI and SMC.

PI controller. This controller is simple to elaborate. Fig. 5 shows the block diagram of the system implemented with this controller. The terms k_p and k_i represent respectively the proportional and integral gains.
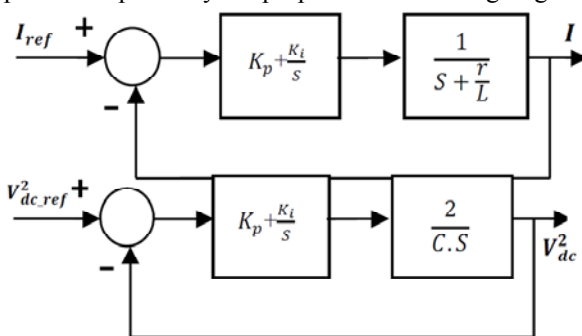

Fig. 5. System with PI controller

The regulator terms are calculated with a pole compensation method. The time response of the controlled system will be fixed at $\tau = 5$ ms. This value is sufficient for our application and a lower value might involve transients with important overshoots. The calculated terms are represented in Table 1.

	Controller series part	Controller shunt part	Controller continues branch
K_p	$1/\tau$	$1/\tau$	$C \cdot \omega^2/2$
K_i	$\left(\dfrac{R}{L}\right)K_p$	$\left(\dfrac{r_p}{L_p}\right)K_p$	$C \cdot \xi \omega$

It is important to specify that the pole compensation is not the only method to calculate a PI regulator but it is simple to elaborate with a first order transfer-function and it is sufficient in our case to compare with other regulators.

Sliding mode controller. Sliding mode control is one of the effective nonlinear robust control approaches since it provides system dynamics with an invariance property to uncertainties once the system dynamics are controlled in the sliding mode [16-18]. The main feature of Sliding mode controller (SMC) is that it only needs to drive the error to a switching surface it consists of three parts Fig. 6.
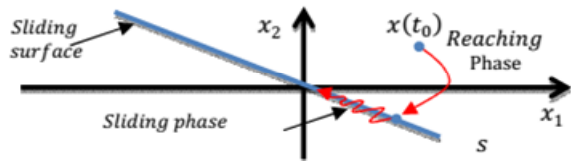
Fig. 6. Phase portrait of sliding mode control

The switching surface choice. The design of the control system will be demonstrated for a nonlinear system presented in the canonical form [17]:

$$\begin{cases} \dot{x} = f(x,t) + B(x,t) \cdot V(x,t), \\ x \in Rn, V \in Rm, ran(B(x,t)) = m, \end{cases} \quad (7)$$

where $f(x, t)$, $B(x, t)$ – two continuous and uncertain non-linear functions, supposed limited.

We take the general equation to determine the sliding surface proposed by J.J. Slotine [20, 21] given by

$$S(X) = \left(\frac{d}{dt} + \lambda\right)^{n-1} e; \quad e = x^* - x, \quad (8)$$

where e – error on the signal to be adjusted; λ – a positive coefficient; n – system order; x^* – desired signal; x – state variable of the control signal.

Convergence condition. The convergence condition is defined by the Lyapunov equation [14]; it makes the surface attractive and invariant :

$$S \cdot \dot{S} < 0. \quad (9)$$

Control calculation. The control algorithm is defined by the relation [17]:

$$V^{com} = V^{eq} + V^n, \quad (10)$$

where V^{com} is the control vector, V^{eq} is the equivalent control vector, V^n is the correction factor and must be calculated so that the stability conditions for the selected control are satisfied

$$V^n = Ksat(S(X)/\delta), \quad (11)$$

$$sat(S(X)/\delta) = \begin{cases} sign(S) & if \quad |S| > \delta; \\ S/\delta & if \quad |S| < \delta; \end{cases} \quad (12)$$

where $sat(S(x)/\delta)$ is the proposed saturation function, δ is the boundary layer thickness.

In our study, the errors between the references and measured I_d and I_q currents have been chosen as sliding mode surfaces, so we can write the following expression

$$\begin{cases} s_d = I_{sd\_ref} - I_{sd}; \\ s_q = I_{sq\_ref} - I_{sq}. \end{cases} \quad (13)$$

The first order derivate of (8) gives

$$\begin{cases} \dot{s}_d = \dot{I}_{sd\_ref} - \dot{I}_{sd}; \\ \dot{s}_q = \dot{I}_{sq\_ref} - \dot{I}_{sq}. \end{cases} \quad (14)$$

Taking its derivative and replacing it in the current $\dot{I}_{sd}$ and $\dot{I}_{sq}$ expression (2) we get

$$\begin{cases} \dot{s}_d = \dot{I}_{sd\_ref} - \omega I_{sq} + \dfrac{r}{L} I_{sd} - \dfrac{1}{L}\left(v_{sd} - v_{cd} - v_{rd}\right); \\ \dot{s}_q = \dot{I}_{sq\_ref} + \omega I_{sd} + \dfrac{r}{L} I_{sq} - \dfrac{1}{L}\left(v_{sq} - v_{cq} - v_{rq}\right) \end{cases} \quad (15)$$

Replacing the expression of v_{cd} and v_{cq} in (10) by their expressions given in (15), one obtains

$$\begin{cases} \dot{s}_d = \dot{I}_{sd\_ref} - \omega I_{sq} + \dfrac{r}{L} I_{sd} - \dfrac{1}{L}\left(v_{sd} - \left(v_{cd}^n + v_{cd}^{eq}\right) - v_{rd}\right); \\ \dot{s}_q = \dot{I}_{sq\_ref} + \omega I_{sd} + \dfrac{r}{L} I_{sq} - \dfrac{1}{L}\left(v_{sq} - \left(v_{cq}^n + v_{cq}^{eq}\right) - v_{rq}\right) \end{cases} \quad (16)$$

I_{qr} will be the component of the control vector used to constraint the system to converge to S=0. The control vector v^{eq} is obtain by imposing $\dot{S}=0$ so the equivalent control components are given by the following relation

$$\begin{cases} v_{cd}^{eq} = -L\dot{I}_{sd\_ref} + L\omega I_{sq} - rI_{sd} + v_{sd} - v_{rd}; \\ v_{cq}^{eq} = -L\dot{I}_{sq\_ref} - L\omega I_{sd} - rI_{sq} + v_{sq} - v_{rq}. \end{cases} \quad (17)$$

Using the same procedures as for part shunt we get the following expression:

$$\begin{cases} v_{cd}^{eq} = -L_p \dot{I}_{pd\_ref} + L_p \omega I_{pq} - r_p I_{pd} + v_{pd} - v_{rd}; \\ v_{cq}^{eq} = -L_p \dot{I}_{pq\_ref} - L_p \omega I_{pd} - r_p I_{pq} + v_{pq} - v_{rq}. \end{cases} \quad (18)$$

To obtain good performances, dynamic an commutation around the surface, the control vector is imposed as follows [19]

$$v = v^{eq} + K \cdot \text{sign}(S). \quad (19)$$

The sliding mode will exist only if the following condition is met

$$S \cdot \dot{S} < 0. \quad (20)$$

Fuzzy logic second order sliding mode controller (FLSOSMC). The sliding mode control is a widely studied control scheme that provides robustness to certain disturbances and system uncertainties [7, 9] Nevertheless, a few drawbacks arise in its practical implementation, such as chattering phenomenon Such chattering has many negative effects in real world applications since it may damage the control actuator and excite the undesirable unmodeled dynamics In order to reduce the effects of these problems, second order sliding mode seems to be a very attractive solution [22].

This method generalizes the essential sliding mode idea by acting on the higher order time derivatives of the sliding manifold, instead of influencing the first time derivative as it is the case in SMC, therefore reducing chattering and while preserving SMC advantages [23].

In order to ensure the active and reactive power convergence to their reference, a second order sliding mode control (SOSMC) is used. Considering the sliding mode surface given by (15), the following expression can be written:

$$\begin{cases} \dot{s}_d = \dot{I}_{sd\_ref} - \omega I_{sq} + \dfrac{r}{L} I_{sd} - \dfrac{1}{l}\left(v_{sd} - v_{cd} - v_{rd}\right); \\ \ddot{S}_d = Y_1(t,x) + \varLambda_1(t,x)v_{cd}, \end{cases} \quad (21)$$

and

$$\begin{cases} \dot{s}_q = \dot{I}_{sq\_ref} - \omega I_{sd} + \dfrac{r}{L} I_{sq} - \dfrac{1}{l}\left(v_{sq} - v_{cq} - v_{rq}\right); \\ \ddot{S}_q = Y_2(t,x) + \varLambda_2(t,x)v_{cq}, \end{cases} \quad (22)$$

where $Y_1(t,x)$, $Y_2(t,x)$, $\varLambda_1(t,x)$ and $\varLambda_2(t,x)$ – uncertain functions which satisfy

$$\begin{cases} Y_1 > 0, \ |Y_1| > \lambda_1, \ 0 < K_{m1} < \varLambda_2 < K_{M1}; \\ Y_2 > 0, \ |Y_2| > \lambda_2, \ 0 < K_{m2} < \varLambda_2 < K_{M2}. \end{cases}$$

Basing on the super twisting algorithm introduced by Levant in [24], the proposed high order sliding mode controller contains two parts [25]

$$v_{cd} = v_1 + v_2. \quad (23)$$

With

$$\dot{v}_1 = -k_1 \cdot \text{sign}(S_d);$$
$$v_2 = -l \cdot |S_1|^\gamma \cdot \text{sign}(S_d); \quad (24)$$
$$v_{cq} = w_1 + w_2$$

and with

$$\dot{w}_1 = -k_2 \cdot \text{sign}(S_q);$$
$$w_2 = -l \cdot |S_q|^\gamma \cdot \text{sign}(S_q).$$

In order to ensure the convergence of the sliding manifolds to zero in finite time, the gains can be chosen as follows [25]

$$\begin{cases} k_i > \dfrac{\lambda_i}{K_{mi}} \\ l_i^2 \geq \dfrac{4\lambda_i}{K_{mi}^2} \cdot \dfrac{K_{Mi}(k_i + \lambda_i)}{K_{mi}(k_i - \lambda_i)}; \quad i = 1,2; \\ 0 < \gamma \leq 0.5. \end{cases}$$

In order to improve the SOSMC of the UPFC and more and more decrease the adverse effect caused by the *sign* function, we propose in this paper to use the (FLSOSMC).

For the proposed FLSOSMC, the universes of discourses are first partitioned into the seven linguistic variables NB, NM, NS, EZ, PS, PM, PB, triangular and trapezoidal membership functions are chosen to represent the linguistic variables for the inputs and outputs of the controllers.

The fuzzy labels used in this study are negative big (NB), negative medium (NM), negative small (NS), equal zero (EZ), positive small (PS), positive medium (PM) and positive big (PB).

These choices are described in Fig. 7.
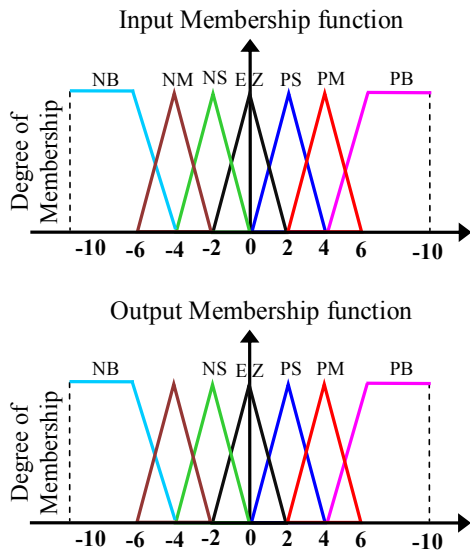
Fig. 7. Fuzzy sets and its memberships functions

Table 2
The parameters of the laboratory UPFC model

Parameter name	Symbol	Value	Unit
Network voltage	V_r	220	V
Voltage of the receiver	V_s	220	V
DC voltage	V_{dc}	280	V
Network frequency	f	50	HZ
The capacity of the common circuit DC	C	2	mF
Inductance 1	L	1.125	mH
Resistance 1	r	100	Ω
Inductance 2	L_p	1.125	mH
Resistance 2	r_p	100	Ω

Simulations and results. In this section, simulations are realized with a UPFC coupled to a 220V/50Hz grid. The system parameters are given in Table 2. The whole system is simulated using the Matlab/Simulink software.

In the objective to evaluate the performances of the controllers, three categories of tests have been realized: pursuit test, sensitivity to introducing perturbation and robustness facing variation of the reactance XL.

Pursuit test. This test has for goal the study of the three controllers (PI, SMC and FLSOSMC) behavior in reference tracking. The simulation results are presented in Fig. 8. As it's shown by this figure, for the 3 controllers, the active and reactive power track almost perfectly their references but with an important response time for the PI controller compared to the SMC and FLSOSMC. Therefore it can be considered that the two types of sliding mode controllers have a very good performance for this test.

Fig. 8. Reference tracking test

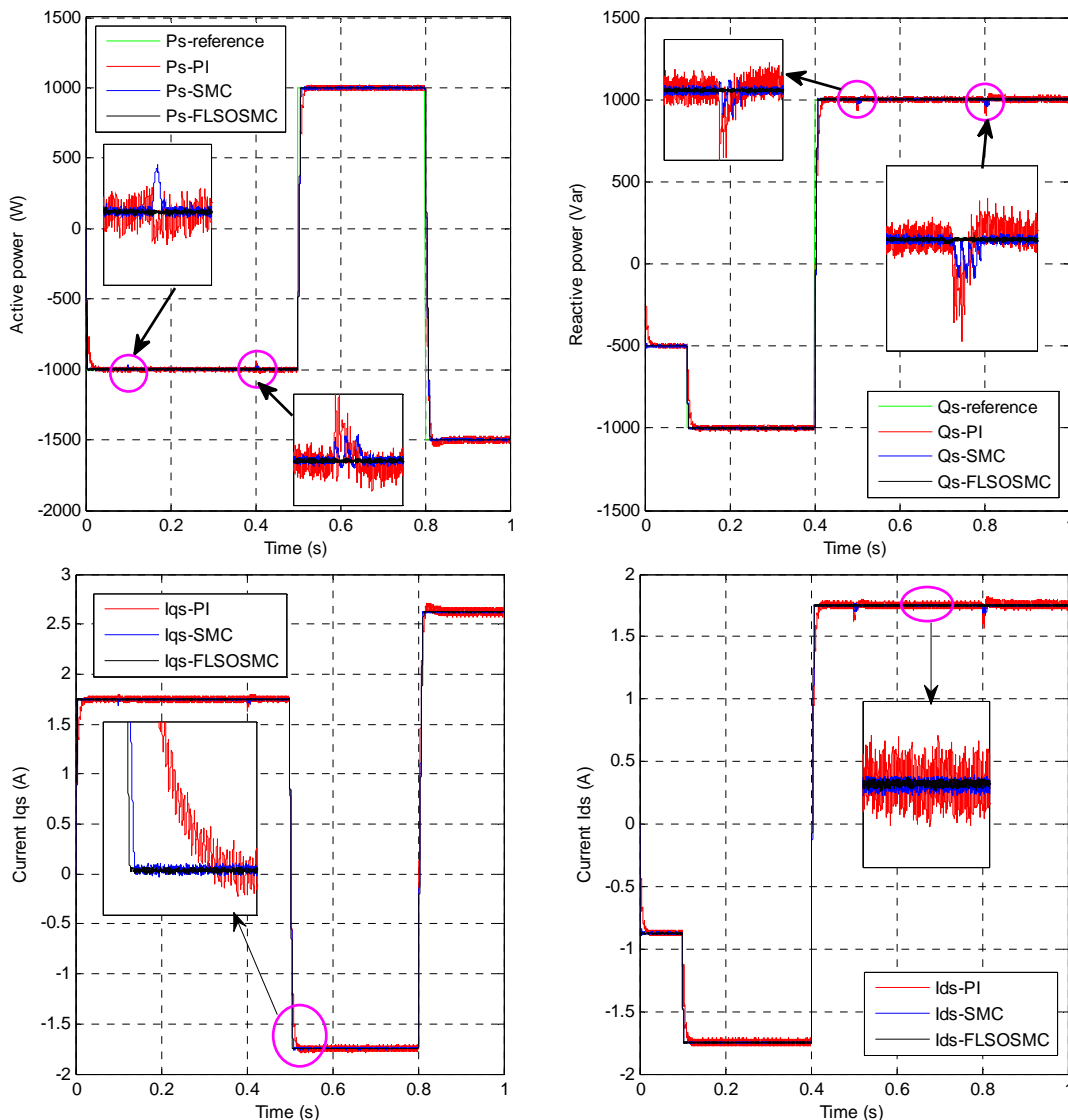**Robustness.** We tested the robustness of the used controllers for a variation of the reactance XL. The results presented in Fig. 9 show that reactance variation presents a clear effect on the active and reactive powers of the two used controllers and that the effect appears more significant for PI controller than that with the SMC and FLSOSMC. Thus it can be concluded that these last are robust against this parameter variation.
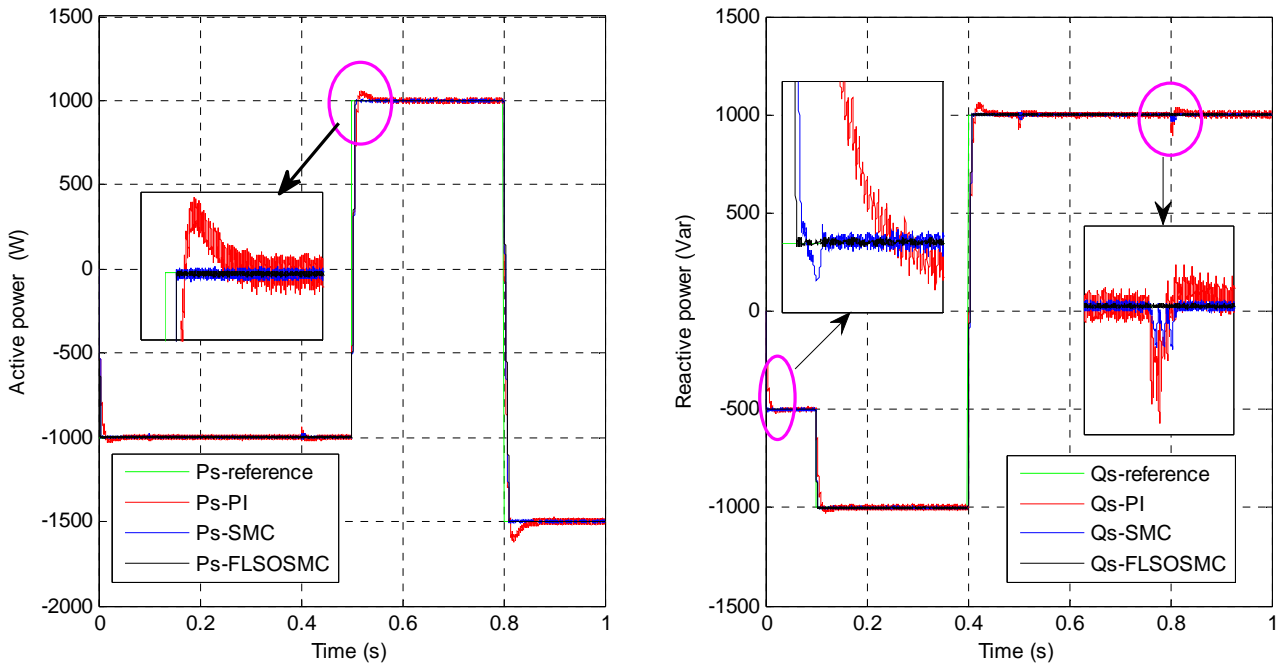
Fig. 9. Sensitivity to the reactance variation (XL –30 %)

Sensitivity to a sub-voltage perturbation. The aim of this test is to analyze the influence of a sub-voltage perturbation (+50 %) in the time interval $t = 0.6$ s and $t = 0.62$ s on active and reactive powers for the 3 controllers. The simulation results are shown in Fig. 10. This figure expresses that the introducing perturbation produced a slight effect on the power curves with PI controller. While the effects are almost negligible for the system with the two other controllers. This result is attractive for UPFC applications to ensure stability and quality of the active and reactive powers when the voltage is varying.
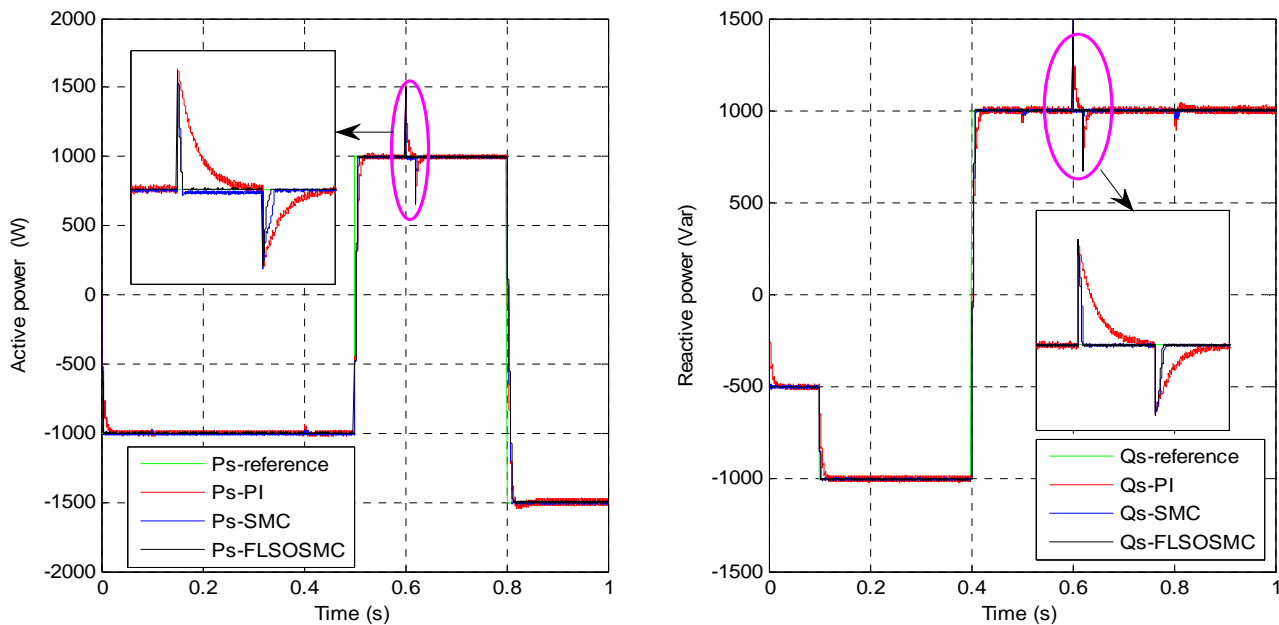
Fig. 10. Sensitivity to sub-voltage perturbation (+50 %)

Conclusion. A robust control method based on variable structure technique of a UPFC has been presented in this paper. Simulation results verified the effectiveness of the control strategy that allows independent control and decoupled active and reactive power of these devices by minimizing the interaction effect between these powers. The Fuzzy logic second order sliding mode controller controller ensures a perfect decoupling between the two axes comparatively to the PI one where the coupling effect between them is very clear.

Results comparison between conventional PI Controller and the proposed Fuzzy logic second order sliding mode controller based controller for UPFC indicates that the proposed Fuzzy logic second order sliding mode controller based controller has less steeling time and less overshoot and compared with the conventional Proportional-Integral Controller.

Basing on all these results the UPFC device, can adjust the distribution the system power flow among the transmission line quickly and smoothly, and have no significant impact to other operating parameters of the system.

REFERENCES

1. IEEE Draft Recommended Practice for Monitoring Electric Power Quality. 2018.
2. Boudiaf M., Moudjahed M. Improvement of transient stability of power system by IPFC, SSSC and STATCOM. *Journal of Electrical Engineering*, 2014, vol.14, no.1, pp.257-272.
3. Yang S., Liu Y., Wang X., Gunasekaran D., Karki U., Peng F.Z. Modulation and Control of Transformerless UPFC. *IEEE Transactions on Power Electronics*, 2016, vol.31, no.2, pp. 1050-1063. **doi: 10.1109/tpel.2015.2416331.**
4. Krishna T.M., Anjaneyulu K.S.R. Coordination of intelligent controllers for shunt and series converters of UPFC. *2015 Conference on Power, Control, Communication and Computational Technologies for Sustainable Growth (PCCCTSG)*, Dec. 2015. **doi: 10.1109/pccctsg.2015.7503911.**
5. Round S.D. Performance of a unified power flow controller using a d-q control system. *Sixth International Conference on AC and DC Power Transmission*, 1996. **doi: 10.1049/cp:19960384.**
6. Sharma N. K., Jagtap P.P. Modelling and Application of Unified Power Flow Controller (UPFC). *2010 3rd International Conference on Emerging Trends in Engineering and Technology*, 2010. **doi: 10.1109/icetet.2010.169.**
7. Umre P.B., Bandal V.S., Dhamne A.R. Design of controller for Unified Power Flow Controller (UPFC) using Sliding Mode Control (SMC) strategies. *2014 5th International Conference – Confluence The Next Generation Information Technology Summit (Confluence)*, 2014. **doi: 10.1109/CONFLUENCE.2014.6949286.**
8. Shotorbani A., Ajami A., Zadeh S., Aghababa M., Mahboubi B. Robust terminal sliding mode power flow controller using unified power flow controller with adaptive observer and local measurement. *IEEE IET Generation, Transmission & Distribution*, 2014, vol.8, no.10, p.1712-1723. **doi: 10.1049/iet-gtd.2013.0637.**
9. Nayeripour M., Narimani M.S., Niknam T., Jam S. Design of sliding mode controller for UPFC to improve power oscillation damping. *Applied Soft Computing*, 2011, vol.11, no.8, 2011, pp. 4766-4772. **doi: 10.1016/j.asoc.2011.07.006.**
10. LÓpez J., Sanchis P., Roboam X., Marroyo L. Dynamic Behavior of the Doubly Fed Induction Generator During Three-Phase Voltage Dips. *IEEE Transactions on Energy Conversion*, 2007, vol.22, no.3, pp. 709-717. **doi: 10.1109/tec.2006.878241.**
11. Cupertino F., Naso D., Mininno E., Turchiano B. Sliding-Mode Control With Double Boundary Layer for Robust Compensation of Payload Mass and Friction in Linear Motors. *IEEE Transactions on Industry Applications*, 2009, vol.45, no.5, pp. 1688-1696. **doi: 10.1109/tia.2009.2027521.**
12. Bouanane A., Amara M., Chaker A. State space neural network control (SSNNC) of UPFC for compensation power. *2015 3rd International Renewable and Sustainable Energy Conference (IRSEC)*, Dec. 2015. **doi: 10.1109/irsec.2015.7455135.**
13. Kamel S., Jurado F., Lopes J.A.P. Comparison of various UPFC models for power flow control. *Electric Power Systems Research*, 2015, vol.121, pp. 243-251. **doi: 10.1016/j.epsr.2014.11.001.**
14. Mallick R.K., Nahak N., Sinha R.R. Fuzzy sliding mode control for UPFC to improve transient stability of power system. *2015 Annual IEEE India Conference (INDICON)*, Dec. 2015. **doi: 10.1109/indicon.2015.7443182.**
15. Meng W., Qinxiang G., Leiting C., Liqiang L., Caiyun Z. Mathematical Model and Control Strategy of UPFC. *2014 Sixth International Conference on Measuring Technology and Mechatronics Automation*, Jan. 2014. **doi: 10.1109/icmtma.2014.96.**
16. Wai R.J., Chang J.M. Implementation of robust wavelet-neural-network sliding-mode control for induction servo motor drive. *IEEE Transactions on Industrial Electronics*, 2008, vol.50, no.6, pp. 1317-1334. **doi: 10.1109/TIE.2003.819570.**
17. Utkin V.I. Sliding mode control design principles and applications to electric drives. *IEEE Transactions on Industrial Electronics*, 1993, vol.40, no.1, pp. 23-36. **doi: 10.1109/41.184818.**
18. Astrom K.J., Wittenmark B. *Adaptive Control*. New York, Addison-Wesley, 1995.
19. Sun T., Chen Z., Blaabjerg F. Flicker study on variable speed wind turbines with doubly fed induction generators. *IEEE Transactions on Energy Conversion*, 2005, vol.20, no.4, pp.896-905. **doi: 10.1109/TEC.2005.847993.**
20. Slotine J.J.E., Li W. *Applied Nonlinear Control*. Englewood Cliffs, NJ, Prentice-Hall, 1991.
21. Slotine J.-J.E. Sliding controller design for non-linear systems. *International Journal of Control*, 1984, vol.40, no.2, pp. 421-434. **doi: 10.1080/00207178408933284.**
22. Tseng M.-L., Chen M.-S. Chattering reduction of sliding mode control by low-pass filtering the control signal. *Asian Journal of Control*, 2010, vol.12, no.3, pp. 392-398. **doi: 10.1002/asjc.195.**
23. Boudjema Z., Meroufel A., Djerriri Y., Bounadja E. Fuzzy sliding mode control of a doubly fed induction generator for wind energy conversion. *Carpathian Journal of Electronic and Computer Engineering*, 2013, vol.6, no.2, pp. 7-14.
24. Levant A., Alelishvili L. Integral High-Order Sliding Modes. *IEEE Transactions on Automatic Control*, 2007, vol.52, no.7, pp. 1278-1282. **doi: 10.1109/tac.2007.900830.**
25. Benelghali S., Benbouzid M.E.H., Charpentier J.F., Ahmed-Ali T., Munteanu I. Experimental Validation of a Marine Current Turbine Simulator: Application to a Permanent Magnet Synchronous Generator-Based System Second-Order Sliding Mode Control. *IEEE Transactions on Industrial Electronics*, 2011, vol.58, no.1, pp. 118-126. **doi: 10.1109/tie.2010.2050293.**

Abdellatif Hinda[1], *Associate Professor,*
Mounir Khiat[1], *Doctor of Power Engineering, Professor,*
Zinelaabidine Boudjema[2], *Doctor of Power Engineering, Professor,*
[1] SCAMRE Laboratory,
Department of Electrical Engineering,
ENP Oran, Algeria.
[2] Electrical Engineering Department,
University of Chlef, Algeria,
e-mail: abdellatif.hinda2@gmail.com

A. Rahmani, L. Slimani, T. Bouktir

UNBALANCED LOAD FLOW WITH HYBRID WAVELET TRANSFORM AND SUPPORT VECTOR MACHINE BASED ERROR-CORRECTING OUTPUT CODES FOR POWER QUALITY DISTURBANCES CLASSIFICATION INCLUDING WIND ENERGY

Purpose. The most common methods to design a multiclass classification consist to determine a set of binary classifiers and to combine them. In this paper support vector machine with Error-Correcting Output Codes (ECOC-SVM) classifier is proposed to classify and characterize the power quality disturbances such as harmonic distortion, voltage sag, and voltage swell include wind farms generator in power transmission systems. Firstly three phases unbalanced load flow analysis is executed to calculate difference electric network characteristics, levels of voltage, active and reactive power. After, discrete wavelet transform is combined with the probabilistic ECOC-SVM model to construct the classifier. Finally, the ECOC-SVM classifies and identifies the disturbance type according to the energy deviation of the discrete wavelet transform. The proposed method gives satisfactory accuracy with 99.2% compared with well known methods and shows that each power quality disturbances has specific deviations from the pure sinusoidal waveform, this is good at recognizing and specifies the type of disturbance generated from the wind power generator. References 22, tables 8, figures 9.
Key words: **unbalanced load flow, wavelet transform (WT), support vector machines (SVM), power quality disturbance, wavelet energy.**

Цель. Наиболее распространенные методы построения мультиклассовой классификации заключаются в определении набора двоичных классификаторов и их объединении. В данной статье предложена машина опорных векторов с классификатором выходных кодов исправления ошибок (ECOC-SVM) с целью классифицировать и характеризовать такие нарушения качества электроэнергии, как гармонические искажения, падение напряжения и скачок напряжения, включая генератор ветровых электростанций в системах передачи электроэнергии. Сначала выполняется анализ потока несимметричной нагрузки трех фаз для расчета разностных характеристик электрической сети, уровней напряжения, активной и реактивной мощности. После этого дискретное вейвлет-преобразование объединяется с вероятностной моделью ECOC-SVM для построения классификатора. Наконец, ECOC-SVM классифицирует и идентифицирует тип возмущения в соответствии с отклонением энергии дискретного вейвлет-преобразования. Предложенный метод дает удовлетворительную точность 99,2% по сравнению с хорошо известными методами и показывает, что каждое нарушение качества электроэнергии имеет определенные отклонения от чисто синусоидальной формы волны, что способствует распознаванию и определению типа возмущения, генерируемого ветровым генератором. Библ. 22, табл. 8, рис. 9.
Ключевые слова: **несбалансированный поток нагрузки, вейвлет-преобразование (WT), машины опорных векторов (SVM), нарушение качества электроэнергии, энергия вейвлета.**

Introduction. The quality of energy has become an important issue for electric users and their customers. With the rapid increase of wind energy, this quality can be easily disturbed by the distortion in the supply of the electric power network that can lead to high costs and create many problems.

Problem statement and definition. To improve and ensure the quality of the electrical energy, the disturbances must be detected and if possible the detection must be close to the source of these disturbances. Several criteria can set the quality of energy which includes the voltage waveform, harmonics, inter harmonics, transient voltage, frequency voltage, frequency stability, voltage fluctuations (flicker)...etc [1]. To improve the power quality in [2] found that the load flow analysis is an important part and essential step for any power system network computation and it has always been useful by many power system engineers in this domain. Furthermore, they propose a novel approach using a 25 IEEE bus test system to solve the reorder of the unbalanced distribution network including optimal distribution network including optimal location of dispersed production units. By the comparison with other results obtained before, the results of this new technique are better to reduce losses and improve the PQ characteristics in distribution network level. With a same way, In [3] a modification has been done for the CPC power theory to four-wire unbalanced power, for

objective to gives the smallest possible line losses in the same transferred of the active power to the load in non symmetrical and unbalanced distribute voltage. For this reason a load flow is an important analysis tool to improve the PQ [4].

On the other hand, the wavelet transform has an important part in power system, and the development of this tool allowed many scientists to operate in various domains among them power quality. First applied of wavelets transform in power system by Ribeiro and Robertson in 1994 [5, 6]. From this year till now the number of publications in this domain has increased and the most popular wavelet analysis in power systems are used and applied for amelioration of power quality.

Overview of the most well-known evolutionary classifier on the topic. In the literature various methods based on wavelet transform (WT), fuzzy logic, neural network (NN), support vector machine (SVM), particle swarm optimization (PSO) and genetic algorithm (GA) have been proposed and implemented for PQD identification and classification.

In [7] present a combination of binary classifiers method, the proposed PQD classifier is based on WT and SVM, this method uses a one-vs-one multiclass SVM (four SVM nodes) each node is contain one event and trained individually allowing them to be parallelized. In general, the results display a good performance and the

PQ events can be detected. A novel method of automatic classification of hybrid or single PQD is proposed by [1], this proposed algorithm depend of the Discrete Wavelet Transform (DWT) and Probabilistic NN based Artificial Bee Colony (PNN-ABC) optimal feature selection of PQD, the DWT utilized for the feature extraction of the disturbances and the PNN is applied as an operative and dynamic classifier for the classification of the PQD. After the results, they found that the proposed algorithm is a significantly upper technique forcharacterize and identifying the single and various PQD. On the other hand, [8] are presents a new approach consisting linear Kalman filter and fuzzy-xpert system for identification and classification of voltage and current disturbances in power systems. Linear Kalman filter together with DWT is used to extract the parameters and these parameters are the inputs to fuzzy-xpert system that uses to identify the class of the PQD. A new method to classify and detect PQD in power system based fuzzy logic (FL) and neural networks basis radial function (RBFNN) are suggested in [9], RBFNN used the feature extracted by wavelet as inputs to generate membership function in FL and features to collect various events using FL detection and classification. The comparison showed that the classification accuracy of the fuzzy logic is improved just by the help of PSO, more details in [10]. Other techniques based on fuzzy and WT have been presented in [10, 11]. In [12] is presented another methodology that uses a maximal overlap discrete wavelet transform (MODWT) technique to recognition and locating of different PQD, the coefficients extracted from MODWT used like input for the classifiers. The obtained results show that the Decision Tree (DT) provides better classification accuracy than the SVM at every case with and without noise. Otherwise, the selection tree is working satisfactorily with synthesized or real signals. Probabilistic neural network (PNN) has been used in [13] as a function approximation tool for PQD classification and genetic algorithm (GA) is used to optimize the PNN parameter and the results demonstrate that the method is more accurate than the other methods presented. Another method has been presented in [14], S-transform with double-resolution (DRST) combined with directed acyclic graph based on support vector machines (DAG-SVMs). First, DRST are used for an effective feature extraction from power signals. Then, the DAG-SVMs classify and predict the PQD. Obtained results of this proposed show that the automatic classification algorithm is powerful and has the ability to distinguish and to detect different power quality phenomena classes easily. In [15] is displayed a performance enhancement scheme for the recently developed extreme learning machine (ELM) for classifying PQD using particle swarm optimization (PSO), the results indicated that the proposed algorithm faster and more accurate in discriminating PQD, and overall accuracy was 97.6 %. Other methods based on SVM and WT have been presented in [7, 16], wavelet and neural network [1, 17].

Generally, each research has a different strategy and this is good for providing information and to predict the classes of PQD and each method has its negatives and positives, also the significance of the importance of

unbalanced load flow analysis is needed for more information and good contribution and to generalize all PQD especially in transmission network to reduce power losses and to improve the PQ characteristics for electric users and their customers.

The goal of the paper is to overcome the advantages we propose in this paper a recognized method based unbalanced load flow to extract and calculate difference system data such as voltage, reactive and active power. After, this data are used to calculate the energy deviation of the waveform signal using the discrete wavelet transform, in which the support vector machines with Error-Correcting Output Codes (ECOC-SVM) locates the importance values including to classify some kinds of power quality disturbances produced from the wind energy.

Wavelet transform. Discrete wavelet transform (DWT) is an implementation using a discrete set of scales and wavelet translations obeying certain rules. With $a = a_0^m$ and $b = nb_0 a_0^m$, where $a_0 > 1$, $b_0 > 0$, and m, n are integers

$$DWT = (m,n) = \int_{-\infty}^{+\infty} x(t)\psi^*(t)dt, \qquad (1)$$

where «m» scale and «n» shift (translation)

$$\psi^*(t) = a_0^{\frac{m}{2}}\left(\left(t - na_0^m b_0\right)\middle/ a_0^m\right). \qquad (2)$$

In other words, this technique decompose the signal into a set of mutually orthogonal wavelets, which is the major difference with continuous wavelet transform.

Energy of signal. The energy of the disturbed signal will divided into different resolution levels by different ways depending on the power quality events at hand. So, the standard deviation at different resolution levels of the decomposed signal (Equations (1) and (2)) and MRA is proposed in this technique as feature to classify different power quality problems. The energy used in our study in equations (3), is the vector containing the percentages of energy corresponding to the details at different resolution levels, given by

$$E_d(K) = \frac{\sum \left(C_{d_K}\right)^2}{\sum C^2} \cdot 100, \qquad (3)$$

where C is the vector contains the wavelet decomposition and C_d is the vector contains the detail coefficients at level k, using the DWT.

All of the waveforms in this paper are simulated in MATLAB Simulink with IEEE 9 Bus system [18]. We generated pure sine wave (frequency 60 Hz and the amplitude in p.u).

Proposed method. The block diagram in Fig. 1 demonstrate the proposed method. Where the Support Vector Machine (SVM) with Error-Correcting Output Codes (ECOC) classifier is proposed to classify and characterize the power quality disturbances such as voltage sag, voltage swell and harmonic distortion, which are possible to be produced from the wind energy.
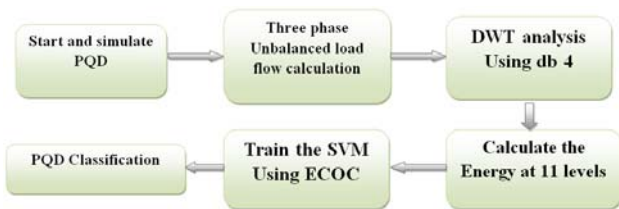
Fig. 1. Block diagram representing the simulation steps

Firstly, 3 phases unbalanced load flow analysis is executed to calculate different electric network characteristics, levels of voltage, active and reactive power. After, a wavelet transform is applied to decompose the signal by DWT. Using the equation (3), we calculate the energy of the decomposed signal. Finally, the ECOC-SVM classifies and identifies the disturbance type according to the energy deviation of the DWT.

Applications and results. Possible causes of the voltage sag include short circuit faults, electric motors starting, turning on of heavy equipment, capacitor switching, etc. Sag can occur on multiple-phase or on a single phase, and are often accompanied by voltage swells on other healthy phases. Where, the harmonic currents produced by some nonlinear loads on the system, such as adjustable speed drives, arc furnace loads, computers, copiers, etc. The wind power generator has a possibility to generate all this kinds of disturbances. By this way, we have generated different power quality problems using the IEEE 9 Bus model (Fig. 2).
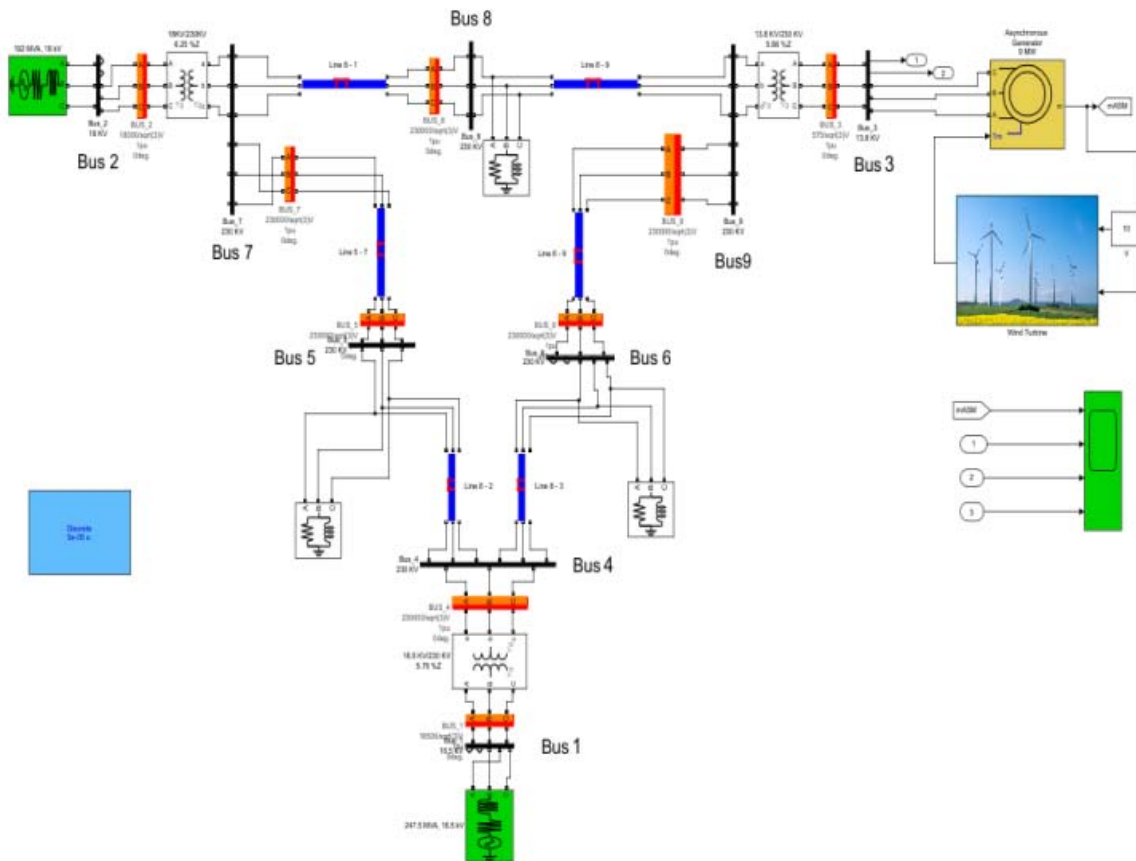
Fig. 2. IEEE 9 bus system network

In this study, sag and swell voltages caused by a short circuit fault at bus 6 and the rectifiers (diode) are used in our study as source of harmonics on the network at the same bus with 90 % power factor (cosθ = 0.9) in Bus 6, take in consideration the main characteristics of event in power system [19].

Unbalanced Load Flow Results. Load flow analysis is an important part and essential step for any power system network computation and it has always been useful by many power system engineers in this domain to improve the power quality and to reduce the power losses. Most methods use a balanced load flow (single or simple phase), this gives low information quantity, especially in three phase system in transmission or distributed network. For this reason, unbalanced load flow is needed to extract a maximum of information in each phase. Table 1, 2 and Fig. 3 presents 3 phase unbalanced load flow results.

Fig. 3. Voltage profile of the three phase load flow results

Table 1 represents the phase magnitude voltage, angle, active and reactive powers in each generator bus and Table 2 represent the load buses. It can be seen the non-symmetrical values in some buses, especially in case of the manager's fault (phase C), where Fig. 3 shows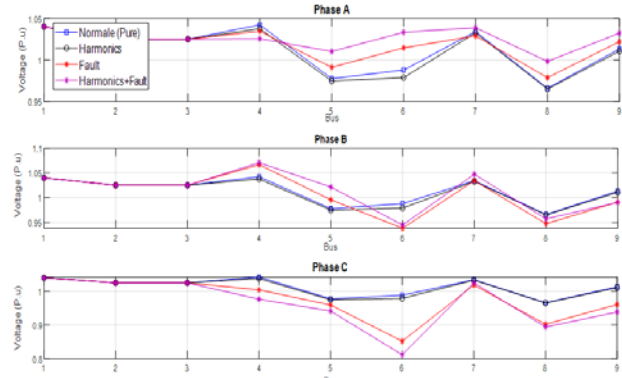 in detail the voltage profile and the minimum voltage found in case 4 (harmonics + fault), especially in phase C at bus 6 and its observed also near to this bus. Furthermore, in the harmonic disturbance results, there is a difference between all buses, this is due to the location of the harmonic source (bus 6) and the total distortion harmonic (THD) in each bus when THD in bus 1 was 1.16 % in bus 6 30.29 % and 21.3 % in bus 5, The same thing for the other disturbances.

DWT Results. The appropriate select of the mother wavelet perform an important part in detecting, localizing and analysing different kinds of signal variations, the choice relies on the nature of the application. For detection of low amplitude, short duration, fast decaying and oscillating type of signals, the most popular wavelets are Daubechies and Symlets families (db2, db3 and sym2, sym3… etc). Wavelet Daubechies «db4» is used to execute the DWT with 11 decomposition levels.

Figure 4 shows the distorted energy distribution at each level, we could not actually recognize the features. High and low frequency disturbance come in 5th, 6th and 9th level. The results showed that the sag energy deviation levels are less than the pure energy deviation levels, and minimum values concentrates between 6th and 9th levels. Contrary to the value of energy in voltage swell is more than the pure signal, also the voltage swell has the maximum energy deviation at level 8. These figures have been tested and proved using the IEEE 9-bus network (Fig. 2).
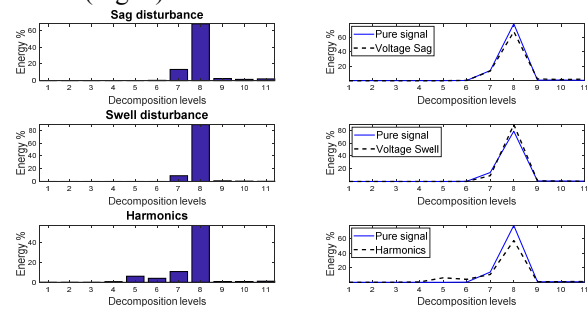

Fig. 4. Distortion energy distribution in each level

Table 1

Unbalanced load flow results for the Generators Buses

		Phase A				Phase B				Phase C				Total			
		Voltage		Power		Voltage		Power		Voltage		Power		Voltage		Power	
		p.u	angle	MW	Mvar	p.u	angle	MW	Mvar	p.u	angle	MW	Mvar	p.u	angle	MW	Mvar
BUS 1	Normal (pure)	1.04	0	27.4	–0.67	1.04	–120	27.4	–0.67	1.04	120	27.4	–0.67	1.04	0	82.21	–2.02
	Harmonics	1.04	0	25.89	2.04	1.04	–120	25.89	2.04	1.04	120	25.89	2.04	1.04	0	77.67	6.13
	Fault (phase C)	1.04	0	25.72	3.87	1.04	–120	31.33	–15.15	1.04	120	106.98	31.07	1.04	0	164.04	19.80
	Harm + Fault	1.04	0	8.85	8.81	1.04	–120	12.92	–18.22	1.04	120	106.74	47.96	1.04	0	128.51	38.57
BUS 2	Normal (pure)	1.025	9.54	54.32	–2.36	1.025	–110.46	54.32	–2.36	1.025	129.54	54.32	–2.36	1.025	9.54	162.97	–7.07
	Harmonics	1.025	9.96	54.33	–1.54	1.025	–110.04	54.33	–1.54	1.025	129.96	54.33	–1.54	1.025	9.96	163	–4.63
	Fault (phase C)	1.025	14.26	54.33	0.53	1.025	–114.3	54.33	–2.4	1.025	113.85	54.33	6.30	1.141	4.61	163	4.44
	Harm + Fault	1.025	19.15	54.33	–4.82	1.025	–111.17	54.33	–9.57	1.025	114.46	54.33	2.58	1.0091	7.49	163	–11.81
BUS 3	Normal (pure)	1.025	2.74	28.3	7.61	1.025	–117.26	28.3	7.61	1.025	122.74	28.3	7.61	1.025	2.74	84.90	22.83
	Harmonics	1.025	3.16	28.33	9.14	1.025	–116.54	28.33	9.14	1.025	123.46	28.33	9.14	1.025	3.46	85	27.42
	Fault (phase C)	1.025	9.93	28.33	2.43	1.025	–122.03	28.33	20.59	1.025	101.67	28.33	38.26	1.0042	–3.46	85	61.28
	Harm + Fault	1.025	15.32	28.33	–3.53	1.025	–118.58	28.33	20.94	1.025	100.97	28.32	51.27	0.9942	–0.73	84.99	68.69

Table 2

Unbalanced load flow for the Load Buses

		Phase A				Phase B				Phase C				Total			
		Voltage		Power		Voltage		Power		Voltage		Power		Voltage		Power	
		p.u	angle	MW	Mvar	p.u	angle	MW	Mvar	p.u	angle	MW	Mvar	p.u	angle	MW	Mvar
BUS 5	Normal (pure)	0.9777	–3.66	41.63	16.58	0.9777	–123.66	41.63	16.58	0.9777	116.34	41.63	16.58	0.9777	–3.66	124.89	49.75
	Harmonics	0.9748	–3.44	41.67	16.67	0.9748	–123.44	41.67	16.67	0.9748	116.56	41.67	16.67	0.9748	–3.44	125	50
	Fault (phase C)	0.9713	–1.85	41.67	16.67	0.9957	–125.56	41.67	16.67	0.9093	104.58	41.67	16.67	0.9541	–7.42	125	50
	Harm + Fault	1.0103	2.33	41.67	16.67	1.0495	–122.4	41.67	16.67	0.9413	105.86	41.67	16.67	0.9933	–4.48	125	50
BUS 6	Normal (pure)	0.9879	–4.73	29.88	9.93	0.9879	–124.73	29.88	9.93	0.9879	115.27	29.88	9.93	0.9879	–4.73	89.64	29.78
	Harmonics	0.9789	–3.86	28.47	13.8	0.9789	–123.86	28.47	13.8	0.9789	116.14	28.47	13.8	0.9789	–3.86	85.4	41.4
	Fault (phase C)	1.0646	–0.74	30	10	0.9382	–124.77	30	10	0.7239	86.77	30	10	0.8835	–10.62	90	30
	Harm + Fault	1.0933	2.09	28.47	13.8	0.9448	–119.96	28.46	13.8	0.5869	80.18	28.45	13.8	0.8369	–7.67	85.38	41.39
BUS 8	Normal (pure)	0.9661	–1.72	33.42	11.65	0.9661	–121.72	33.42	11.65	0.9661	118.28	33.42	11.65	0.9661	–1.72	100.25	34.94
	Harmonics	0.9651	–1.1	33.33	11.67	0.9651	–121.1	33.33	11.67	0.9651	118.9	33.33	11.67	0.9651	–1.1	100	35
	Fault (phase C)	0.9788	4.54	33.33	11.67	0.9475	–126.1	33.33	11.67	0.9023	99.21	33.33	11.67	0.9276	–7.09	100	35
	Harm + Fault	0.9984	10.31	33.33	11.67	0.9572	–122.34	33.33	11.67	0.8940	99.2	33.33	11.67	0.9273	–3.54	100	35

Using the proposed rules extracted from MRA technique at different levels with MRA curve the recognizing waveform problem becomes more easily and we can localize and detect and also classify several PQ events. When sag occurs, the 8th level also when the signal suffers harmonic distortion the 5th and 6th levels show noticeable variations, and this is clear in Fig. 5.

The percentages of energy depend on many factors, value of the disturbance, the duration, the location of this disturbance (in which bus) also the parameter of the network system as lines, load, voltage source…etc.

However, to preserve the complete information Std-MRA curve values of all levels of MRA are considered as an input to SVM to classify the power quality events.
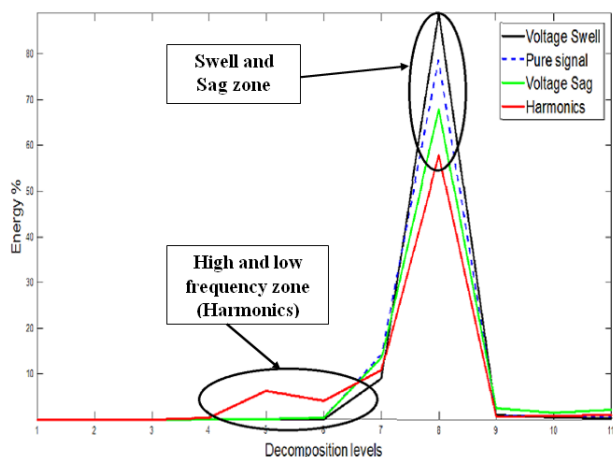

Fig. 5. Families of energy deviation curve for different PQD

Support Vector Machine results. A Support Vector Machine (SVM) is a special classifier formally and known by a separating hyperplane. In the other words, given name as training data (supervised or control learning), the algorithm outputs an optimal hyperplane which classify new examples (Fig. 6). For that reason our objective should be to obtain the line passing as far as possible from all points. Then, the process of the SVM algorithm is based on locate the optimal hyperplane that determinate the largest distance between the two class to the training examples. In this case, the classification becomes very dynamic and more precise. Different kernel functions are used and applied in the literature. The Gaussian kernel (Equation (4)) is an example of radial basis function kernel which gives the best results is selected [20]

$$k(x, y) = \exp\left(-\frac{\|x - y\|^2}{2\sigma^2}\right).$$ (4)

The adjustable parameter σ represent a significant role in the behavior of kernel, and should be carefully adjust to the problem at hand. If overestimated, the exponential will behave almost linearly and the higher-dimensional projection and forecast will start to lose its non-linear capacity. In the other hand, if underestimated the function will miss regularization and the decision limit will be highly sensitive to unrest in training data.

Two-Class Support Vector Machine. From the simulated signals, DWT is applied to the signals waveforms. After, the energy of the decomposition levels

obtained using the DWT are used for SVM. The basic idea of SVM is to plan the training data from the input area into a higher dimensional feature space through Gaussian kernel function. By this away, space optimal hyper plane is specified and determined to maximize the generalization ability of the classifier. Before the training process, input data are normalized and divided into 500 sets for training and 300 sets for test. A structure of the support vector machines consists of 2 or 3 inputs (Energy level), for example [Ed6 – Ed8] or [Ed6 – Ed8– Ed9] as illustrated in Table 3. The output variables of the support vector machines are designated as value range from 1 to 6, which corresponds to the different power quality problems:

A: «1» corresponds to Voltage swell;
B: «2» corresponds to Voltage sag;
C: «3» corresponds to Harmonic;
D: «4» corresponds to Voltage swell + Harmonic;
E: «5» corresponds to Voltage sag + Harmonic;
F: «6» corresponds to pure (without problems).

We have 5 Two-Class SVM models are used and each model contains 2 types of the power quality problems (Table 3). For each SVM model, the adjusted parameters out-of sample classification error are investigated as the most appropriate parameters so that the obtained output is only specified or determined the effect of choice or with energy level are good for the training of the SVM and also for the classification. After the training process, case studies are varied so that the decision algorithm capability can be verified. The total numbers of the case studies are 300.
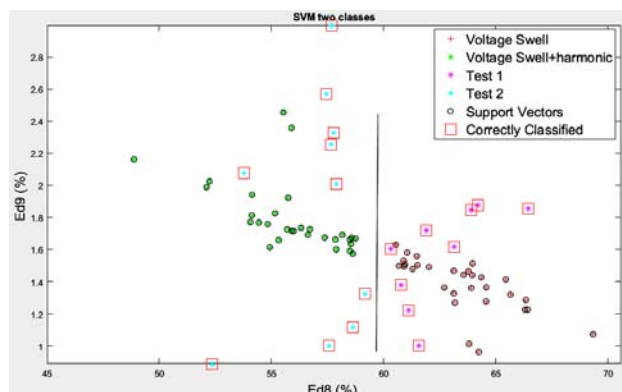

Fig. 6. Classification by two-class SVM between Voltage swell and Voltage swell + Harmonic

Table 3
Out-of sample classification error for two-class SVM

SVM Models	Ed 6 & Ed 9	Ed 8 & Ed 6	Ed 8 & Ed 9	Ed 6 & Ed 8 & Ed 9
A & B	0 %	2 %	2 %	0 %
B & C	0 %	0 %	0 %	0 %
C & E	27 %	7 %	10 %	0 %
C & D	16 %	13 %	21 %	9 %
D & E	12 %	3 %	5 %	0 %
Average	12 %	5 %	7.6 %	1.8 %

Multi-Class SVM (ECOC-SVM). The most common framework or methods already used Kernel functions. Well known classic SVM was developed for binary classification, if a multi class classifier is needed

such as the case of PQD classification, particularly where the signals include more than one disturbance or more problems, in this situation the SVM needs to be achieved in several steps. The natural extension is to combine various binary classifiers to response and to comply a binary decision tree. Error-Correcting Output Codes (ECOC) represent a effective structure to handling with these kinds of problems. However, the performance is influenced by the size and degree of the problem. In addition, for the particular case analyzed in this paper, multi ECOC technique or Fit multiclass models for support vector machines (fitcecoc) are used [21]. Multi ECOC technique is based on a reduction of multiclass classification problems to a set and combination of binary SVM where certain decoding scheme and coding design are used for the prediction of classification results according to binary SVM predictions (Fig. 7):

- max objective evaluations of 30 reached;
- total function evaluations: 30;
- total elapsed time: 50.6946 sec;
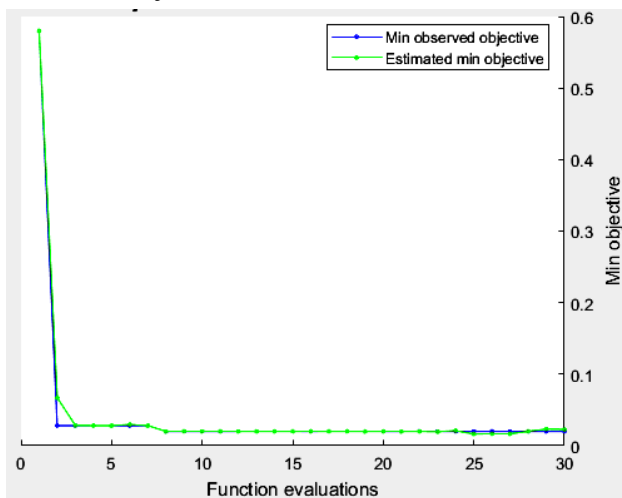- total objective function evaluation time: 8.1846.

Fig. 7. Min objective vs Number of function evaluations

Table 4

Out-of sample classification error for ECOC-SVM

	Ed 8 & Ed 6	Ed 6 & Ed 8 & Ed 10	All Energy levels (Ed1-Ed11)
Out-of sample classification error ECOC-SVM	10.8 %	10 %	3.2 %

Wind turbine simulation and results. In this section, reconfiguration of the transmission network in the presence of power wind generator. As we know, this reconfiguration can disturb the network parameters and create some PQD (Harmonics and voltage perturbation), as seen in Fig. 9, by replacing the generator in bus 3 by a wind farm power generation and keeping the same power generation 85 MW (figure 2).

Figures 8 and 9 represent the simulation results, where Fig. 8 represent the mechanical power of the turbine and the speed of the asynchronous machine. On the other hand, Fig. 9 present the frequency, current and voltage waveform at bus 3 and table 8 represent the 3 phase load flow results with and without wind energy.
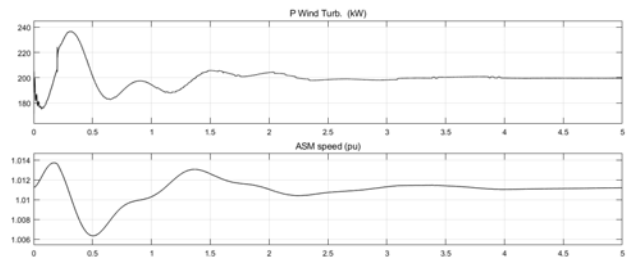

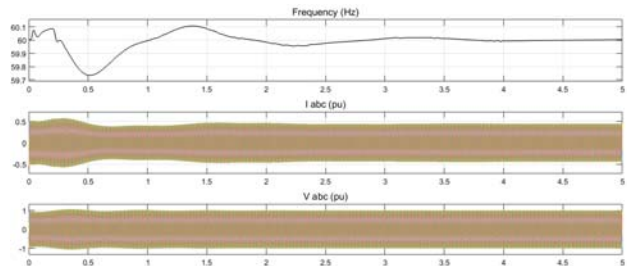Fig. 8. Turbine mechanical power and the ASM speed

Fig. 9. Frequency, current and voltage waveform at bus 3

In this part we will divide the signal produced from the wind generator at bus 3 into 3 parts (0-0.5 s, 0.5-1 s, 1-5 s), and we will try to detect the different perturbation on this signal using ECOC-SVM classifier. Table 5 shows the classification results.

Table 5

PQD classification generated by the wind generator using Ecoc-SVM classifier

SIGNAL PART	[0 – 0.5 s]	[0.5 – 1 s]	[1.5 – 4.5 s]
PQD class	D	E	F

Comparing performance with other classifiers. Tables 6 and 7 demonstrate the ability of the proposed method to identify and classify PQD with very high accuracies averaging to 99.2 %.

Table 6

Percentage of classification by ECOC-SVM and other existing classifiers

Type of power quality problem	ST with CFDT [22]	S-transform and DAG-SVMs [14]	Proposed ECOC-SVM
A	98.66 %	98.5 %	100 %
B	97.33 %	99 %	100 %
C	100 %	99.5 %	98 %
D	98 %	97 %	98 %
E	–	99.5 %	100 %
Average	98.49 %	98.7 %	99.2 %

Table 7

Classification accuracy rate of the proposed method compared with other methods

Method	Classification
Proposed method (ECOC-SVM)	99.20 %
Neural network with DWT and fuzzy logic [10]	98.17 %
Wavelet and fuzzy logic [11]	98.02 %
Wavelet and SVM [7]	93.43 %
PSO-ELM [15]	97.60 %
Fast Dyadic ST with CFDT [22]	98.66 %

The performance and the efficiency of the proposed method and algorithm is also compared with other existing classifiers, including wavelet transform and neural network, wavelet transform and neural fuzzy, wavelet and SVM. The most common methods to design multiclass classification is to determine a series of binary classifiers and to combine or collect them [14-16]. This work represents an effective framework to compact with these types of problems.

The results showed significant performance by different device and strategy of new problem dependent designs based on the ternary ECOC-SVM with out-of sample classification error are relatively low with 3.2 % (Table 4).

Table 8

Load flow results with and without wind energy in some buses

		Phase A				Phase B				Phase C				Total			
		Voltage		Power		Voltage		Power		Voltage		Power		Voltage		Power	
		p.u	angle	MW	Mvar	p.u	angle	MW	Mvar	p.u	angle	MW	Mvar	p.u	angle	MW	Mvar
BUS 3	Without wind	1.025	2.74	28.3	7.61	1.025	−117.26	28.3	7.61	1.025	122.74	28.3	7.61	1.025	2.74	84.90	22.83
	With wind	1.02	1.11	28.33	5.14	1.02	−116.1	28.33	5.14	1.02	123.5	28.33	5.14	1.02	1.15	85	15.42
BUS 8	Without wind	0.9661	−1.72	33.42	11.65	0.9661	−121.72	33.42	11.65	0.9661	118.28	33.42	11.65	0.9661	−1.72	100.25	34.94
	With wind	0.9555	2.1	33.99	10.41	0.9555	−117.9	33.99	10.41	0.9555	121.96	33.99	10.41	0.9555	1.88	101.97	31.23
BUS 6	Without wind	0.9879	−4.73	29.88	9.93	0.9879	−124.73	29.88	9.93	0.9879	115.27	29.88	9.93	0.9879	−4.73	89.64	29.78
	With wind	0.9620	3.27	29.77	8.96	0.9620	−115.84	29.77	8.96	0.9620	122.90	29.77	8.96	0.9620	3.52	89.33	29.6

Conclusion.

The paper introduces the application and the implementation of wavelet transform and multiresolution analysis signal decomposition as a powerful analysis tool in power system, the property of this wavelet demonstrate the capacity of this technique to extract significant information from the analyzed distorted signal. This information is partitioned into different zones where each zone can be used to observe and classify power quality problems. The results show clearly that the precision of the combination of discrete wavelet transform and support vector machines algorithm is highly acceptable as shown in previous tables. In the other hand, the proposed method is able to recognize and classify different power disturbance types efficiently with 99.2 % compared with well known methods. The further work will be the improvement of the algorithm by taking in consideration the real signals for the development of the practical protection system, it can also help in finding and locating the source and the cause of disturbance.

REFERENCES

1. Khokhar S., Mohd Zin A.A., Memon A.P., Mokhtar A.S. A new optimal feature selection algorithm for classification of power quality disturbances using discrete wavelet transform and probabilistic neural network. *Measurement*, 2017, vol.95, pp. 246-259. **doi: 10.1016/j.measurement.2016.10.013.**
2. Roosta A., Eskandari H.-R., Khooban M.-H. Optimization of radial unbalanced distribution networks in the presence of distribution generation units by network reconfiguration using harmony search algorithm. *Neural Computing and Applications*, 2018, vol.31, no.11, pp. 7095-7109. **doi: 10.1007/s00521-018-3507-0.**
3. Škrbić B., Mikulović J., Šekara T. Extension of the CPC power theory to four-wire power systems with non-sinusoidal and unbalanced voltages. *International Journal of Electrical Power & Energy Systems*, 2019, vol.105, pp. 341-350. **doi: 10.1016/j.ijepes.2018.08.032.**
4. Emiroglu S., Uyaroglu Y., Ozdemir G. Distributed reactive power control based conservation voltage reduction in active distribution systems. *Advances in Electrical and Computer Engineering*, 2017, vol.17, no.4, pp. 99-106. **doi: 10.4316/aece.2017.04012.**
5. Ribeiro P.F Wavelet transform: an advanced tool for analyzing non-stationary harmonic distortion in power system. *Proceedings of the IEEE International Conference on Harmonics in Power Systems*, Bologna, Italy, September 21-24, 1994.
6. Robertson D., Camps O., Mayer J. Wavelets and power system transients: feature detection and classification. *Proceedings of SPIE international symposium on optical engineering in aerospace sensing*, Orlando, FL, USA, April 5-8, 1994, vol.2242, pp. 474-487.
7. De Yong D., Bhowmik S., Magnago F. An effective power quality classifier using wavelet transform and support vector machines. *Expert Systems with Applications*, 2015, vol.42, no.15-16, pp. 6075-6081. **doi: 10.1016/j.eswa.2015.04.002.**
8. Abdelsalam A.A., Eldesouky A.A., Sallam A.A. Classification of power system disturbances using linear Kalman filter and fuzzy-expert system. *International Journal of Electrical Power & Energy Systems*, 2012, vol.43, no.1, pp. 688-695. **doi: 10.1016/j.ijepes.2012.05.052.**
9. Kanirajan P., Kumar V.S. Wavelet-based power quality disturbances detection and classification using RBFNN and fuzzy logic. *International Journal of Fuzzy Systems*, 2015, vol.17, iss.4, pp 623-634. **doi: 10.1007/s40815-015-0045-0.**
10. Reaz M.B.I., Choong F., Sulaiman M.S., Mohd-Yasin F., Kamada M. Expert system for power quality disturbance classifier. *IEEE Transactions on Power Delivery*, 2007, vol.22, no.3, pp. 1979-1988. **doi: 10.1109/tpwrd.2007.899774.**
11. Guo-Sheng Hu, Jing Xie, Feng-Feng Zhu. Classification of power quality disturbances using wavelet and fuzzy support vector machines. *2005 International Conference on Machine Learning and Cybernetics*, 2005. **doi: 10.1109/icmlc.2005.1527633.**
12. Upadhyaya S., Mohanty S. Localization and classification of power quality disturbances using maximal overlap discrete wavelet transform and data mining based classifiers. *IFAC-PapersOnLine*, 2016, vol.49, iss.1, pp 437-442. **doi: 10.1016/j.ifacol.2016.03.093.**
13. Manimala K., Selvi K. Power disturbances classification using S-transform based GA–PNN. *Journal of The Institution of Engineers (India): Series B*, 2015, vol.96, iss.3, pp 283-295. **doi: 10.1007/s40031-014-0144-6.**

14. Li J., Teng Z., Tang Q., Song J. Detection and classification of power quality disturbances using double resolution S-transform and DAG-SVMs. *IEEE Transactions on Instrumentation and Measurement*, 2016, vol.65, no.10, pp. 2302-2312. **doi: 10.1109/tim.2016.2578518**.

15. Ahila R., Sadasivam V., Manimala K. An integrated PSO for parameter determination and feature selection of ELM and its application in classification of power system disturbances. *Applied Soft Computing*, 2015, vol.32, pp 23-37. **doi: 10.1016/j.asoc.2015.03.036.**

16. Bosnic J.A., Petrovic G., Putnik A., Mostarac P. Power quality disturbance classification based on wavelet transform and support vector machine. *2017 11th International Conference on Measurement*, May 2017. **doi: 10.23919/measurement.2017.7983524**.

17. Bhavani R., Prabha N.R. A hybrid classifier for power quality (PQ) problems using wavelets packet transform (WPT) and artificial neural networks (ANN). *2017 IEEE International Conference on Intelligent Techniques in Control, Optimization and Signal Processing (INCOS)*, Mar. 2017. **doi: 10.1109/itcosp.2017.8303073**.

18. Available at: https://www.mathworks.com/matlabcentral/fileexchange/45936-ieee-9-bus?s_tid=srchtitle (accessed 13 May 2018).

19. Muhammad Zaid M., Malik M.U., Bhatti M.S., Razzaq H., Aslam M.U. Detection and classification of short and long duration disturbances in power system. *Journal of Electrical Systems*, 2017, vol.13, iss.4, pp 779-789.

20. Ekici S. Classification of power system disturbances using support vector machines. *Expert Systems with Applications*, 2009, vol.36, iss.6, pp 9859-9868. **doi: 10.1016/j.eswa.2009.02.002.**

21. Escalera S., Pujol O., Radeva P. On the decoding process in ternary error-correcting output codes. *IEEE Transactions on Pattern Analysis and Machine Intelligence*, 2010, vol.32, no.1, pp. 120-134. **doi: 10.1109/tpami.2008.266**.

22. Biswal M., Dash P.K. Measurement and classification of simultaneous power signal patterns with an S-transform variant and fuzzy decision tree. *IEEE Transactions on Industrial Informatics*, 2013, vol.9, no.4, pp. 1819-1827. **doi: 10.1109/tii.2012.2210230.**

Ala eddine Rahmani[1], *Ph.D Student in Electrical Engineering*,
Linda Slimani[1], *Doctor in Electrical Engineering, Professor*,
Tarek Bouktir[1], *Doctor in Electrical Engineering, Professor*,
[1] Department of Electrical Engineering,
Université Ferhat Abbas Sétif 1, Algeria,
phone: +213 658 210 102,
e-mail: alaaeddinrahmani@yahoo.fr,
slimaniblinda@gmail.com, tbouktir@univ-setif.dz

R.V. Zaitsev, M.V. Kirichenko, G.S. Khrypunov, L.V. Zaitseva, O.N. Chugai, A.A. Drozdova

CONSTRUCTIVE SOLUTION OF HIGHLY EFFECTIVE PHOTOENERGY MODULE: DEVELOPMENT AND EXPERIMENTAL TESTING

Based on experimental study and computer modeling of working temperature influence on the efficiency of Chinese production silicon solar cells identified temperature dependence of efficiency shows the feasibility of using Chinese production Si-SC in the construction of photovoltaic thermal system, which together with the heat pump is part of a combined system for hot water supply, heating and air conditioning. Based on a detailed analysis of the working temperature influence on the efficiency of photovoltaic processes that determine the solar cells work, it has been developed the optimal construction and technological solution of hybrid solar generated module, the main feature of which is the heat exchange block, designed to reduce the solar cells working temperature. The experimental testing of hybrid modules samples equipped with developed cooling system, high-voltage part of power take-off system demonstrates their reliability and high efficiency which allow to achieve the such module efficiency up to 18.5 %. References 19, tables 1, figures 8.
Keywords: **silicon solar cells, working temperature, efficiency dependence, diode and output parameters, cooling system, solar irradiation concentration, hybrid solar generating module.**

На основе экспериментального исследования в комплексе с компьютерным моделированием влияния рабочей температуры на эффективность кремниевых солнечных элементов китайского производства выявлена температурная зависимость их эффективности. Температурная зависимость показывает целесообразность использования солнечных элементов китайского производства в составе фотоэлектрической тепловой системы, которая вместе с тепловым насосом является частью комбинированной системы горячего водоснабжения, отопления и кондиционирования воздуха. На основе детального анализа влияния рабочей температуры на эффективность фотоэлектрических процессов, определяющих работу солнечных элементов, было разработано оптимальное конструктивно-технологическое решение гибридного солнечного генерирующего модуля, основной особенностью которого является теплообменный блок, предназначен для снижения рабочей температуры солнечных элементов. Экспериментальные испытания образцов таких модулей, оснащенных разработанной системой охлаждения и высоковольтной системой отбора мощности, демонстрируют их надежность и высокую эффективность, позволяющие достичь КПД гибридного модуля до 18,5 %. Библ. 19, табл. 1, рис. 8.
Ключевые слова: **кремниевые солнечные элементы, рабочая температура, зависимость эффективности, диодные и выходные параметры, система охлаждения, концентрация солнечного излучения, гибридный солнечный модуль.**

Introduction. Now by increasing the efficiency of industrial production monocrystalline silicon solar cells (Si-SC) up to 17-18 % while significantly reducing their cost Chinese manufacturers were the largest exporters of photovoltaic products in the world [1]. A significant part of the manufacturers engaged in industrial production of solar modules, using Chinese-made solar cells. In addition, the largest segment of the market of imported solar modules also is occupied by Chinese manufacturers. For selling solar cells Chinese manufacturers in addition to efficiency and output parameters indicate the open circuit voltage (U_{oc}), short-circuit current density (J_{sc}), the fill factor (FF) of the illuminated current-voltage characteristic (CVC) which are measured at room temperature 25 °C.

However, during Si-SC working, according to the efficiency value only a small part of solar energy using to generate electricity. The majority of solar radiation has converted to heat in the device structure. This leads to an increase of Si-SC working temperature, which reduces their efficiency. In a significant amount of research works have been analyzed the influence of temperature on the efficiency of monocrystalline Si-SC, which are produced in European countries and Russia (see, [2-4]). Thus, established physical mechanisms lead to lower efficiency. At the same time, similar studies of Chinese production Si-SC with a few exceptions was not carried out [5]. Now a popular option for increasing a power of solar energy stations is the equipment of solar generating module (SGM) by low solar concentration system. Using low-

concentration of solar radiation is economically justified. The equipment of photovoltaic modules, by concentrators single or double-sided flat focline type, as shown in Fig. 1, with the degree of concentration up to 2, which is optimal for solar cells of conventional design based on single-crystal silicon allows to twice reduce the number of used solar cells, thereby reducing consumption of semiconductor material.

However, preliminary calculations of thermal parameters for SGM equipped with concentrator show that without cooling systems such using low-concentration solar radiation increases the SGM equilibrium temperature up to 55 °C, close to the maximum operating temperature of the Si-SC.

Fig. 1. Example of SGM module, equipped with a one-sided low solar concentration system

Thus, the study of temperature influence on the efficiency of photovoltaic processes in industrial samples of Chinese production Si-SC should be consider as relevant research objective, which has great practical importance. In the first phase were carried out, the experimental study the effect of temperature on the output diode parameters of industrial samples Chinese production Si-SC.

In the second stage, we analyze the physical mechanisms of the temperature effect on the output and diode parameters industrial samples of investigated Si-SC. Based on the experimental data obtained in the third step was the development of a hybrid solar generating module concept.

Aim of the investigation development of highly effective photoenergy module based on silicon solar cells construction solution and their experimental testing.

1. Experimental technique. According to the equivalent Si-SC circuit quantitative characteristics of photovoltaic processes that occur in such device structures are diode characteristics: density of the photocurrent (J_{ph}), the diode saturation current density (J_o), the coefficient of diode ideality (A), series resistance (R_s) and shunt resistance (R_{sh}), calculated per unit area of SC.

By the analyzing the literature [6], it can be shown that with increasing J_f, R_{sh}, and with decreasing J_o, A, R_s increases the efficiency of solar cells. The photocurrent density, which quantifies the effectiveness of nonequilibrium charge carriers generation and diffusion processes, determined by the number of photons arriving to the base layer, a quantum yield of the photoelectric effect and the of nonequilibrium charge carriers lifetime in the base layer. The values of the ideality coefficient and density of diode saturation current, which quantitatively characterize the efficiency of the of nonequilibrium charge carriers separation in Si-SC, controlled by the recombination speed in the space charge area and the energy structure of the separation barrier. Shunt resistance is included in the equivalent circuit of solar cells in order to take into account the influence on the efficiency photovoltaic processes of low resistivity local parts of the device structure and the end surfaces. The series resistance of solar cells, the amount of which determines the nonequilibrium charge carriers collection efficiency depends on the electrical conductivity of the base Si-SC layer, the contact resistance and the recombination speed of nonequilibrium charge carriers on the back and front contacts.

In this work calculation of output and diode parameters for investigated SC was carried out using the developed analytical processing program based on an approximation of the experimental illuminated CVC by the theoretical expression from [6]. Illuminated CVC Si-SC measured by the loaded method during Illumination SC by the solar radiation simulator for terrestrial conditions with the light power up to 100 mW/cm^2. Measuring scheme, which has shown in Fig. 2,*a*, as a source of simulating solar radiation includes LED Illuminator (Fig. 2,*b*) with microcontroller control.

The variable load resistance having six decades with the corresponding resistance values, which allows precisely vary value when measuring the CVC in the range from 0.01 up to 1000 Ohm. Registering of voltage value on load resistance has carried out by digital multimeter Mastech MS8226 DMM. Initial registering and control during measurements the value of radiation power on the SC front surface, were performed using standard Si-SC having a known value of the short-circuit current, and place it near the investigated Si-SC. By changing, the distance between the Si-SC and LED illuminator emitting element achieved the compliance with the actual value of I_{sc} for standard Si-SC to its value at 100 mW/cm^2 irradiance power, after that investigated Si-SC has been connected to the measuring circuit.
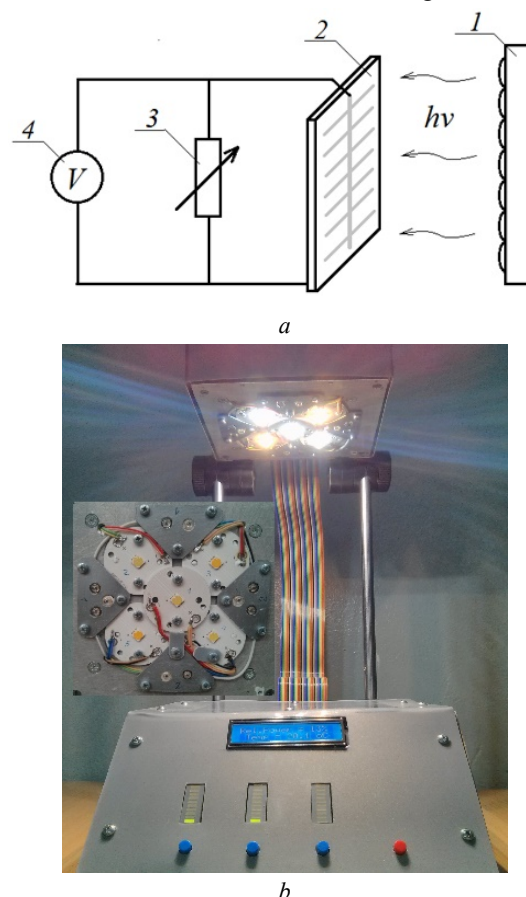

a

b

Fig. 2. Measuring scheme for investigated loaded current-voltage characteristics (*a*) and the appearance of the LED illuminator (*b*), the inset shows the location of the LEDs on the radiating element
(*1* – LED Illuminator; *2* – investigated Si-SC; *3* – variable load resistance; *4* – multimeter to measure the voltage on the load resistance)

3. Results and its discussion. For the experimental studies of the temperature effect on the output and diode parameters of Si-SC were selected monocrystalline Chinese production Si-SC with the characteristic values of efficiency, which represent the minimum, maximum and average values for the device structures on the market.

For this samples at temperatures from 0 °C up to 50 °C illuminated CVC were measured. As a result of subsequent analytical processing measured illuminated CVC were determined output and diode parameters investigated Si-SC.

The analysis shows that with increasing temperature, observed practically linear decrease of efficiency (Fig. 3, on this and other figures 1, 2, 3 is the numbers of investigated SC).
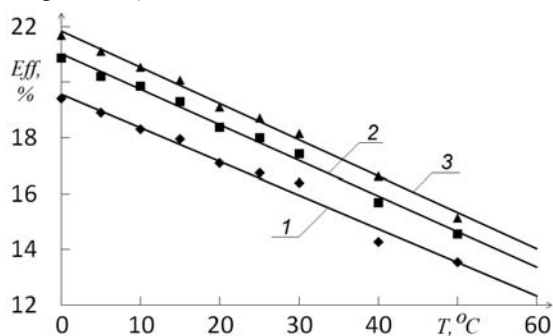

Fig. 3. Effect of working temperature on the Si-SC efficiency

The reduction factor, which describes the relative change of efficiency when the temperature changes by one degree, is 0.7 %/°C. For the open-circuit voltage and short circuit current density also observed reduce their values with increasing operating temperature (Fig. 4,a,b). Fill factor of the illuminated CVC does not change substantially with increasing temperature.
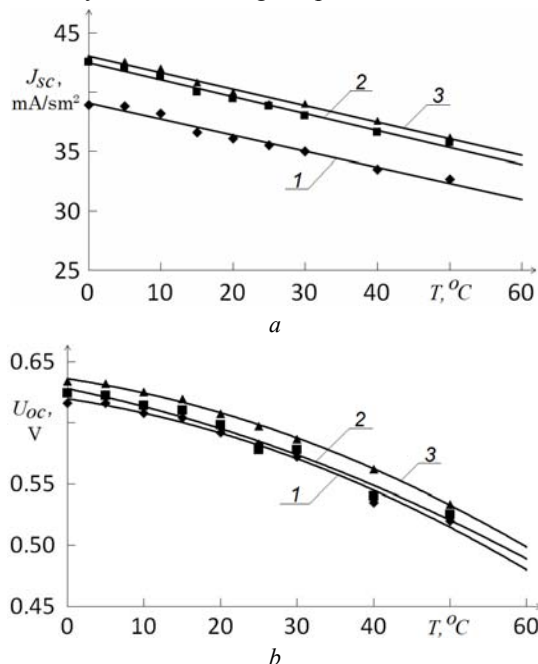

Fig. 4. Effect of working temperature on the Si-SC short circuit current density (a) and the open circuit voltage (b)

Analysis of the diode parameters showed that the recorded decrease of efficiency due to the increase of the diode saturation current density (Fig. 5,a) and a decrease of shunt resistance (Fig. 5,b).

The analysis of the physical mechanisms of the temperature effect on the output and diode parameters for Chinese production Si-SC industrial samples shown that experimental results are only partially can be commented upon in the framework of traditional ideas about the influence of temperature on the efficiency of photovoltaic processes in the Si-SC, which has described in [7]. According to traditional views, which correspond to the experimental studies of Si-SC at increasing the temperature the diffusion length of the nonequilibrium carriers in Si increases. This is because the diffusion coefficient is not changed or increased, and the minority carrier lifetime increases with increasing temperature. The increase of minority carriers diffusion length leads to an increase of short circuit current density with increasing temperature. However, this effect is small and its value on level 0.07 %/°C. Reduction of the open circuit voltage significantly exceeds the increase of short circuit current density and its value is up to 0.4 %/°C. Smoother shape of illuminated CVC at higher temperatures leads to reduce the fill factor of illuminated CVC. Overall, therefore, increase of temperature leads to a relative decrease of the efficiency on level of 0.5 %/°C.
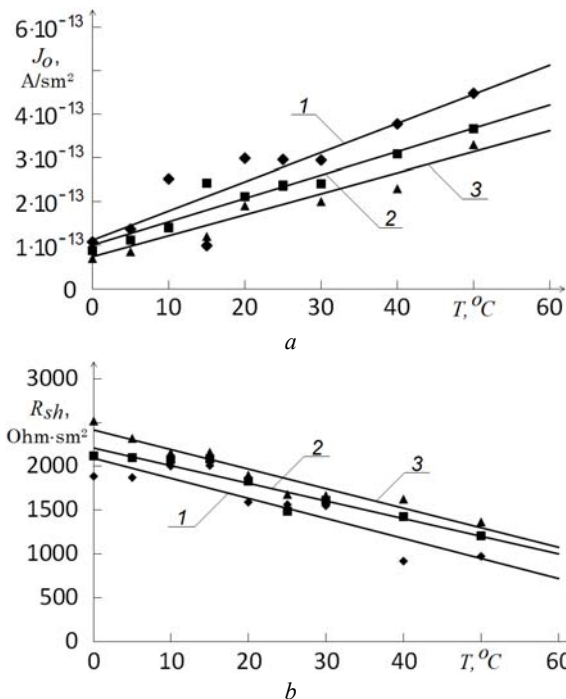

Fig. 5. Effect of working temperature on the density of diode saturation current (a) and shunt resistance (b)

According to the experimental data practically for Chinese-made solar cells relative efficiency reduction higher and its value is at 0.7 %/°C. At this the short-circuit current density decreases, and the fill factor of illuminated CVC practically unchanged.

According to the existing physical representations the density of the diode saturation current is the most important diode parameter, which effect on changes of SC output parameters with changes the working temperature. The exponential increase of diode saturation current density evidence that basic physical mechanism of J_o increase is thermally activated growth of the charge carrier's concentration. Since experimental dependence $J_o(T)$ is not a linearized in $\ln J_o - 1000/T$ coordinates, the mechanism is not only one, above mentioned. On its existence indicates the experimentally established unconventional decline of short-circuit current density with increasing of working temperature.

Analysis of diode parameters shows that the abnormally high efficiency reduction and non-traditional decrease of short-circuit current density due to experimentally registered decrease of shunt resistance.

Current in high conductivity areas reduce the contribution of the photocurrent in the short-circuit current and this current is additional physical mechanism that reduces efficiency.

Development of a hybrid photovoltaic module concept carried out based on experimentally established data about high speed of efficiency reduction for China production Si-SC. This fact reduces their relatively high initial output parameters and determines the feasibility of using them as a part of the hybrid solar generating module (HSGM), which is a hybrid of solar cells and solar thermal collector and allows to ensure cooling of the silicon device structure due to coolant circulation. Depending on the necessary technological requirements worked out three basic modes of HSGM working [8]: ensuring the most efficient power generation, ensuring maximum efficiency of thermal energy and maximizing the overall efficiency. In [9] developed designs that for maximize the electric power ensure the heat extraction from SC front surface to the environment and from the rear surface to the coolant circuit. The main feature of the module design that meets this working regime is the absence of air layer between the solar cells and translucent coating. With this working regime, the coolant temperature in the circuit must be less than 35 °C. However, since fluid heated by module has a low temperature, it is required that a further heating, which leads to the need for additional hardware. For example, this HSGM working regime enables combined system for hot water supply, heating and air conditioning based on heat pump and HSGM [10].

In this paper, for cooling Chinese production Si-SC we propose a simple and reliable design of a hybrid solar generated module. To realize the cooling system via a compound with heat conductivity (1.04-1.44) W/(m·K) is assumed to provide a thermal contact between the back surface of the solar module and aluminum absorber to which are welded aluminum tubes through which water flows.

We propose to gluing by this compound plate aluminum absorber with welded tubes directly to the back surface of the solar module (see Fig. 6).
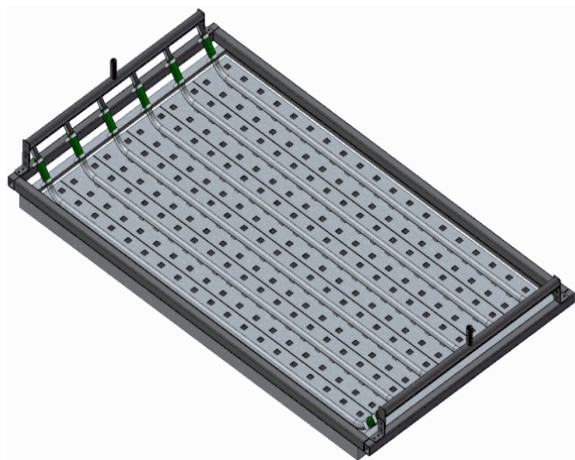

Fig. 6. General view of HSGM module, equipped with a cooling system on the back side

Temperature changes were calculated in the layers included in the standard solar module design (see Fig. 7).
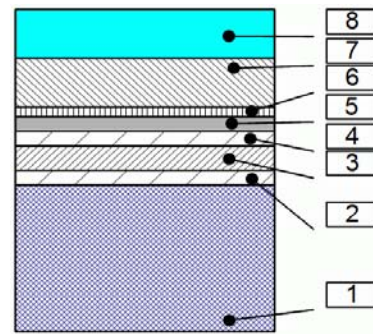

Fig. 7. Construction of hybrid solar generated module:
1 – glass; 2, 4 – EVA film for laminating; 3 – silicon SC;
5 – protective PVC layer; 6 – heat conductive compound;
7 – aluminium absorber; 8 – coolant (water)

In calculating we the expected natural air cooling from front surface and cooling of back surface with the coolant. Area of SC with size 158 mm × 158 mm was 0.02496 m^2, thermal energy, absorbing by SC taking into account the conversion of solar energy into electrical energy is 24.96 W/m^2. Thermal resistances R_t(K/W) and temperature changes ΔT(K) on the layers that make up the construction solar module were calculated [11, 12]. Results are presented in Table 1.

Calculated values of heat resistance R_t(K/W) and temperature differences ΔT(K) on layers that make up a construction of hybrid solar generated module

Layers	Thickness Δ, μm	Heat conduction coefficient, W/(m·K)	R_t, K/W	ΔT, K
Glass	4	1.15	0.1390	-3.48
EVA	0.5	0.33	0.0161	-1.52
Si-SC	0.15	150	0	0
PVC	0.5	0.33	0.0110	-1.52
EVA	0.5	0.19	0.1050	-2.63
Compound	0.25	1.28	0.0080	-0.20
Al absorber	2	236	$3.4 \cdot 10^{-4}$	-0.01

For minimize expends of generated electrical energy to coolant circulation, we proposed to use a thermosiphon system with slight overheating (5-7)° against to the environment. Then, taking into account the calculated temperature differences in the layers of the solar module its overheating against to the environment is reduced up to a (10-12) °C, which reduces the efficiency losses from heat more than twice.

Based on the analysis of Table 1, the highest thermal resistance after the obligatory top glass has a protective PVC film. Changing it to a thin PET (polyethylene terephthalate or polyester), which is produced in thickness (20-150) μm and is close to the PVC value of the thermal conductivity κ = 0.24 W/(m·K) will reduce the ΔT in the protective layer up to (0.2-0.4) °K. It is also possible to reduce the EVA layer thickness from 0.5 mm to 0.3 mm, which will reduce ΔT in this layer up to 0.9 °K. As a result of measures to reduce the system thermal resistance we can achieve the excess of SC temperature above water temperature less 1.5°C.

In addition to the heat exchange units which fixed directly on the HSGM, cooling system also includes the supply and offtake coolant collectors, radiator which cools the coolant, expansion tank and connecting hoses [12-14].

Collectors are used to organize the coolant flow and carried out the distribution of uniform coolant flow from the radiator into the six flows in the number of heat exchange blocks and reverse association coolant flow at the outlet of heat exchanging blocks for supplying the radiator. Collectors are made from standard water pipes. Joining the collectors (Fig. 6) with a heat exchange block to prevent galvanic corrosion and thermal stress compensation is performed through the adapter in the form of segments of reinforced PVC hose. Cooling of the coolant, in which can be used as water or ethylene glycol aqueous solution, is carried out by passing it through the radiator of the tubular structure, made of steel tubing. Tubular radiator design simplifies manufacturing and provides sufficient heat dissipation area for effective heat dissipation extracted from cooled HSGM [15].

Since the cooling circuit is closed, at change the temperature changes the volume of fluid and to compensate for changes in the volumes it is necessary to use expansion tanks. The proposed cooling system can use standard diaphragm expansion tanks, designed for heating systems with solar collectors. They have a working pressure of 6 atm, maximum up to 10 atm, the maximum flow temperature 70 °C, volume (33-40) l and equipped with the necessary fastening elements [16-18].

The experimental testing of the developed HSGM constructive solution carried out by field testing during the week by using generating stand consist from two HSGM samples, equipped according to the developed constructive solution and using a high-voltage power take-off system.

The experimental dependence of generated power distribution during the day is shown on Fig. 8. The analysis of this dependence makes it possible to conclude that the results of the calculation the optimal values of HSGM vertical installation angle allowed to achieve the character of power, generated by HSGM dependence which corresponds to the position of the Sun on the sky.
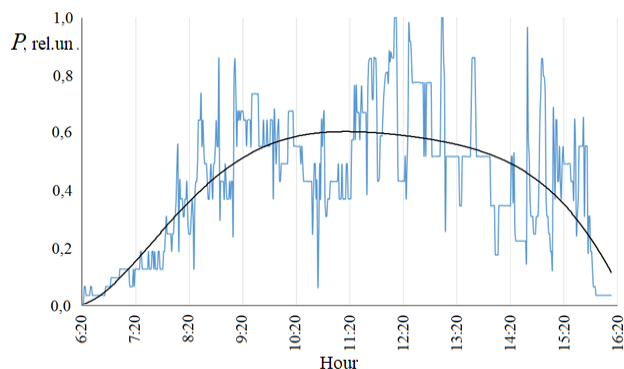

Fig. 8. Distribution of relative power generated by HSGM depending on daytime

During the tests, the working of HSGM cooling system, high-voltage part of power take-off system and the accuracy of HSGM installation angles were checked. The HSGM cooling system, built on the principle of coolant thermosiphon circulation, has been showed high efficiency – depending on the intensity of the incident solar radiation and the ambient temperature, the module temperature does not exceed 20-25 °C. Due to the design features, the cooling system operates completely autonomously, and coolant circulation is only ensured when HSGM photoreceiving surface is actually heated. The absence of temperature sensors and circulation pumps increases its reliability and minimizes energy needed for its working.

Concentrators of sunlight, made in the form of flat mirrors and installed on HSGM, have shown their resistance to wind and rain. The implemented angle of concentrators installation provides an effective self-cleaning from rain drops, while washing away the dust.

High-voltage DC-DC power take-off system [19] demonstrates their high reliability during testing.

In general, the implementation of the developed HSGM design solution allowed to achieve the efficiency this modules up to 18.5 %.

Conclusions.

The study of working temperature influence on the efficiency of Chinese production silicon solar cells shows that the reduction of efficiency is 0,07 %/°C when working temperature increases, that is significantly higher than in the device structures of European and Russian production and a due to the unconventional decrease of short circuit current density.

By the computer modeling of the quantitative influence of diode parameters on efficiency, it has been shown that Chinese production Si-SC efficiency decrease is due to not only by the growth of the traditional diode saturation current density, but also a decrease of shunt resistance.

Identified temperature dependence of efficiency shows the feasibility of using Chinese production Si-SC in the construction of photovoltaic thermal system, which together with the heat pump is part of a combined system for hot water supply, heating and air conditioning. Based on a detailed analysis of the working temperature influence on the efficiency of photovoltaic processes that determine the solar cells work, it was proposed the optimal construction and technological solution hybrid solar generated module, the main feature of which is the heat exchange block, designed to reduce the HSGM working temperature.

The experimental testing of HSGM samples with developed cooling system, high-voltage part of power take-off system demonstrates their reliability and high efficiency which allow to achieve the HSGM efficiency up to 18.5 %.

REFERENCES
1. Bye G., Ceccaroli B. Solar grade silicon: Technology status and industrial trends. *Solar Energy Materials and Solar Cells*, 2014, vol.130, pp. 634-646. **doi: 10.1016/j.solmat.2014.06.019**.
2. Singh P., Ravindra N.M. Temperature dependence of solar cell performance – an analysis. *Solar Energy Materials and Solar Cells*, 2012, vol.101, pp. 36-45. **doi: 10.1016/j.solmat.2012.02.019**.
3. Singh P., Singh S.N., Lal. M., Husain M. Temperature dependence of I–V characteristics and performance parameters of silicon solar cell. *Solar Energy Materials and Solar Cells*, 2008, vol.92, iss.12, pp. 1611-1616. **doi: 10.1016/j.solmat.2008.07.010**.
4. Radziemska E. Effect of temperature on dark current characteristics of silicon solar cells and diodes. *International*

Journal Energy Res, 2006, vol.30, iss.2, pp. 127-134. **doi: 10.1002/er.1113.**

5. Cai W., Chao F., JinLong T., DeXiong L., SiFu H., ZhiGang X. The influence of environment temperatures on single crystalline and polycrystalline silicon solar cell performance. *Science China: Physics, Mechanics and Astronomy*, 2012, vol.55, no.2, pp. 235-241. **doi: 10.1007/s11433-011-4619-z.**

6. Möller H.J. *Semiconductors for solar cells*. Boston, Artech House, 1993.

7. Afanasyev V.P., Terukov E.I., Scherchenko A.A. *Thin film solar cells on the silicon base*. SPbSETU, LETI, 2012.

8. Kharchenko V.V., Nikitin B.A., Tichonov P.V. Select of photoenergy heat module parameters. *Renewable and small energy 2012: Proc. of IX In-tern. ann. conf. M.,* 2012, pp. 292-297.

9. Ramos A., Chatzopoulou M.A., Guarracino I., Freeman J., Markides C.N. Hybrid photovoltaic-thermal solar systems for combined heating, cooling and power provision in the urban environment. *Energy Conversion and Management*, 2017, vol.150, pp. 838-850. **doi: 10.1016/j.enconman.2017.03.024**.

10. Zhang X., Zhao X., Smith S., Xu J., Yu X. Review of R&D progress and practical application of the solar. *Renewable Sustainable Energy Rev*, 2012, vol.16, iss.1, pp. 599-617. **doi: 10.1016/j.rser.2011.08.026**.

11. Herrando M., Markides C.N. Hybrid PV and solar-thermal systems for domestic heat and power provision in the UK: Techno-economic considerations. *Applied Energy*, 2016, vol.161, pp.512-532. **doi: 10.1016/j.apenergy.2015.09.025**.

12. Dupeyrat P., Menezo C., Fortuin S. Study of the thermal and electrical performances of PVT solar hot water system. *Energy and Buildings*, 2014, vol.68, part C, pp.751-755. **doi: 10.1016/j.enbuild.2012.09.032**.

13. Zhao X., Zhang X. *Handbook Nearly Zero Energy Building Refurbishment*, Springer, 2013.

14. Romero Rodríguez L., Salmerón Lissén J.M., Sánchez Ramos J., Rodríguez Jara E.Á., Álvarez Domínguez S. Analysis of the economic feasibility and reduction of a building's energy consumption and emissions when integrating hybrid solar thermal/PV/micro-CHP systems. *Applied Energy*, 2016, vol.165, pp.828-838. **doi: 10.1016/j.apenergy.2015.12.080**.

15. He W., Chow T.-T., Ji J., Lu J., Pei G., Chan L. Hybrid photovoltaic and thermal solar-collector designed for natural circulation of water. *Applied Energy*, 2006, vol.83, iss.3, pp.199-210. **doi: 10.1016/j.apenergy.2005.02.007.**

16. Coventry J.S. Performance of a concentrating photovoltaic/thermal solar collector. *Solar Energy*, 2005, vol.78, iss.2, pp. 211-222. **doi: 10.1016/j.solener.2004.03.014.**

17. Pathak M.J.M., Sanders P.G., Pearce J.M. Optimizing limited solar roof access by exergy analysis of solar thermal, photovoltaic, and hybrid photovoltaic thermal systems. *Applied Energy*, 2014, vol.120, pp.115-124. **doi: 10.1016/j.apenergy.2014.01.041.**

18. Liang R., Zhang J., Ma L., Li Y. Performance evaluation of new type hybrid photovoltaic/thermal solar collector by experimental study. *Applied Thermal Engineering*, 2015, vol.75, pp.487-492. **doi: 10.1016/j.applthermaleng.2014.09.075.**

19. Zaitsev R.V., Kyrychenko M.V., Kholod A.V., Zaitseva L.V., Prokopenko D.S., Khrypunov G.S. Calculation of operating parameters of high-voltage power take-off system for the photovoltaic facility. *Electrical engineering & electromechanics*, 2016, no.4, pp. 63-68. **doi: 10.20998/2074-272X.2016.4.09.**

R.V. Zaitsev[1]*, Doctor of Technical Science, Associate Professor,*
M.V. Kirichenko[1]*, Candidate of Technical Science, Senior Researcher,*
G.S. Khrypunov[1]*, Doctor of Technical Science, Professor,*
L.V. Zaitseva[2]*, Candidate of Technical Science, Senior Lecturer,*
O.N. Chugai[2]*, Doctor of Technical Science, Professor,*
A.A. Drozdova[1]*, Candidate of Phys.-Math. Science, Associate Professor,*
[1] National Technical University «Kharkiv Polytechnic Institute»,
2, Kyrpychova Str., Kharkiv, 61002, Ukraine,
e-mail: zaitsev.poman@gmail.com
[2] Zhukovsky National Aerospace University «Kharkiv Aviation Institute»,
17, Chkalov Str., Kharkiv, Ukraine, 61000.

Передплатний індекс: 01216